UNITED NATIONS EDUCATIONAL, SCIENTIFIC AND CULTURAL ORGANIZATION
INTERNATIONAL ATOMIC ENERGY AGENCY
INTERNATIONAL CENTRE FOR THEORETICAL PHYSICS
I.C.T.P., P.O. BOX 586, 34100 TRIESTE, ITALY, CABLE: CENTRATOM TRIESTE

SMR/989 - 6

"Course on Shallow Water and Shelf Sea Dynamics "
7 - 25 April 1997

"The M_2 Tide on the Amazon Shelf"

&

"Physical Oceanography of the Amazon Shelf"

J. CANDELA
Centro de Investigacion Cientifica
Y Educacion Superior de Ensenada (Cicese)
Ensenada
Mexico

Please note: These are preliminary notes intended for internal distribution only.

JOURNAL OF GEOPHYSICAL RESEARCH, VOL. 100, NO. C2, PAGES 2283–2319, FEBRUARY 15, 1995

The M_2 tide on the Amazon shelf

Robert C. Beardsley,[1] Julio Candela,[1] Richard Limeburner,[1] W. Rockwell Geyer,[1] Steven J. Lentz,[1] Belmiro M. Castro,[2] David Cacchione,[3] and Nelson Carneiro[4]

Abstract. As part of A Multidisciplinary Amazon Shelf Sediment Study (AMASSEDS), moored and shipboard current measurements made over the Amazon shelf during 1990–1991 have been analyzed to determine the dominant semidiurnal tidal constituent, the M_2. These results have been combined with coastal sea level data from within the Amazon and Para Rivers, the adjacent shelf, and with satellite-derived tidal elevation data from off the shelf to provide a more complete description of the M_2 tide in this complex river/shelf system. Near the Amazon River mouth the M_2 tide propagates across the shelf and through the mouth as a damped progressive wave, with its amplitude decreasing and phase increasing upriver. Over the adjacent shelf north of Cabo Norte, the M_2 tide approaches a damped standing wave, with large amplitudes (greater than 1.5 m) near the coast due to near resonance within the coastal embayment formed by the Cabo Norte shoal to the south and Cabo Cassipore to the north. The observed M_2 tidal currents are nearly rectilinear and oriented primarily across the local isobaths. Comparisons between tidal observations in both the North Channel and the Cabo Norte–Cabo Cassipore embayment and a simple variable-width channel tidal model indicate that (1) most of the M_2 tidal energy dissipation occurs over the mid- and inner shelf (in water depths less than 20 m) and (2) fluid muds found there cause a significant reduction (of order 50%) in the effective bottom friction felt by the M_2 tide. The approximate resonant period of the Cabo Norte–Cabo Cassipore embayment is 11.9 hours, and at resonance the average energy dissipation per forcing period is roughly 2.2 times the average mechanical energy in the embayment. This damping rate is large enough that the tidal amplification is rather insensitive to forcing frequency, so that the response of the embayment to forcing over the semidiurnal band should be essentially the same. The vertical structure of the M_2 tidal current is examined at one outer shelf site located in 65-m water depth. The observed semimajor axis increases logarithmically with height above bottom within the lowest 1–2 m and reaches a maximum in excess of 0.5 m/s at approximately 11 m above bottom. The mean ellipticity is small (less than 0.1) and positive, indicating clockwise rotation of a nearly rectilinear current, and the semimajor axis is oriented within 10° of the local cross-isobath direction. The M_2 phase increases with height above bottom, with flood at the bottom leading flood at the surface by about 1 hour. A simple, local homogeneous tidal model with time- and space-dependent eddy viscosity simulates the observed near-bottom velocity reasonably well, however, the model suggests that stratification above the lowest few meters may significantly affect the tidal boundary layer structure at this site. The M_2 energy flux onto the Amazon shelf and into the Amazon and Para Rivers has been estimated using current and surface elevation data and the best fit variable-width channel model results. The net M_2 energy flux into the mouths of the Amazon and Para Rivers is 0.47×10^{10}W and 0.19×10^{10}W, respectively. A net M_2 energy flux of about 3.3×10^{10}W occurs onto the shelf between the North Channel of the Amazon River and Cabo Cassipore. This stretch of the Amazon shelf accounts for about 1.3% of the global dissipation of the M_2 tide.

[1] Department of Physical Oceanography, Woods Hole Oceanographic Institution, Woods Hole, Massachusetts.
[2] Instituto Oceanográfico, Universidade de São Paulo, São Paulo, Brazil.
[3] U.S. Geological Survey, Menlo Park, California.
[4] Directoria de Hidrografia e Navegacao, Niteroi, Brazil.

Paper number 94JC01688.
0148-0227/95/94JC-01688$05.00

1. Introduction

The Amazon River is the world's largest river in terms of freshwater discharge, supplying about 15% of the total riverine input of fresh water entering the world's oceans [*Baumgartner and Reichel*, 1975]. This discharge which varies from a low of about 0.08 Sv in November to a high of 0.25 Sv in June [*Oltman*, 1968] creates an enormous surface plume over the Amazon shelf, and dilute water from the plume can be traced

thousands of kilometers into the adjacent ocean [*Muller-Karger et al.*, 1988, *Lentz*, this issue]. The sediment discharge of the Amazon is also quite large; about three million tons of sediment are carried through the river mouth per day, on average [*Nittrouer et al.*, 1986]. A significant fraction of this sediment flux is presently accumulating in a large subaqueous delta over the inner and middle Amazon shelf [*Nittrouer et al.*, 1986]. The Amazon shelf is also distinguished for its large semidiurnal tides and strong tidal currents, large fortnightly variability, and tidal ranges at the river mouth of more than 3 m [*Gibbs*, 1982; *Curtin*, 1986]. These features plus the location of the mouth of the Amazon River at the equator make the Amazon River mouth and adjacent shelf a fascinating region and a unique natural laboratory to study a number of important processes in tidal dynamics, such as the dynamical mechanisms responsible for tidal dissipation and its time variability, the influence of large variations in river discharge on tidal propagation, and the effects of tidal and river discharge current interactions on sediment and nutrient transports.

We present here a new description of the dominant semidiurnal tidal constituent, the M_2 (12.42-hour period), in the Amazon River mouth and adjacent shelf region. This constituent, plus the other principal semidiurnal constituents, the S_2 (12.00-hour period) and N_2 (12.66-hour period), account for about 85% or more of the total tidal elevation variance and are the most energetic tides in this region. This description is based on a combined analysis of historical coastal sea level data recently obtained from the Brazilian Navy Hydrographic and Navigation Directory, moored bottom pressure and shipboard and moored current data recently collected as part of A Multidisciplinary Amazon Shelf SEDiment Study (AMASSEDS), and satellite-derived tidal elevation data from the western equatorial Atlantic published by *Cartwright et al.* [1991]. AMASSEDS was a multicomponent U.S./Brazil program designed to study physical, geological, and geochemical processes which control sediment transport and accumulation in this complex shelf environment [*AmasSeds Group*, 1990; *Nittrouer et al.*, 1991]. The physical oceanographic component included four regional shipboard acoustic Doppler current profiler (ADCP)/conductivity-temperature-depth (CTD) surveys, three intensive small-scale studies of the Amazon frontal zone, a 5-month deployment of a moored current meter array, and deployments of satellite-tracked drifters. The ADCP/CTD surveys were timed to sample the shelf during the four stages of the Amazon River discharge as follows: August 1989 (falling discharge), February 1990 (rising), May 1990 (maximum), and November 1991 (minimum). Frontal studies consisting of continuous acquisition of ADCP and high-resolution current and suspended sediment profile data at several anchor stations were conducted in March and June 1990 and November 1991. Some preliminary results of the physical oceanography component of AMASSEDS [*Geyer et al.*, 1991; *Candela et al.*, 1992] have been published prior to this special volume. This paper attempts to synthesize a coherent description of the M_2 tide in this region based on the entire AMASSEDS physical data set and available coastal and ocean sea level data.

This paper is organized as follows. A brief description of the offshore semidiurnal tidal forcing is presented next in section 2, followed by a detailed description of the barotropic M_2 tidal response of the Amazon shelf and river mouth region in section 3. A simple variable-width channel tidal model is then used in section 4 to explain how the regional geometry and bottom friction combine to govern the M_2 tidal response. The vertical structure of the M_2 tidal currents at one outer shelf site is then described in section 5 and is interpreted in terms of a simple eddy viscosity model. A simple estimate of the net flux of M_2 tidal energy on the Amazon shelf and into the Amazon and Para Rivers is discussed in section 6. Conclusions are presented in section 7.

2. Description of the Observed Semidiurnal Tides in the Tropical Atlantic

Cotidal charts of the semidiurnal tides in the Atlantic Ocean have been published by *Defant* [1961], *Schwiderski* [1979, 1981] (hereinafter referred to collectively as S79) and *Cartwright et al.* [1991] (hereinafter referred to as CRS91). Both *Defant* [1961] and S79 use coastal and in situ tidal data and either subjective or dynamic interpolation to construct their cotidal charts, while CRS91 use only sea surface height computed from Geosat radar altimeter data obtained during the Exact Repeat Mission (ERM). All show the M_2, S_2, and N_2 to be the dominant semidiurnal constituents, in that order, in the equatorial Atlantic. All three constituents exhibit a broad region of little phase change and maximum amplitude off the Amazon shelf, with amplitudes based on CRS91 varying from about 70 to 85 cm for M_2, 20 to 28 cm for S_2, and 15 to 17 cm for N_2 (Figure 1). The relative amplitudes of the two smaller constituents to M_2 are about $S_2/M_2 = 0.31$ and $N_2/M_2 = 0.21$, indicating a large spring–neap variation ($(M_2 + S_2)/(M_2 - S_2) = 1.9$) and monthly variation ($(M_2 + S_2 + N_2)/(M_2 - S_2 - N_2) = 3.2$) in the semidiurnal forcing. The two principal diurnal constituents in the western equatorial Atlantic, K_1 and O_1, have maximum amplitudes of 6–8 cm off the Amazon shelf (CRS91). Thus the primary tidal forcing on the Amazon shelf is semidiurnal, with the M_2 being the dominant constituent.

A conceptual model of the equatorial Atlantic semidiurnal tides is provided by *Platzman et al.* [1981]. *Platzman* [1984] shows that these tides can be synthesized from a relatively small number of gravity wave normal modes for the Atlantic basin. Three modes in particular exhibit features which can be seen in the observed tides as follows: mode 30, a "North Atlantic transverse half wave" with a period of 13.0 hours; mode 31, identified as the "Gulf of Guinea one-quarter wave" with a period of 12.8 hours; and mode 33, identified as a "transverse half wave" between Africa and

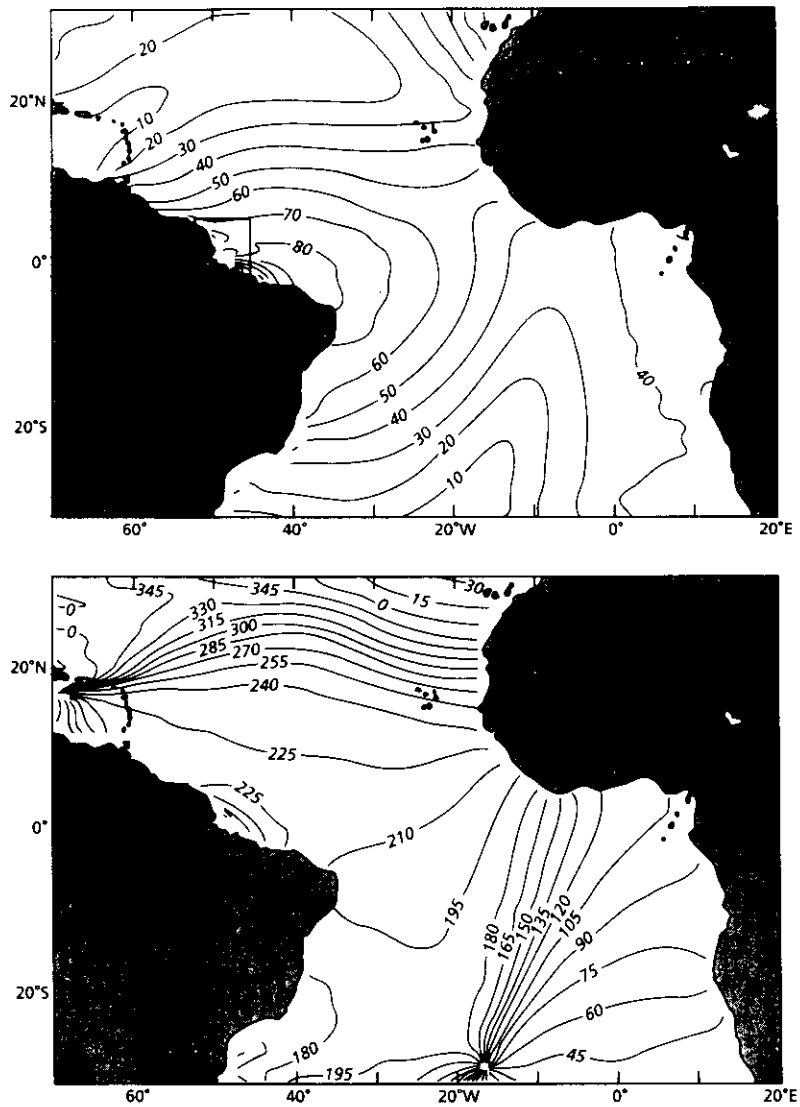

Figure 1. Cotidal map for the M_2 constituent in the tropical Atlantic Ocean derived from Geosat radar altimeter measurements by *Cartwright et al.* [1991]. (top) Amplitude is shown in centimeters and (bottom) phase is shown in degrees Greenwich. The Amazon shelf region is located in the small box in the top panel. The cotidal charts for the S_2 and N_2 constituents are similar in structure in the western equatorial Atlantic. This figure kindly supplied by R. Ray.

South America with a period of 12.1 hours [*Platzman et al.*, 1981]. With a global quality factor Q in the semidiurnal band in excess of 14 [*Platzman*, 1984], the tidal response should exhibit a noticeable change in structure with varying forcing frequency, and the observed semidiurnal tides in the tropical Atlantic do exhibit changes consistent with this prediction.

Using Geosat data, *Cartwright and Ray* [1991] show that, globally,the S_2 and especially M_2 tides are primarily forced in the equatorial band. This is true in the Atlantic, with the largest amplitudes within the basin occurring in the western tropical Atlantic except for comparable amplitudes near the northwest European shelf. The ratio of the observed tidal amplitude off the Amazon shelf to its equilibrium value varies from about 3.2 for M_2 to 2.2 for both N_2 and S_2. The strong oceanic semidiurnal tidal forcing present off the Amazon shelf is thus a consequence of the near-resonant response of the Atlantic basin to the astronomical tidal forcing in the semidiurnal band.

A comparison was made between the S79 and CRS91 cotidal charts and ocean tide data in the western tropical Atlantic to determine which charts were more accurate for the dominant M_2 and S_2 constituents. The ocean tide data available consist of two bottom pressure stations located near 51°W and four bottom-mounted inverted echo sounder (IES) stations located along 44°W (Table 1). Even though *Cartwright* [1982] argues that the IES tidal signal is generally contaminated by internal tides, the IES records are at least 1 year long, and estimates of the amplitude uncertainty based on noise spectra are typically less than ±2 cm in the semi-

Table 1. Ocean In Situ and Coastal M_2, S_2, and N_2 Tides Measured in the Western Equatorial Atlantic

Station	Latitude, °N	Longitude, °W	M_2 A, cm	M_2 P, °G	S_2 A, cm	S_2 P, °G	N_2 A, cm	N_2 P, °G	Record Length, days	Source
					Ocean Stations					
1	2.983	44.017	61.9	209	21.6	237	13.8	195	506	1
2	5.083	44.117	50.1	78	16.0	228	15.3	240	378	1
3	6.950	43.983	64.9	228	21.5	259	14.0	219	1022	1
4	8.783	44.000	66.8	69	20.1	255	15.0	217	383	1
5	9.983	50.517	50.2	224	14.8	252	10.6	207	83	2
6	7.000	51.550	57.7	222	17.4	248	12.4	204	81	2
7	3.317	48.267	81.0	233	15.2	266	27.5	232	29	3
8	3.000	49.333	90.0	254	30.1	296	29.1	237	32	4
9	3.385	49.940	103.3	254	28.8	282	22.0	232	182	5
					Coastal Stations					
87	4.233	51.642	107.4	288	28.1	321	15.9	265	32	4
91	3.850	51.133	101.3	288	22.6	321	34.8	281	32	4
93	2.592	50.850	276.8	301	57.2	347	50.1	270	32	4
9	2.097	50.500	351.4	318	87.5	6	60.5	307	32	4
94	1.217	49.883	155.7	43	33.4	73	24.3	8	32	4
66	0.767	50.113	155.8	90	31.0	129	22.4	49	42	4
29	−0.158	49.150	144.9	43	38.2	69	20.4	26	60	4
79	−0.173	48.767	136.1	12	41.0	38	29.8	356	32	4
80	−0.223	48.465	123.0	341	40.9	14	22.9	334	32	4
81	−0.662	48.050	158.5	344	47.3	18	35.6	296	30	4
*S	−0.617	47.350	176.4	302	57.7	343	33.2	291	369	6
8	−0.617	47.350	174.1	298	55.9	335	32.2	289	364	4
*B	−1.448	48.502	117.0	62	32.7	107	21.5	48	369	6
86	−0.892	46.617	190.0	293	49.2	305	35.4	306	31	4
109	−1.408	45.417	184.0	276	54.7	311	34.3	262	327	4
107	−1.642	45.355	230.0	279	70.6	318	45.0	265	364	4
					River Stations					
1	−1.448	48.502	116.3	61	33.1	102	21.9	48	356	4
5	−1.800	50.275	47.8	255	9.3	283	9.6	242	45	4
6	−1.127	52.210	40.1	20	7.9	53	5.8	339	34	4
11	−2.577	44.370	216.8	291	57.5	331	41.2	282	118	4
13	−2.678	44.363	218.8	294	59.0	335	44.9	285	87	4
14	−2.567	44.367	224.4	287	63.2	321	39.9	262	97	4
15	0.917	50.077	192.8	77	52.8	120	49.8	53	32	4
17	−1.408	51.653	56.7	322	11.5	349	10.5	278	32	4
19	−0.017	50.608	83.0	139	- - -	- - -	- - -	- - -	7	4
21	−1.315	48.488	125.0	55	37.5	93	30.5	32	32	4
22	−0.142	49.988	115.5	94	26.8	138	20.3	78	32	4
23	−0.152	50.392	79.8	148	18.0	175	19.6	113	32	4
24	−1.395	48.492	116.8	57	35.4	104	22.7	50	118	4

Table 1. (continued)

Station	Latitude, °N	Longitude, °W	M_2 A, cm	M_2 P, °G	S_2 A, cm	S_2 P, °G	N_2 A, cm	N_2 P, °G	Record Length, days	Source
30	−0.200	50.683	65.6	179	- - -	- - -	- - -	- - -	7	4
31	−1.132	50.925	71.5	299	10.6	326	10.0	265	366	4
32	−1.183	48.467	119.4	35	35.6	71	18.8	8	32	4
33	−0.917	48.283	143.7	10	44.1	52	28.2	349	32	4
34	−0.938	50.875	66.5	272	9.1	292	9.7	237	32	4
39	−1.533	48.750	111.2	77	34.3	119	18.7	60	47	4
44	−1.693	50.493	50.3	284	7.4	342	6.9	269	236	4
45	−1.100	51.238	68.7	316	10.1	352	8.7	293	224	4
46	−1.697	50.600	29.7	313	0.4	121	2.6	316	32	4
56	−1.822	49.817	54.0	179	12.0	226	5.4	160	32	4
57	−2.242	49.517	111.4	180	25.4	226	20.0	184	32	4
59	−0.432	50.420	124.9	141	23.9	137	- - -	- - -	15	4
62	−0.057	51.180	106.0	198	24.3	234	19.0	165	61	4
72	0.033	51.050	105.4	191	20.6	223	21.5	159	32	4
75	−1.127	52.210	23.0	32	3.5	66	1.7	32	88	4
76	−0.930	52.427	35.9	330	5.0	115	3.2	48	93	4
83	−0.575	47.900	132.9	334	25.1	46	45.1	326	32	4
84	−0.725	50.770	67.8	241	14.9	266	15.0	204	32	4
85	−0.725	50.770	70.9	81	13.3	270	11.3	152	216	4

Many of these tidal constants result from an analysis of sea level data obtained from the Brazil Navy Hydrographic and Navigation Directory. A is amplitude, P is phase, and °G is degrees Greenwich. Sources are 1, inverted echo sounder results (E. Katz, personal communication, 1991); 2, bottom pressure results from *Cartwright and Zetler* [1985]; 3, moored pressure measurements from *EG&G* [1981]; 4, Brazil Navy Hydrographic and Navigation Directory; 5, moored pressure measurements from *Alessi et al.* [1992]; and 6, *National Oceanic and Atmospheric Administration* [1973] Coast and Geodetic Survey.

*S indicates Salinopolis and *B indicates Belem.

diurnal band (E. Katz, personal communication, 1991). The results (Table 2) show that although both CRS91 and S79 tend to overestimate the observed M_2 amplitude, CRS91 differs less in both amplitude and phase from in situ observations. The differences between both cotidal charts and observation are less for S_2, with CRS91 showing slightly better agreement. On the basis of this very limited comparison, we have chosen to use the CRS91 tidal data to describe the semidiurnal tidal forcing off the Amazon shelf.

3. Description of the Semidiurnal Tides Over the Amazon Shelf

The geometry of the Amazon continental margin is complex (Figure 2). Situated next to the Ceara and Demerara abyssal plains, the Amazon continental slope is relatively straight and aligned approximately northwest–southeast except over the Amazon cone. The shelf break occurs at a depth of about 100 m, and the shelf width varies from a minimum of about 100 km to the northwest near 4°N, to a maximum of about 250 km near the mouths of the Amazon and Para Rivers, to about 150 km to the southeast near 45°W. Since the last glaciation, much of the suspended sediment discharge of the Amazon River has been deposited off and to the northwest of the Amazon River mouth, creating a large, subaqueous delta of fine sediment [*Nittrouer et al.*, 1983; 1991]. This delta extends offshore to about the 60-m isobath, and as a result, the inner shelf between about 1 and 4°N is quite broad and shallow. Offshore of this delta, the outer shelf is relatively smooth and covered with coarser relict sediment.

The bottom topography in the Amazon River mouth is quite complex and not well known (Figures 2 and 12). Typical water depths in both the North and South Channels exceed 20 m. As these channels reach the

Table 2. Comparison Between In Situ Tidal Measurements and the Tidal Charts of *Schwiderski* [1979] and *Cartwright et al.* [1991] in the Western Equatorial Atlantic

	M_2		S_2	
	Amplitude, cm	Phase, °G	Amplitude, cm	Phase, °G
	Comparison Near 51° W (n = 2)			
S79	−6.0	−7°	−1.1	3°
CRS91	−1.3	−1°	−0.4	3°
	Comparison Near 44° W (n = 3)			
S79	−14.3 ± 12.7	−17° ± 10°	−1.3 ± 3.7	−7° ± 13°
CRS91	−5.0 ± 11.1	−8° ± 12°	0.8 ± 3.3	−5° ± 12°

Comparisons are made between (top) two in situ bottom pressure measurement sites located near 51°W (stations 5 and 6, Table 1) with the tidal charts of *Schwiderski* [1979] (S79) and *Cartwright et al.* [1991] (CSR91) and (bottom) three inverted echo sounder (IES) sites located near 44°W (stations 1, 2, and 4, Table 1) with S79 and CRS91. For the bottom pressure comparison, the difference in amplitude (centimeters) and phase (degrees Greenwich) are given. For the IES comparison, both mean difference and standard deviations are given. The tidal values at the IES station near 7°N (station 3) were not consistent with the others and were not included in this comparison.

river mouth, they shallow to depths less than 7 m. For simplicity, we will define here the mouth of the Amazon River to be the transverse shoal with water depth less than 7 m which stretches between Cabo Maguari (separating the South Channel and the Para River) and Cabo Norte. The presence of a large and very shallow bank (Banco Santa Rosa) between the North and South Channels serves to separate the two channels and make the depth profile offshore of this center region monotonic. Northeast of Cabo Norte, a large shallow shoal (called here the Cabo Norte shoal) extends about 90 km offshore over the inner shelf. This shore-perpendicular shoal may be clearly seen in the offshore extension of the 5-m isobath (Figure 2). Owing to its large size and very shallow depth, this shoal tends to separate the Amazon River mouth area from the shelf to the northwest and may present a partial barrier to along-shore flow.

3.1. Coastal Tidal Admittance

An initial picture of the response of this shelf region to semidiurnal tidal forcing can be gained from the tidal admittance at selected coastal and river stations. In Figure 3 (top) the ratio of the coastal elevation amplitude normalized by the ocean forcing elevation is plotted for each constituent as a function of alongshore position and the difference in phase between the coast and ocean is plotted in Figure 3 (middle). Figure 3 (bottom) shows the shelf geometry and location of the eight shelf and six river mouth stations. The ocean tidal forcing was estimated using CRS91 along a transect parallel to the shelf break and located about 50 km offshore of the shelf break (to reduce the effects of spatial averaging over the upper slope in the satellite-derived data). The coastal tide constituents were computed from sea level records using harmonic analysis [*Forman*, 1977] (see Appendix A for a discussion of the analysis method); the results, together with station location, record duration, and other information, are listed in Table 1.

In general, the cross-shelf phase difference for all three semidiurnal constituents increases along the shelf toward the Amazon River mouth. Within the river mouth the increase in phase upstream illustrates the well-known observation that the semidiurnal tides propagate upriver through the river mouth [*Defant*, 1961; *Ferraz*, 1975]. While there is considerable scatter in the individual values for each constituent, the admittance amplitude exhibits a clear along-shelf asymmetry, with large amplitudes in excess of 3 occurring to the north between Cabo Norte and Cabo Cassipore and maximum amplitudes of less than 2.5 occurring to the southeast of Cabo Norte. Within the North and South Channels the average admittance amplitude is about 1.6 and 1.8, respectively. As each constituent propagates across the shelf into shallower water, conservation of energy leads to an increase in tidal elevation amplitude which causes the admittance amplitude to exceed 1 despite dissipation. In the river mouth the relative decrease in

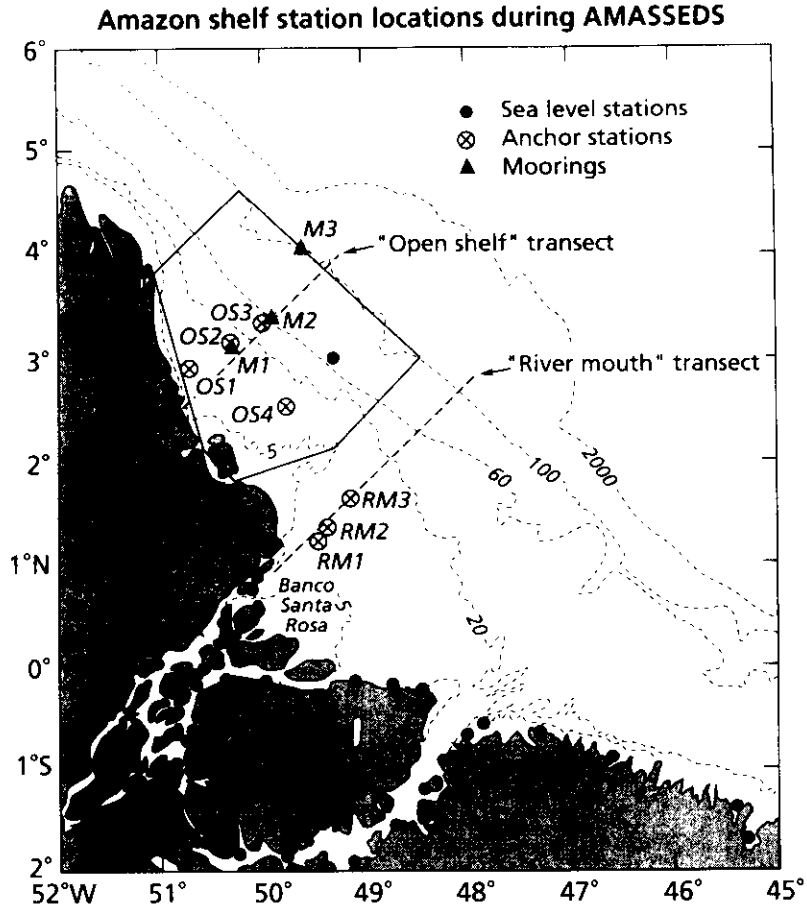

Figure 2. Topographic map of the Amazon continental margin. The 5-, 20-, 60-, 100-, and 2000-m isobaths are shown. Note the complex topography near the Amazon River mouth and the large shore-perpendicular shoal off Cabo Norte. The shelf break is located along the 100-m isobath, and the 2000-m isobath indicates the location of the Amazon cone. Also shown are the locations of the three moored stations (M1–M3), the three river mouth anchor stations (RM1–RM3), and the four open shelf anchor stations (OS1–OS4) where physical measurements were made during AMASSEDS, and 39 coastal stations and one midshelf station where historical tide measurements have been obtained. The AMASSEDS moored stations and three anchor stations are located along the "open shelf" cross-shelf transect, and the three AMASSEDS river mouth anchor stations are located along the "river mouth" cross-shelf transect.

admittance amplitude from the adjacent shelf areas and the phase structure indicate significant propagation of tidal energy upriver. North of Cabo Norte, the increase in coastal admittance amplitude with increasing shelf width and existence of an amplitude maximum suggest that the semidiurnal tides in this area may be in near resonance with their offshore forcing.

To illustrate this last point, we take advantage of the equatorial setting of this shelf region (with Coriolis parameter $f = 0$) and consider the simple analytic cross-shelf barotropic tidal model discussed by *Clarke* [1991]. The shelf tide is forced by the ocean tide prescribed at the shelf break, the dynamics are linear, bottom friction is represented by a constant frictional decay timescale, the bottom topography is linear between the coast and the shelf break at the 100-m isobath, and all alongshore effects are ignored. The coastal response function is then

$$\frac{\zeta_c}{\zeta_{sb}} = \frac{1}{J_0(\mu L)} \quad , \tag{1}$$

where

$$\mu = \frac{2\sigma}{\sqrt{gh_0}}\,(1 - i\varepsilon) \quad , \tag{2}$$

where ζ_c and ζ_{sb} are the coastal and shelf break elevations, respectively, J_0 is the Bessel function of order 0 of the first kind, L is the width of the shelf between the coast and shelf break, h_0 is the depth of the shelf break, σ is the tidal frequency, g is gravity, and ε is the ratio of the tidal period to (2π) times the friction timescale.

Using values of σ and ε relevant for M_2, we plot in Figure 3 the admittance amplitude and phase difference predicted by (1) as a function of alongshore position for the shelf to the northwest and southeast of the river

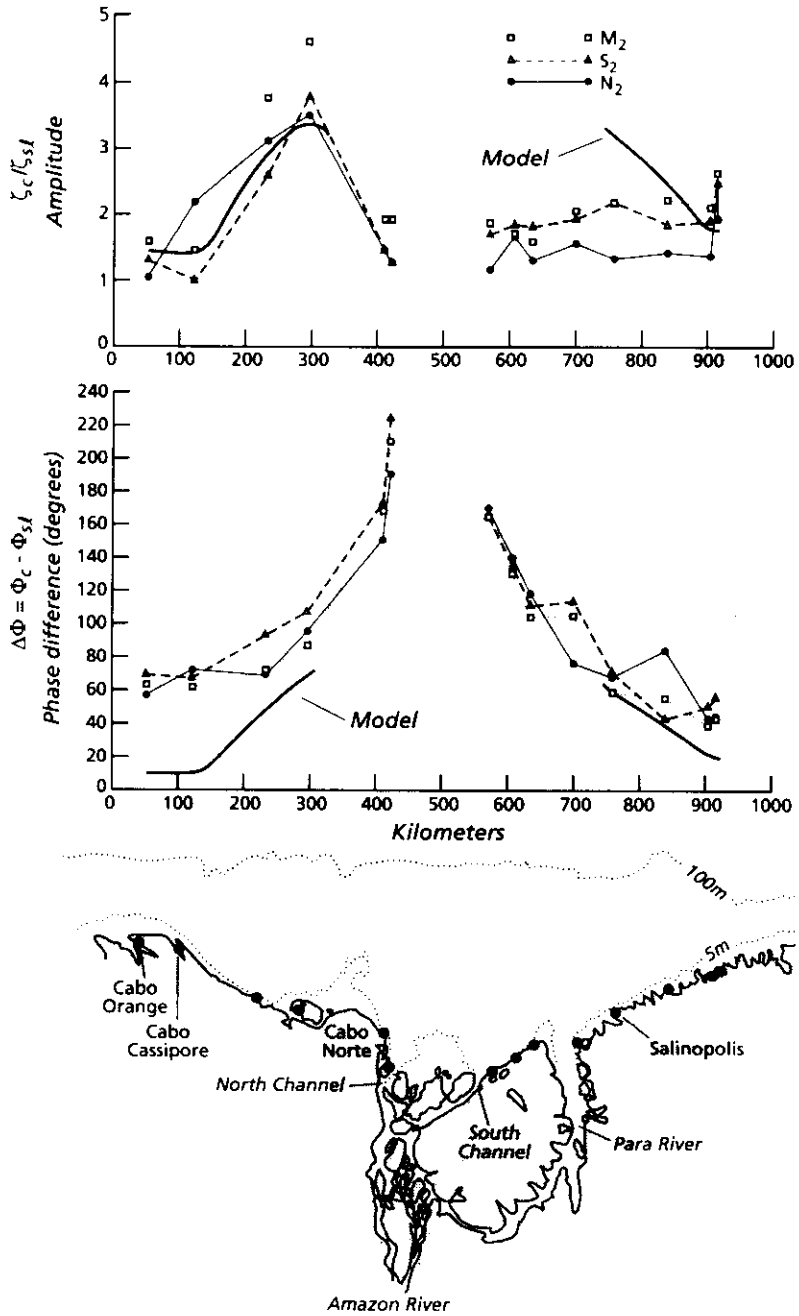

Figure 3. Semidiurnal tidal admittance function at selected coastal stations along the Amazon shelf region. (top) The admittance amplitude or the coastal elevation amplitude divided by the elevation amplitude over the slope for the three main semidiurnal constituents. (middle) The difference in the elevation phase at the coast from that over the slope. (bottom) The locations of the 14 coastal stations. The 5- and 100-m isobaths are shown to indicate the general shape of the shelf and the Cabo Norte shoal. Note the difference in the response between the Cabo Norte–Cabo Cassipore embayment and the Amazon and Para river mouth region. The admittance amplitude and phase difference predicted with the simple constant-slope analytic model described in section 3.1 is denoted by the thick solid curves. The model friction parameter ($\varepsilon = 0.5$) was picked to give good agreement for M_2 elevation and transport along the open shelf transect.

mouth. Between Cabo Norte and Cabo Cassipore the model predicts an amplitude maximum of about 3.4, in rough agreement with the observed admittance amplitude (although less than that exhibited by M_2). While the model underpredicts the cross-shelf phase difference in this northern shelf region, especially at the two stations near Cabo Cassipore and Cabo Orange, the model correctly estimates the alongshore trend in phase difference near the center of this area between Cabo Norte and Cabo Cassipore. (The large underprediction of the phase difference at these two stations may be due in part to their locations within local embayments. In general,

this model will underestimate the observed phase difference presented in Figure 3 since the latter is the phase difference between maximum elevation at the coast and about 50 km offshore of the shelf break. Following *Clarke* [1991], crude estimates of the amplitude and phase variations which may occur across the continental slope (including the Amazon cone) are < 10 cm and < 5–20°. These changes, being largely unknown, have been ignored in constructing Figure 3.) Given a shelf break depth of $h_0 = 100$ m, the model predicts that inviscid quarter-wave resonance occurs for M_2 at a shelf width $L = 268$ km. With friction appropriate for M_2 the resonant shelf width is decreased to $L = 252$ km. The maximum shelf width in this northern shelf area is about 225 km, roughly 90% of the model resonant value, suggesting that this northern shelf region is near resonant at semidiurnal frequencies. To the southeast of the Amazon River mouth, the model correctly predicts the alongshore trend in phase difference but overpredicts the amplitude increase as the shelf gets wider near the mouth of the Para River. This suggests that a significant fraction of the onshore tidal energy flux continues upstream into the Para and Amazon Rivers rather than be reflected at the coast. This further suggests that the Cabo Norte shoal plays an important role in the asymmetry of the observed tidal response by inhibiting the onshore tidal energy flux entering the Cabo Norte–Cabo Cassipore area from flowing into the Amazon River mouth. Thus the amplitude maximum found between Cabo Norte and Cabo Cassipore is due to a combination of near-resonant shelf width and partial isolation from the Amazon River mouth region.

The similarity of the M_2, S_2, and N_2 admittance functions suggests that the response of this shelf region is essentially the same for these three constituents. Since the offshore S_2 and N_2 forcing have relative amplitude ratios compared with the M_2 of about 0.3 and 0.2, we expect large fortnightly (of order 30%) and monthly (of order 50%) variability in the semidiurnal tide and tidal currents over the whole shelf region. Even though the rest of this paper is focused on the M_2 constituent since it is the most energetic and accurately observed constituent, it is important to remember that the other semidiurnal constituents are also quite energetic and that the large spring–neap and monthly variations are essential features of the regional semidiurnal tides.

3.2. M_2 Cotidal Charts for the Amazon Shelf

We present next cotidal charts for the M_2 elevation and transport fields over the Amazon shelf based on all available data. (We note that cotidal charts can be a useful synthesis of available information about the major harmonic constituents of the tide in a given area. In the case of elevation, the cotidal chart presents contours of equal amplitude and phase of each constituent considered, while for transport it is necessary to describe the behavior of the four parameters defining the tidal ellipse, i.e., the semimajor and semiminor axes, its geographical orientation, and phase. For elevation the phase indicates the time of maximum amplitude, while for transport the phase indicates the time of maximum transport along the semimajor axis in the direction indicated by the given orientation. Unfortunately, the data

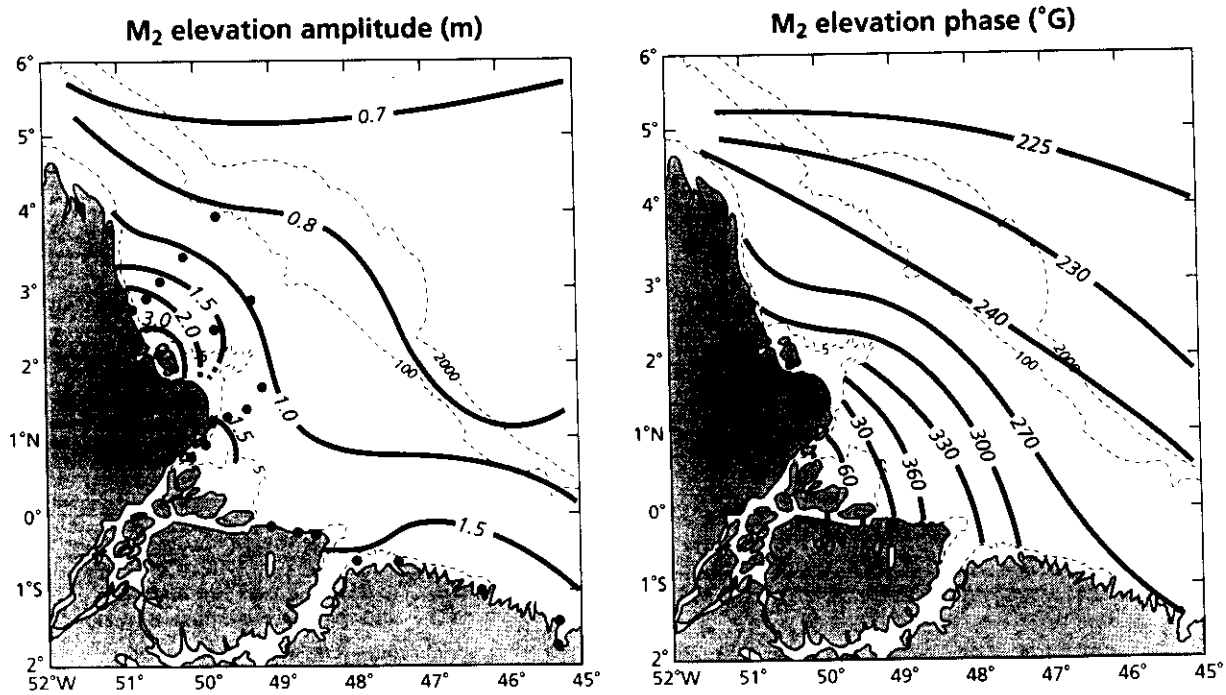

Figure 4. (left) M_2 elevation amplitude (meters) and (right) elevation phase (degrees Greenwich) for the Amazon shelf. These cotidal charts were drawn from elevation data at the shelf stations, denoted by dots, and altimetric results from CRS91 offshore of the shelf break.

are seldom dense enough to draw unambiguous cotidal charts so they contain a certain degree of arbitrariness. However, they are of value in interpreting the data available, for checking results of further analyses on new observations, and for understanding the dynamics of the tides. Usually, cotidal charts are restricted to elevation since current measurements are seldom dense enough spatially to construct a cotidal chart with any degree of certainty. However, in recent years the large spatial coverage which can be attained through shipboard ADCP surveys has permitted construction of an approximate transport cotidal chart for at least the major tidal constituents within a given survey area. Whenever the tide has a strong semidiurnal barotropic character, as in the case for the Amazon shelf, the M_2 cotidal charts alone suffice to give a good estimate of the mean amplitude of the tidal elevation at a given site and of the mean time of high and low water, as well as the mean timing, amplitude, and direction of the tidal currents present in the region.)

The M_2 elevation cotidal chart (Figure 4) includes data from 15 coastal stations located between 2°S and 4°N which are reasonably well exposed to the shelf (Figure 2), the AMASSEDS moored and anchor station data (Tables 1 and 3), and a monthlong record taken over the midnorthern shelf from an exploration oil platform in 80 m of water (Table 1). M_2 elevation amplitude and phase information from 50 km and greater offshore of the shelf break is taken from CRS91. The M_2 transport cotidal chart (Figure 5) incorporates ADCP data from AMASSEDS cruises 1 (August 1989), 2 (March 1990), 3 (May 1990) and 4 (November 1991),

Table 3. Anchor Station Tidal Measurements Made During AMASSEDS

						M_2 Elevation			M_2 Transport		
Station	Latitude, °N	Longitude, °W	Start Date	Duration, hours	Water Depth, m	Amplitudes, m	Phase, °G	Semimajor Axis, m^2/s	Semiminor Axis, m^2/s	Flood Phase, °G	Inclination, °N
					River Mouth						
RM1	1.250	49.485	Nov. 16, 1991	25	15.4	1.39	38	21.6	3.2	13	23
RM2	1.392	49.396	March 20, 1990	25	13.5	1.33	350	18.0	3.2	325	29
	1.392	49.398	June 12, 1990	11	13.7	.90	16	14.7	4.3	347	32
RM3	1.665	49.161	March 10, 1990	25	10.9	1.07	333	14.5	1.6	294	49
	1.631	49.205	March 21, 1990	12	10.9	1.00	323	11.8	5.5	311	35
	1.689	49.155	June 2, 1990	25	10.9	.91	346	14.3	5.5	305	57
	1.688	49.177	June 12, 1990	12	10.6	1.20	340	13.9	3.0	292	53
					Open Shelf						
OS1	2.885	50.721	March 16, 1990	25	11.8	2.36	294	13.7	−0.3	220	11
	2.928	50.709	June 6, 1990	25	12.0	2.58	275	17.0	1.7	209	14
	2.893	50.709	Nov. 18, 1991	25	13.0	2.31	281	16.1	2.6	214	11
OS2	3.105	50.315	March 15, 1990	25	17.9	1.94	275	26.3	2.3	215	30
	3.111	50.316	June 15, 1990	25	18.2	1.65	263	31.7	5.6	203	31
	3.125	50.297	Nov. 19, 1991	25	18.9	1.22	255	19.7	1.7	200	28
OS3	3.331	50.004	March 12, 1990	25	39.4	1.44	250	31.1	0.4	203	33
	3.335	50.003	June 4, 1990	25	40.3	1.10	252	35.9	0.0	196	36
	3.335	50.000	Nov. 21, 1991	13	38.7	0.74	245	22.4	−0.3	193	32
OS4	2.541	49.773	March 18, 1990	25	17.2	1.71	285	23.9	4.5	218	45
	2.524	49.815	June 10, 1990	15	16.6	1.34	304	20.8	4.9	235	47

Tidal elevation and volume transport measurements were made at anchor stations during AMASSEDS. Owing to the shortness of the anchor stations, only the M_2 constituent was estimated using harmonic analysis and inference from a reference station. The elevation and transport phases are given in degrees Greenwich, indicating the phases of maximum surface elevation and flood (onshore) current. The inclination or orientation of the semimajor axis (during ebb) is given in degrees clockwise relative to north. See Figure 2 for station locations.

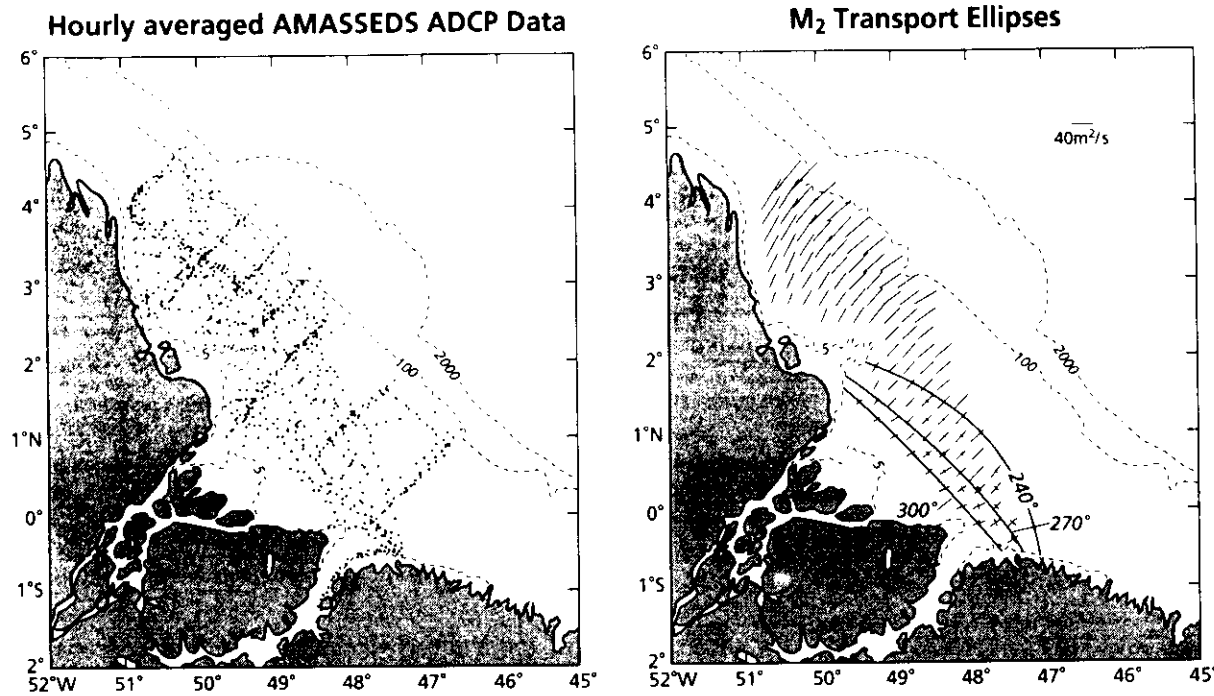

Figure 5. M_2 volume transport cotidal chart for the Amazon shelf based on 1327 hourly averaged acoustic Doppler current profiler (ADCP) transport measurements and anchor and moored current time series collected during AMASSEDS. (left) The distribution of the ADCP data (the locations of the anchor and moored stations shown in Figure 2). (right) The fitted transport ellipses with the phase of maximum flood (onshore) flow given in degrees Greenwich with a contour interval of 30°.

which amount to the 1327 hourly averaged ADCP data points located over the shelf as shown in Figure 5a, and 400 hours of transport observations made at the AMASSEDS M1 and M2 mooring sites (Table 4 and Figure 2). These transport observations have been combined using the empirical analysis technique described by *Candela et al.* [1992] to produce the M_2 transport chart. In this technique the spatial structure of the dominant tidal and steady components are represented by polynomials; the results shown here were obtained with a second-degree polynomial fit for M_2 and first-degree polynomials for the S_2 and steady components.

There is a marked difference in the M_2 tidal behavior in front of the Amazon River mouth and in the northwest shelf as indicated above. Lines of constant phase, contoured over the shelf every 30° (which corresponds to about 1 hour in time) both for elevation and transport, indicate that the tidal elevation signal takes roughly 2 hours to propagate from the shelf break to the coast in the northwest shelf, while the associated transport signal is more nearly simultaneous over the whole northwest shelf. There is a 200% increase in elevation amplitude from the shelf break to the coast in this region. The transport ellipses are nearly perpendicular to the local isobaths and rectilinear (weak ellipticity) over the whole shelf, decreasing in strength toward the coast. The phase difference between elevation and transport is close to 60° over most of the northwest shelf, increasing to about 90° near the coast as expected of a standing wave subject to friction. In front of the Amazon River mouth the tidal elevation signal takes about 5 hours to propagate from the shelf break to the river entrance, with a 50% increase in amplitude at the river entrance with respect to that observed at the shelf break. To the south of the Amazon River mouth the M_2 tide tends to behave similarly to the northwest shelf, i.e., with more of a standing wave character but with weaker cross-shelf amplification.

3.3. M_2 Cotidal Charts for the Lower Amazon and Para Rivers

Next we present M_2 elevation cotidal charts for the lower Amazon and Para Rivers (Figure 6), based on 37 sea level records from within the two rivers (Table 1). The regular pattern observed over the inner shelf in front of the river mouth breaks down as soon as the M_2 tidal wave enters the main Amazon River branches (the North and South Channels) and the Para River. However, the wave propagates with a similar rate in all three channels, showing the same phase (300°) some 350 km into the river mouth as over the inner shelf in front of the river mouth. The M_2 elevation amplitude shows a general decay as it progresses upriver with a more than 70% decrease over a distance of about 350 km from the outermost to the innermost river station considered here. There are strong gradients in amplitude in the narrow channels between the islands separating the North and South Channels. These are particularly large

Table 4a. Semidiurnal Tidal Transport Ellipse Parameters at the AMASSEDS Mooring sites M1–M3

Site	Semimajor Axis, m^2/s	Semiminor Axis, m^2/s	Inclination, °L	Phase, °G
		M2		
M1	24.6 ± 0.5	1.2 ± 0.5	193.5 ± 1.1	210.3 ± 1.1
M2	30.7 ± 0.5	2.6 ± 0.3	188.2 ± 0.6	204.2 ± 0.9
M3	30.8 ± 0.7	−5.4 ± 0.6	189.4 ± 1.3	183.4 ± 1.3
		S2		
M1	4.6 ± 0.6	0.0 ± 0.6	195.1 ± 3.4	249.5 ± 3.2
M2	6.0 ± 0.6	0.5 ± 0.4	185.2 ± 1.7	238.3 ± 2.5
M3	7.3 ± 0.8	−1.5 ± 0.8	193.0 ± 3.3	215.4 ± 3.4
		N2		
M1	4.5 ± 0.5	−0.1 ± 0.5	193.2 ± 6.1	213.9 ± 5.8
M2	5.8 ± 0.5	0.4 ± 0.3	189.1 ± 3.0	199.7 ± 4.6
M3	5.3 ± 0.7	0.5 ± 0.6	191.2 ± 7.1	178.7 ± 7.2

The semimajor and semiminor axes are listed in square meters per second; the inclination or orientation of flood transport is given in degrees local measured counterclockwise from 45°N, the average cross-shelf direction along the moored array transect, and the phase in degrees Greenwich. The mooring site locations, data record lengths, and mean water depth are given below. See Figure 2 for map showing station locations.

in the channels in the eastern region of the river mouth. The main effect of these amplitude gradients is to homogenize the tidal characteristics in the two channels, so that in the inner river mouth the two channels have similar M_2 amplitude and phase values at comparable distances from the seaward end of the river mouth.

The structure of the M_2 tidal wave over the inner shelf region just offshore of the river mouth is particularly complex. From the available data on the tide over the mid- and outer shelf and the shallow depths found in the river mouth we expect the tidal wave to increase its amplitude over the inner shelf within the river mouth before progressing up the narrow channels. However, the specific structure of this increase will depend on the local topography and dissipation processes which are both not well known and may be quite complex. This region needs further direct measurements before the M_2 tidal amplitude (and phase) can be mapped with any certainty.

4. A Dynamical Model for the Amazon Shelf M_2 Tide

The semidiurnal coastal admittance and M_2 cotidal charts presented above suggest that the shelf area between Cabo Norte and Cabo Cassipore is in near resonance at semidiurnal frequencies, while southeast of

Table 4b. AMASSEDS Mooring Site Positions, Local Water Depths, and Transport Record Periods

Site	Latitude, °N	Longitude, °W	Water Depth, m	Start Date, 1990	Record Length, days
M1	3.075	50.313	18	Feb. 9	62
M2	3.385	49.940	65	Feb. 10	65
M3	4.072	49.623	103	Feb. 10	80

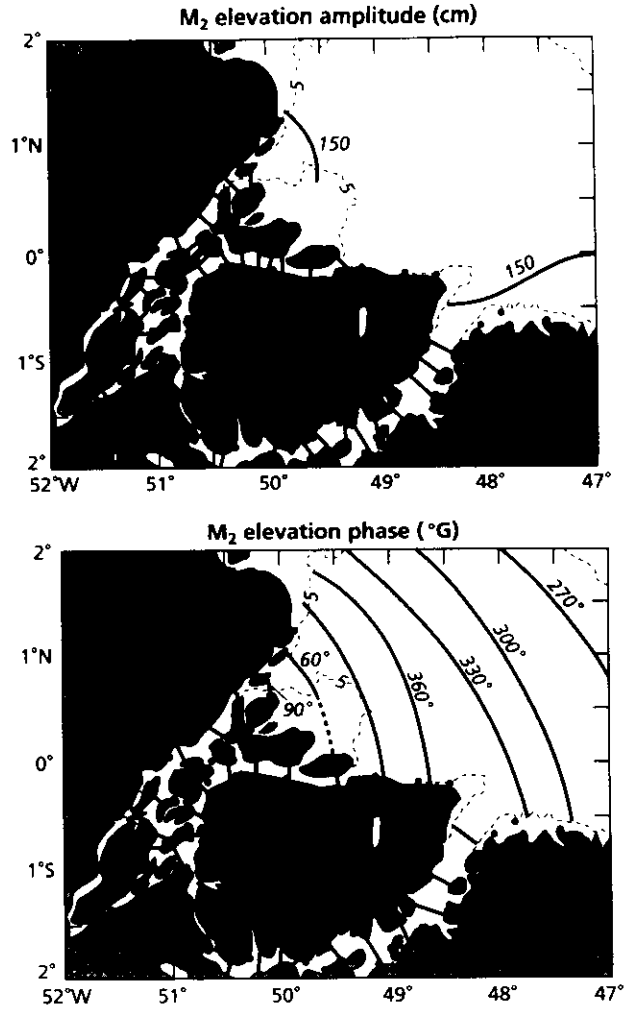

Figure 6. (top) M_2 elevation amplitude (meters) and (bottom) elevation phase (degrees Greenwich) for the Amazon and Para river mouth region. These cotidal charts were drawn from elevation data at coastal and river stations denoted by dots.

Cabo Norte, the Amazon and Para Rivers absorb a small but significant fraction of the incident tidal energy. In this section we present a simple dynamical model to support this conceptual picture of the Amazon shelf tidal response.

The basic model is a numerical version of the simple cross-shelf barotropic tidal model introduced earlier. The governing momentum and continuity equations are

$$\begin{aligned} \frac{\partial u}{\partial t} &= -g\frac{\partial \zeta}{\partial x} - \frac{C_d \mid u \mid u}{h} \quad , \\ \frac{\partial \zeta}{\partial t} &+ \frac{1}{w}\frac{\partial}{\partial x}(whu) = 0 \quad , \end{aligned} \tag{3}$$

where x is the cross-shelf coordinate (positive onshore), ζ is the free surface, u is the onshore velocity, h is the mean water depth, and w is the width of the cross-shelf channel being considered. Any along-shelf variation in forcing or response is ignored. The model dynamics are linear with the exception of bottom stress, which we take to be a quadratic function of velocity, with C_d the drag coefficient. (Experiments conducted with the full nonlinear momentum and continuity equations did not change the model results appreciably, so the simpler dynamics contained in (3) were used. For example, for case B presented in section 4.1, nonlinearity caused a decrease of 4% or less in global quantities like total mechanical energy and dissipation and a maximum decrease in M_2 elevation and transport (primarily nearshore) of 6% or less.) The governing equations are solved numerically on a staggered time and space grid following *Flather and Heaps* [1975] with linear term derivatives approximated with centered differences. The quadratic bottom stress term is also centered in time following *Greenberg* [1983]. The model is driven by the surface elevation specified at the shelf break. Typically, the model equations are integrated for four tidal periods (equilibrium is generally reached after two periods), and the results of the last period are analyzed to determine the tidal constituents and their spatial behavior. The primary benefit of using this numerical approach is to allow us to examine the influence of realistic bottom topography, channel width, and bottom stress on the cross-shelf structure of the M_2 tide.

Current and elevation data were collected at moored and anchor stations located along two cross-shelf transects during AMASSEDS (Figure 2 and Tables 3 and 4). The "open shelf" transect starts at the coast at 2°35′N, 50°50′W and extends across shelf with an orientation of 43°N (chosen to be perpendicular to the regional orientation of the 100-m isobath). The length of this transect from the coast to the 100-m isobath is about 215 km. One coastal tide station and three of the four open shelf anchor stations (OS1–OS3) are located roughly along this transect as are the three moored stations (M1–M3). The "river mouth" transect starts in the North Channel at Punta do Ceu at 0°44′N, 50°07′W, follows the channel to 0°48′N, 50°W, then extends along the channel and across the shelf with an orientation of 43°N. The total length of this transect is about 315 km, with the river mouth sill located roughly 140 km from the transect origin. Two coastal tide stations and the three river mouth anchor stations (RM1–RM3) are located along this transect.

We will apply our model along these two transects and use the tidal observations made there to help select the "best" drag coefficient and channel width (the two free model parameters) and compare with the model results. A combination of depth data obtained from navigation charts and at anchor, moored, and CTD stations was used to determine the model depth profile along each transect. This was straightforward for the open shelf transect but more difficult within the river mouth where the North Channel topography is quite complex (Figures 2 and 12). The model incorporates a no-flux condition at the coast for the open shelf transect. For the river mouth transect the channel depth and width at the origin of the transect is continued 600 km upstream where a simple explicit radiation boundary condition is applied [*Chapman*, 1985]. This allows the incident tidal wave to propagate upstream through the

model river mouth without significant reflection due to the upstream boundary condition.

4.1. The Open Shelf Transect

The model is first applied to the open shelf transect where the topography is simpler and better known and more tidal data are available. To simplify the initial model parameter fitting, the channel width is kept equal to unity and the drag coefficient considered to be constant independent of cross-shelf position. The magnitude of the drag coefficient is then varied to minimize differences between data and model. As shown above (Figure 5), the observed M_2 transport is nearly rectilinear and oriented primarily across the local isobaths in this shelf region. To make the transport data directly comparable with the model transport, the semimajor axis of the M_2 transport observed at the anchor and moored stations and with the ADCP was projected onto the transect. Since the angle between the semimajor axis and the transect is generally less than 15° (except at OS1 where the largest angle is 33°), the reduction in transport amplitude is typically small, less than 5%. The M_2 forcing at the model shelf break is estimated from the M_2 cotidal charts (Figure 4); the values used are $\zeta = 0.80$ m and 233 degrees Greenwich (°G) (this represents a 10% increase in amplitude and 6° phase lag from the values given for 50 km offshore by CSR91).

The model results for the open shelf transect are shown in Figure 7. The best qualitative data/model agreement was obtained with $C_d = 0.0016$. Figure 7a shows the cross-shelf depth profile and, for comparison, a linear depth profile from the coast to the shelf break. The presence of the modern subaqueous delta is clearly seen out to a depth of about 60 m. Figure 7b shows the tidal elevation normalized by the amplitude of the forcing at the shelf break and the elevation phase lag as a function of cross-shelf position. The model-normalized elevation amplitude increases monotonically onshore and reaches a maximum of 3.2 at the coast. All model and observed phases are plotted relative to the phase of the elevation forcing at the shelf break, so that the model elevation phase increases from 0 at the shelf break to about 88° at the coast. Figure 7c shows the model and observed transport amplitude and relative phase. In addition to the anchor and moored transport results, the amplitude and phase of the ADCP-derived transport along the transect is also plotted. (While the cross-shelf shape of the ADCP-derived transport amplitude is consistent with the anchor and moored transport estimates, the ADCP-derived transport values appear to be roughly 10-20% low in comparison. The ADCP-derived transport phase and anchor and moored transport phase estimates agree within about 20°, although their cross-shelf dependencies are opposite. The exact reasons for these differences are not understood, although some part may be due to the spatial smoothing inherent in the polynomial fitting. Despite these differences we believe the basic structure of the M_2 transport field is correctly captured in the cotidal chart shown in Figure 5 even though the transport amplitude may

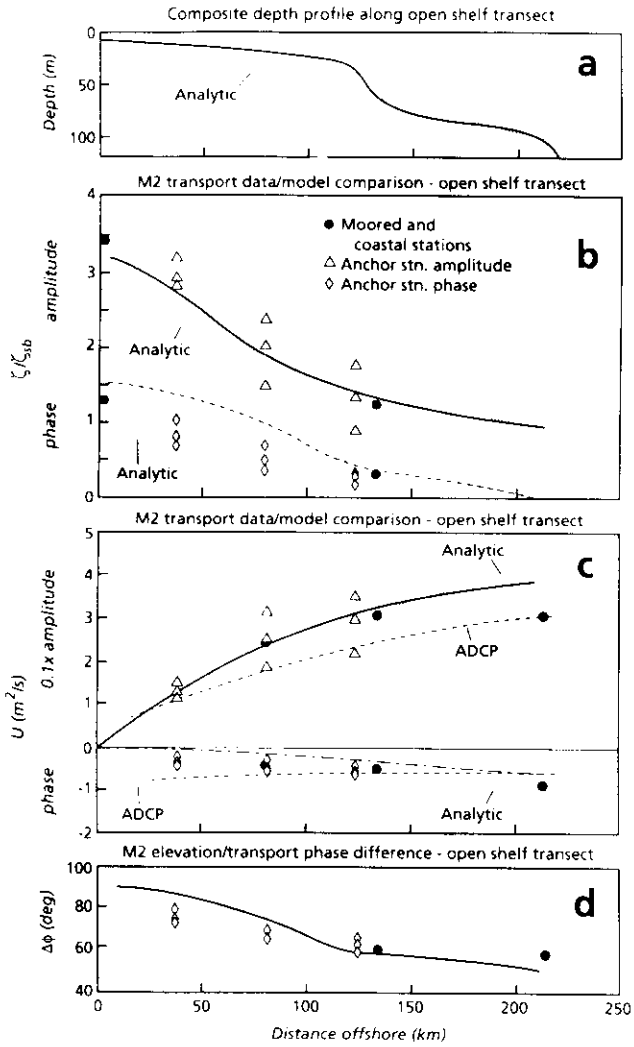

Figure 7. Comparison between constant-width channel model and observations along the open shelf transect. (a) Cross-shelf depth profile, (b) elevation amplitude scaled by shelf break forcing and elevation phase, (c) transport amplitude and phase, and (d) phase difference (in degrees) between elevation and transport. Elevation and transport phases are shown in radians referenced to the phase of the elevation forcing at the shelf break. Elevation and transport measurements from coastal, moored and anchor stations, and the ADCP are shown for comparison with the model predictions. Also shown for comparison are the elevation and transport predicted with an analytic model for the constant-slope depth profile shown in Figure 7a. The analytic model is described in section 3.1; the nondimensional friction parameter $\epsilon = 0.5$.

be underestimated by as much as 20%.) The model transport decreases monotonically onshore from about 39 m^2/s to zero at the coast. Figure 7d shows the model and observed difference between elevation and transport phase. Since the "coast" in the model is really a shallow, vertical wall where the transport must vanish, wave reflection occurs in the model and the model tidal wave

approaches a standing wave at the coast, with elevation and transport approaching 90° out of phase. At the shelf break the model elevation-transport phase difference is about 36°, indicating significant onshore tidal energy flux.

The agreement between model and observed elevation and transport is generally good over the mid- and outer shelf, but over the inner shelf the model overpredicts the phase lag of both elevation and transport. This tendency, plus the overprediction of the elevation-transport phase difference near the coast, suggest that some tidal energy is leaving the transect laterally near the coast. This is supported by the tendency for the observed transport orientation to be more alongshore near the coast (Figure 5). This means that the open shelf transect is located close to but not along the central axis of this shelf region. From the M_2 cotidal charts and shelf geometry we suggest that the central axis is located roughly 70 km to the southeast, where the shelf is widest.

As the first step toward a more realistic model of this shelf region, we now consider a variable-width channel model to fit along the central axis. The channel length is increased by 20 km to 235 km, and the cross-shelf depth profile used above has been extended shoreward to a minimum depth of 5 m at the coast. The channel nondimensional width is allowed to decrease from $w = 1$ over the outer shelf to a value $w_{\min}$ less than 1 at the coast. To simplify the model, only a linear variation in w is considered, with x_w being the distance from shore where w starts to decrease. Numerical experiments were conducted with different $w_{\min}$, x_w, and C_d, and the results were compared with the open shelf transect data described above plus additional tidal data from one coastal station, one outer shelf pressure station, and the open shelf anchor station OS4 (see Figure 2). In this model/data comparison we consider all data to be representative of conditions along the centerline and thus plot the observed data as a function of distance offshore from the new model coast.

The results of this variable-width centerline model are presented in Figure 8. The best qualitative model/data agreement was obtained with a $w_{\min} = 0.3$, $x_w = 90$ km, and $C_d = 0.0013$. This choice of channel width appears consistent with the shelf geometry (see Figure 2) and is shown in Figure 8a with the cross-shelf depth profile. As before, the normalized elevation amplitude (Figure 8b) increases monotonically onshore but now reaches a maximum of about 3.9 at the coast. The elevation phase lag also increases monotonically onshore but now is approximately linear across the inner shelf, reflecting the competing tendencies for the phase speed to decrease with decreasing water depth and increase with decreasing channel width. The model transport (Figure 8c) decreases monotonically onshore from about 40 m^2/s to zero at the coast, exhibiting a slight kink at $x = 90$ km where the channel starts to converge. The model transport phase lag increases shoreward from the shelf break, with an approximately linear phase speed over the inner shelf. The phase difference be-

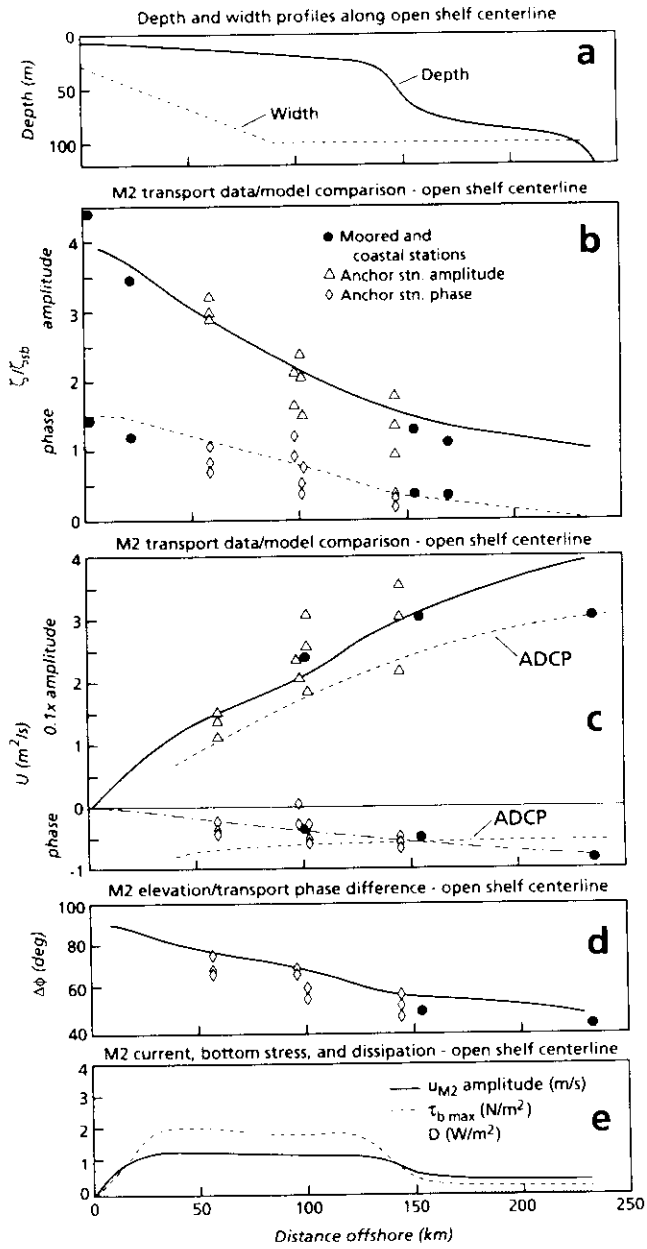

Figure 8. Comparison between variable-width channel model and observations along the open shelf centerline. (a) Cross-shelf depth and channel width profiles, (b) elevation amplitude scaled by shelf break forcing and elevation phase, (c) transport amplitude and phase, (d) phase difference (in degrees) between elevation and transport, and (e) distribution of M_2 current amplitude, maximum bottom stress, and dissipation. As in Figure 7, elevation and transport phases are shown in radians referenced to the phase of the elevation forcing at the shelf break, and elevation and transport measurements from coastal, moored and anchor stations, and the ADCP are shown for comparison with the model predictions. To simplify plotting, the channel width profile has been scaled in Figure 8a to equal 100 at the shelf break; the actual shape is shown superimposed on the shelf topographic map in Figure 2.

tween model elevation and transport at the shelf break is now about 45°(Figure 8d). Figure 8e shows the cross-shelf distributions of model velocity amplitude, maximum bottom stress, and dissipation. The model velocity, bottom stress, and dissipation reach maximum values of 1.26 m/s, 2.06 N/m^2, and 1.27 W/m^2, respectively, near $x = 40$ km over the inner shelf within the channel convergence. The total dissipation equals the onshore energy flux of 1.05×10^5W/m at the shelf break.

The above results demonstrate that reasonable agreement between model and observed data for the M_2 tide can be obtained in this shelf region with a simple variable-width cross-shelf channel model. For this model geometry most of the tidal energy dissipation occurs over the inner shelf in water depths less than 20 m. Over the inner shelf the tide propagates with a phase speed set primarily by the water depth and channel width (with bottom friction being relatively unimportant). These two parameters also set, for the most part, the phase difference between elevation and transport. Since decreasing the minimum width of the coast $w_{\min}$ (thus increasing the channel convergence) increases the tidal phase speed but decreases the elevation-transport phase difference, model/data comparisons (not shown) clearly suggest that $w_{\min} = 0.3$ with a maximum uncertainty of ± 0.1. The uncertainty in choosing C_d is roughly ± 0.0002.

The above model results were obtained with a constant C_d. There is good reason to believe that the actual C_d is not uniform across the shelf. Over the outer shelf the bottom consists of coarse relict sands with bed forms and sand waves oriented across the local isobaths, roughly parallel to the tidal currents [*Nittrouer et al.*, 1983]. Near-bottom current measurements made with a bottom tripod system (Geoprobe) at a water depth of 65 m at the M2 mooring site by *Cacchione et al.* [1995] allow bottom stress there to be estimated using tidal log-layer theory [*Soulsby and Dyer*, 1981]. A regression of the M_2 component of bottom stress against $|u|u$, where u is the depth-averaged M_2 velocity, yields $C_d = 0.0027$, which is probably representative of C_d over the outer shelf. Since less than 4% of the model tidal energy dissipation occurs over the outer shelf, increasing C_d there to 0.0027 does not change the model solution significantly (Table 3). This implies that C_d over the inner shelf must be significantly smaller than the outer shelf value in order to achieve the shelf-wide value of 0.0013 suggested by the variable-width model fit.

The Amazon inner shelf region is noted for fluid muds which can cover large areas as a bottom layer of highly concentrated suspended sediment (with concentrations greater than 10 g/L). As part of AMASSEDS, a small, instrumented tripod developed by *Sternberg et al.* [1991] was used to obtain high-resolution vertical profiles of suspended-sediment concentration, current speed and direction, temperature, and conductivity. Measurements made with this system during hydrographic surveys and anchor stations plus other bottom observations have allowed *Kineke and Sternberg*

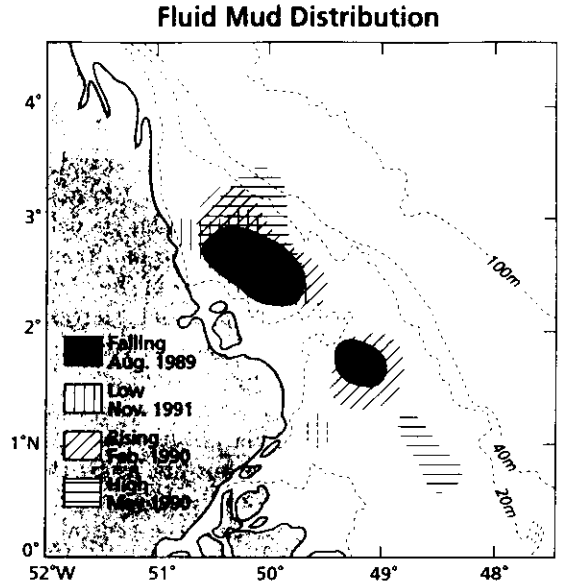

Figure 9. Distribution of fluid mud layers found over Amazon shelf during the four AMASSEDS cruises. These patterns are based on suspended-sediment profile measurements and other bottom sampling conducted during various legs during each cruise. Figure is redrawn from *Kineke and Sternberg* [1995].

[1995]) to construct maps illustrating the spatial extent of the fluid mud layers found during the four AMASSEDS cruises (Figure 9). A sequence of vertical profiles of velocity, salinity, and suspended-sediment concentration obtained over one tidal cycle at the open shelf anchor station OS2 during March 15, 1990, is shown in Figure 10 to illustrate the general structure of an Amazon shelf fluid mud layer and its pronounced effect on the vertical structure of velocity. Note that despite the very large tidal currents (in excess of 1 m/s) and shallow water depth (less than 20 m), the velocity shear is concentrated in a relative thin (2–4 m thick) bottom layer (which includes the thinner fluid mud layer), above which the velocity is more constant with height above the bottom [*Geyer and Kineke*, this issue]. Analyses of the velocity profiles obtained at this anchor station by Geyer and Kineke suggest that the effective drag coefficient felt by the overlying fluid during that 25-hour period was about 0.00016, only 12% of the value used in the basic solution presented above, and only 6% of the value obtained from the Geoprobe measurements over the outer shelf. The large stable stratification caused by the suspended sediment occurring in the fluid mud layer apparently tends to inhibit the vertical turbulent eddy flux of momentum within the layer, thus reducing the turbulent drag on the fluid above the fluid mud layer [*Trowbridge and Kineke*, 1994]. Since fluid mud layers can be found over much of the inner shelf in this region, we conclude that they locally lower the drag on the M_2 transport and result in a spatial and temporal mean value of C_d close to that given by the best model

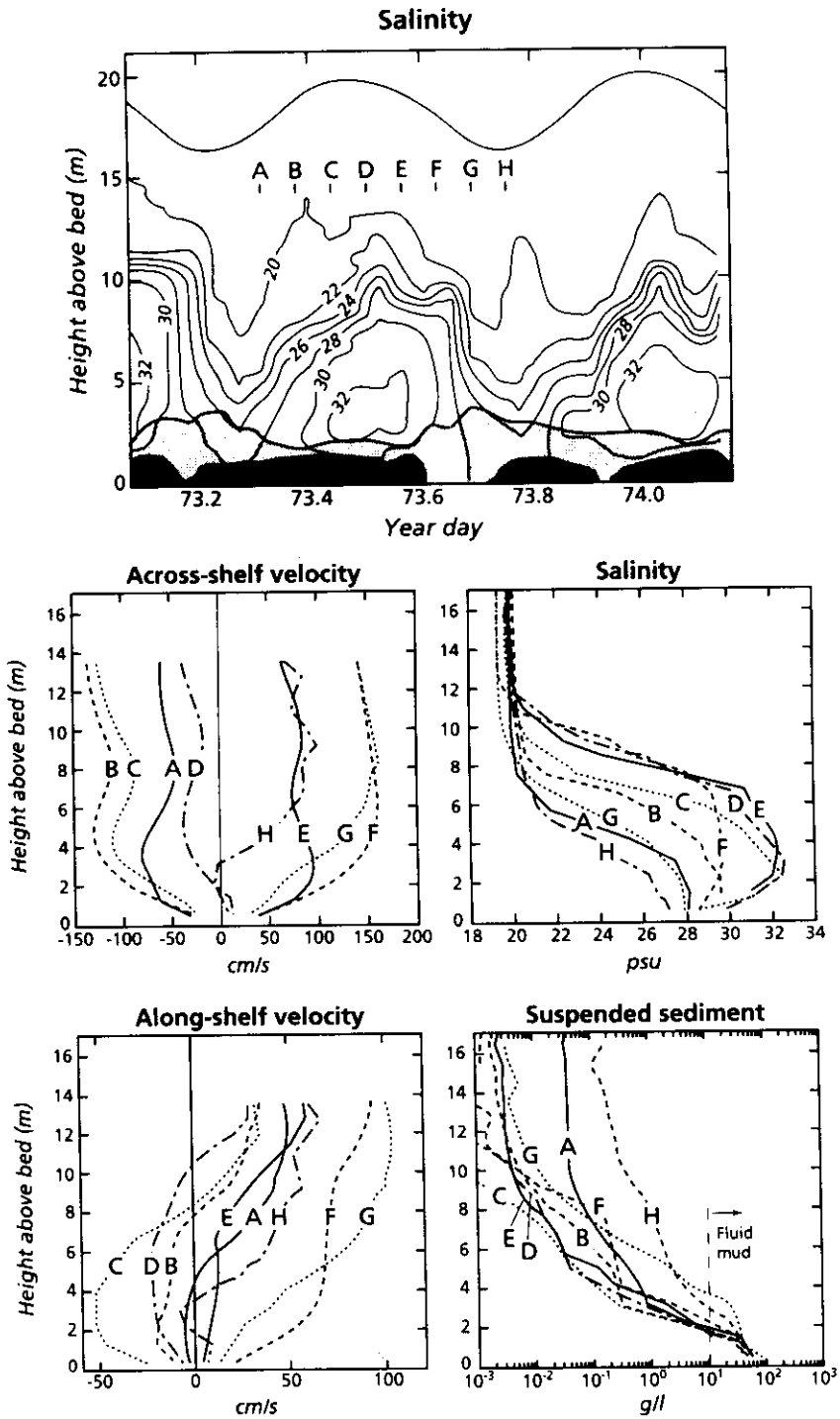

Figure 10. Tidal variations of velocity, salinity, and suspended sediment at open shelf anchor station OS2 on March 15, 1990. (top) Salinity, water depth, and fluid mud layer as a function of time through a 25-hour sampling period. The fluid mud layer is shown as stippled, with suspended sediment concentrations exceeding 10 g/L and 50 g/L, indicated by light and dark stippling, respectively. Remaining panels show vertical profiles of along- and cross-shelf current, salinity, and suspended-sediment (as labeled) observed at 2-hour intervals during the times indicated in the top panel. Note that the region of high shear in the cross-shelf velocity profiles is confined to the lowest 2–5 m, indicating that most of the tidal boundary layer occurs in the fluid mud layer. This figure adapted from *Geyer and Kineke* [this issue].

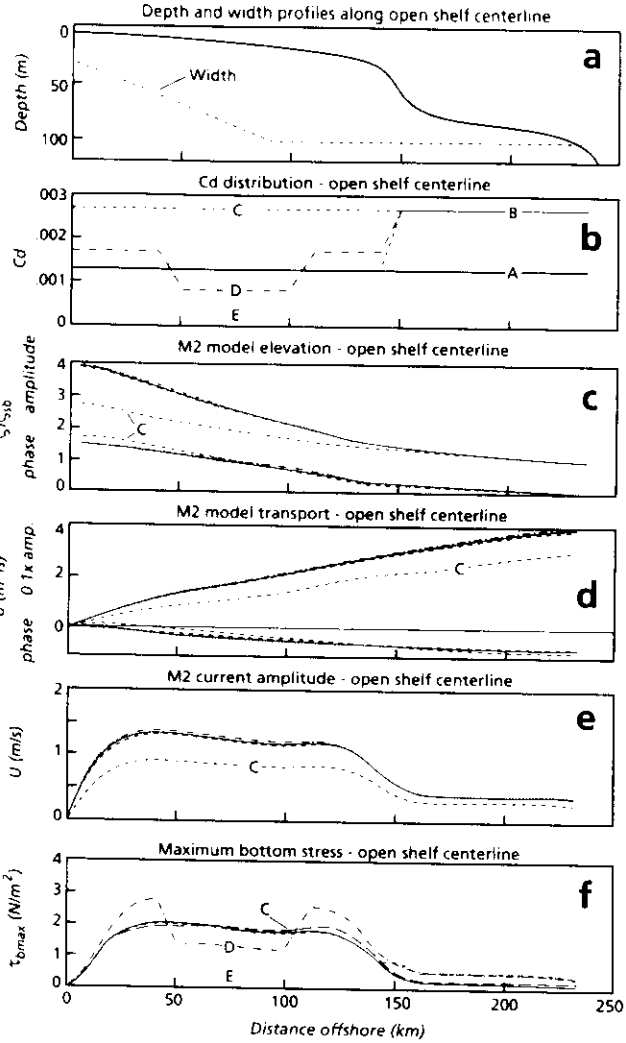

Figure 11. Sensitivity study of open shelf variable-width channel model to variations in bottom friction coefficient C_d. (a) Cross-shelf depth and channel width profiles, (b) cross-shelf profiles of C_d for five cases (case A–case E), (c) scaled elevation amplitude and phase, (d) transport amplitude and phase, (e) current amplitude, and (f) maximum bottom stress distribution. Note that there is little variation in elevation and transport except for case C. See Table 5 for details of the five cases.

fit, 0.0013. (While values of C_d found in the literature vary widely, we note that *Uncles and Stephens* [1990] found good agreement between observed elevations and currents in the Tamar Estuary and a cross-sectionally averaged numerical tidal model using $C_d = 0.0016$. Located in southwestern England, the Tamar Estuary is known to have intertidal mud flats and fluid muds in its upper reaches [*Stephens et al.*, 1992]. *Giese and Jay* [1989] found that the large near-bottom stratification associated with the salt wedge in the lower Columbia River estuary reduced the effective C_d on tidal flow to $C_d = 0.0008$, which is the lowest value reported in the literature to our knowledge.)

To examine the sensitivity of the basic model to spatial variation in C_d, we show in Figure 11 and Table 5 results for five different cross-shelf C_d distributions as follows: case A, $C_d = 0.0013$ everywhere (the basic case presented above); case B, $C_d = 0.0013$ except over the outer shelf ($h > 44$ m) where $C_d = 0.0027$; case C, $C_d = 0.0027$ over the entire shelf; case D, $C_d = 0.0027$ over the outer shelf and $C_d = 0.0017$ over the inner shelf except between $x = 50$ and 100 km where $C_d = 0.0008$, and case E, $C_d = 0.0027$ over the outer shelf and $C_d = 0.0022$ over the inner shelf except between $x = 50$ and 100 km where $C_d = 0.0002$. Case C represents the situation where the outer shelf C_d is applied over the entire shelf. Cases D and E represent possible further reductions in C_d from the basic case due to a discrete band of fluid mud located between 50 and 100 km offshore, with the minimum value of C_d in case E picked to be consistent with the lowest values of C_d estimated at anchor stations in fluid muds by W. R. Geyer and J. H. Trowbridge (personal communication, 1993). In both cases D and E, the intermediate value of C_d used for the rest of the inner shelf was chosen to give a constant spatial average of C_d over the inner shelf of 0.0013.

Applying the outer shelf $C_d = 0.0027$ over the entire shelf (case C) leads to a significant (and clearly unrealistic) underprediction of elevation and transport, while increasing the outer shelf C_d from the basic case value of 0.0013 (case A) to 0.0027 (case B) makes very little difference since so little dissipation occurs over the outer shelf. Since the spatially averaged C_d over the inner shelf is constant in cases A, B, D, and E, decreasing C_d in the inner shelf fluid mud band while increasing C_d over the rest of the inner shelf (cases D and E) has little net effect on the elevation and transport fields over the shelf. This spatial variation in C_d does lead to large variations in bottom stress over the inner shelf, with maximum bottom stresses in and just outside the fluid mud band for case E. The possible implications of this bottom-stress distribution on the formation and maintenance of the fluid mud layers will be discussed later. We conclude from this sensitivity study that while fluid mud layers occurring over the inner shelf may locally lower the effective C_d to minimum values near 0.0002, the large scale of the M_2 tide integrates over smaller-scale variations in C_d. This result strengthens our earlier conclusion that fluid muds must lead to a significant reduction in the spatial and temporal mean C_d over the inner shelf as indicated by the best model/data fit.

The above results suggest that we can consider the Amazon shelf between Cabo Norte and Cabo Cassipore as a large coastal embayment into which the semidiurnal tide propagates from the open ocean. In general, the degree of tidal amplification depends on both the characteristics of the embayment (i.e., water depth, channel length and width, and bottom-friction coefficient) and the tidal forcing at the shelf break (elevation amplitude and frequency). To examine the resonant properties of this embayment over the semidiurnal tidal band, we determined the resonant period and quality factor Q for the five cases presented in Table 5 as follows. Model runs were made for each case with fixed ζ_{sb} but different σ, and the σ which maximized the total mechanical

Table 5. Results of Five Sensitivity Experiments

		Case				
		A	B	C	D	E
$10^3\ C_d$	Outer shelf	1.3	2.7	2.7	2.7	2.7
	Inner shelf	1.3	1.3	2.7	1.7	2.2
	FM band	1.3	1.3	2.7	0.8	0.2
KE, 10^9 J/m		0.96	0.94	0.52	0.99	1.07
PE, 10^9 J/m		1.39	1.35	0.87	1.41	1.49
TE, 10^9 J/m		2.35	2.29	1.39	2.40	2.56
TD, 10^5 W/m		1.05	1.05	0.79	1.09	1.13
ζ_c/ζ_{sb}		3.90	3.85	2.72	3.93	3.99
ϕ_c, deg		86.8	87.6	100.5	89.1	89.9
$u_{\max}$, m/s	at 40 km	1.26	1.25	0.86	1.30	1.40
$\tau_{b_{\max}}$, N/m^2	at 40 km	2.06	2.03	2.02	2.82	4.04
$D_{\max}$, W/m^2	at 40 km	1.27	1.22	0.88	1.72	2.41
Q_{res}		2.94	2.89	2.36	2.91	2.97
T_{res}, hours		11.8	11.9	11.6	11.8	11.7

Five numerical experiments to test the sensitivity of the variable-width channel model to cross-shelf variations in the bottom drag coefficient C_d were conducted within the Cabo Norte–Cabo Cassipore embayment. Case A represents the standard case shown in Figure 8; case B has a larger and more realistic C_d over the outer shelf; case C applies that larger, outer shelf C_d over the entire shelf; and cases D and E represent possible further reductions in C_d from the standard case due to a discrete band of fluid mud (FM) located between 50 and 100 km offshore. In both cases D and E, the intermediate value of C_d used for the rest of the inner shelf was chosen to give a constant spatial average of C_d over the inner shelf of 0.0013, the value used in the standard case. Results listed include the total kinetic energy (KE), potential energy (PE), total energy (TE), total dissipation (TD), ratio of coastal elevation to shelf break elevation, coastal elevation phase lag, and maximum M_2 current, bottom stress, and dissipation. The quality factor Q at the resonant period and the resonant period for each model configuration are given at the bottom. Here $Q = \sigma$ TE/TD (see *Godin* [1992] for discussion of definition and applicabilty of Q to tidal studies).

energy within the embayment was taken as the resonant frequency. With the exception of case C (which we consider to be unrealistic) the resonant period for the other four cases varied from 11.7 to 11.9 hours and Q from 2.8 to 3.0. For case B (perhaps the most realistic case) the resonant period is 11.9 hours and the average energy dissipation per forcing period is roughly $2\pi/Q = 2.2$ times the average mechanical energy in the embayment. Since dissipation is relatively large (leading to a small Q), the amplification does not vary much over the semidiurnal band, with less than a 4% decrease in elevation amplitude at the coast as the frequency is increased from N_2 to S_2. This suggests that the tidal response of the Cabo Norte to Cabo Cassipore embayment should be quite similar over the entire semidiurnal band.

4.2. The River Mouth Transect

The variable-width channel model is next applied to the river mouth transect where the topography is much more complex (Figures 2 and 12), and the anchor station data (Table 3) are less certain. (The anchor station tidal results were obtained by simple harmonic analysis using a long nearby current or pressure time series as a reference station. For the open shelf anchor stations the long pressure and current records from the M2 mooring site were used for reference. These stations were located close enough that the relative amplitudes and phases of the semidiurnal constituents should be quite similar. Unfortunately, the closest suitable reference station for the river mouth anchor stations was Salinapolis (or Belem). It is unknown how much error or uncertainty this introduced into the river mouth anchor station tidal results.) A simplified channel depth profile was developed from navigation charts and shipboard measurements in which the river mouth sill is represented as a broad plateau 100 km wide and 10 m deep. Since the mean river discharge velocity in the North Channel is estimated to be less than 5% of the local gravity wave speed $[(gh)^{1/2}]$, we ignore the mean

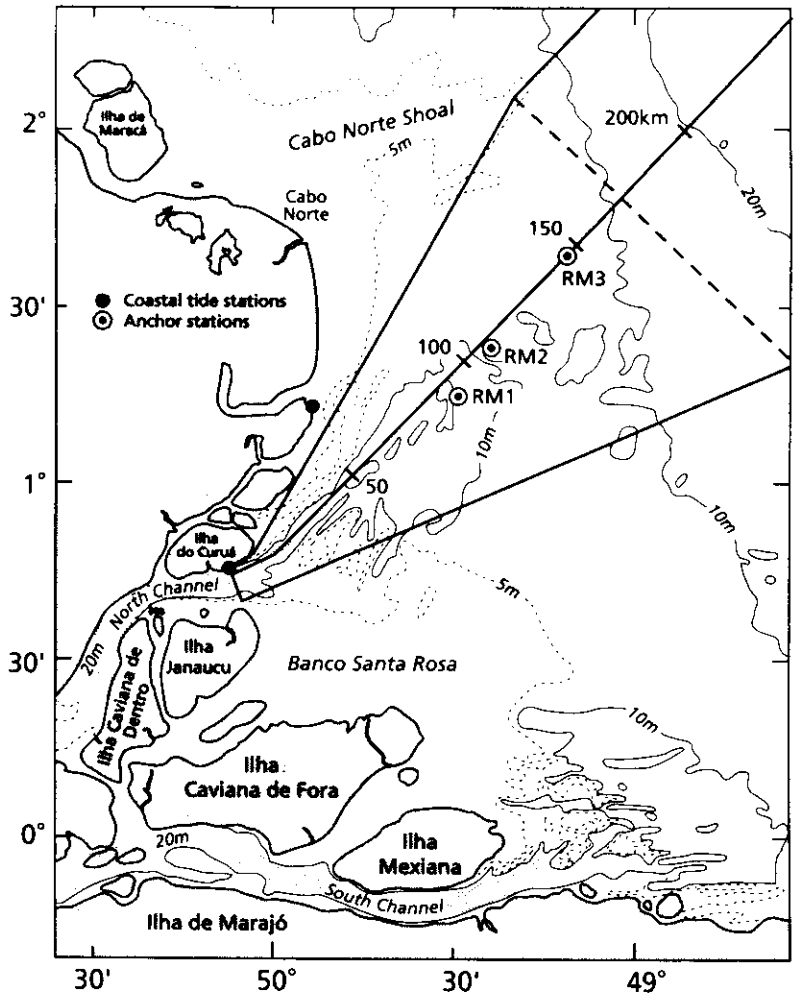

Figure 12. Topographic map of the Amazon River mouth, showing the locations of the three river mouth anchor stations (RM1–RM3) and two coastal sea level stations and the shape of the variable-width channel used to model the M_2 tide across the shelf and into the North Channel. The 5-, 10-, and 20-m isobaths are shown for reference; note the complex topography within each channel, the large bank (Banco Santa Rosa) and shore-parallel shoal between channels, and the large shore-perpendicular Cabo Norte Shoal.

river discharge in the model velocity field. To simplify the model parameter fitting, the drag coefficient over the outer shelf was kept equal to 0.0027 and C_d over the inner shelf varied and the channel width was varied linearly. Fluid muds were found at stations within the river mouth area during AMASSEDS (Figure 9), so we should expect to see some reduction in C_d over the inner shelf as found to the northwest. As shown above (Figure 5), the observed M_2 transport is nearly rectilinear and oriented primarily along the channel axis and thus parallel to the river mouth transect. To make the transport data directly comparable with the model transport, the semimajor axis of the M_2 transport observed at the anchor stations and with the ADCP was projected onto the transect. Since the angle between the semimajor axis and the transect is less than 20°, the reduction in transport amplitude is typically small, less than 4%. The M_2 forcing at the model shelf break was estimated from the M_2 cotidal maps (Figure 4); the values used are $\zeta = 0.85$ m and 245°G (this represents a 10% increase in amplitude and 12° phase lag from the values given for 50 km offshore by CSR91).

The model results for the river mouth transect are shown in Figure 13. The best qualitative data/model agreement was obtained with a channel width which decreased from $w = 1$ at $x = 170$ km to $w_{\min} = 0.08$ at $x = 0$ km (see Figure 12) and an inner shelf $C_d = 0.001$. Figure 13a shows the cross-shelf channel depth and width profiles. The modern subaqueous delta extends out to a depth of about 60 m at $x = 250$ km. The depth of the idealized model river mouth sill between $x = 40$ and 140 km is 10 m, and the river upstream of $x = 0$ km has a depth of 17.5 m. The normalized model elevation amplitude (Figure 13b) increases onshore to a local maximum of about 1.3 at the start of the channel convergence at $x = 170$ km and then increases to about 2 within the convergence toward $x = 0$ km. The model elevation phase increases from

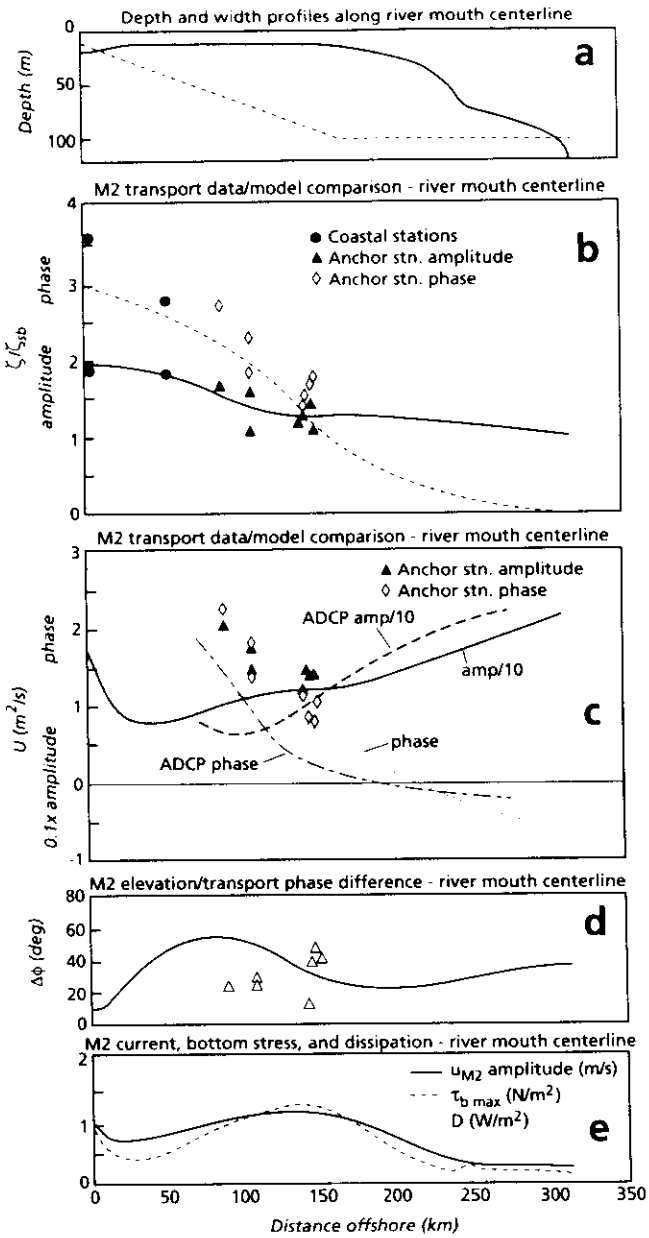

Figure 13. Comparison between variable-width channel model and observations along the river mouth centerline. (a) Cross-shelf depth and channel width profiles, (b) elevation amplitude scaled by shelf break forcing and elevation phase, (c) transport amplitude and phase, (d) phase difference (in degrees) between elevation and transport, and (e) distribution of M_2 current amplitude, maximum bottom stress, and dissipation. As in Figure 7, elevation and transport phases are shown in radians referenced to the phase of the elevation forcing at the shelf break, and elevation and transport measurements from coastal, moored and anchor stations, and the ADCP are shown for comparison with the model predictions. To simplify plotting, the channel width profile has been scaled in the Figure 13a to equal 100 at the shelf break; the actual shape is shown in Figure 12.

0 at the shelf break to about 172° at $x = 0$ km. The model transport (Figure 13c) decreases monotonically onshore from about 22 m^2/s at the shelf break to a minimum of 8 m^2/s at $x = 40$ km before increasing to almost 18 m^2/s at $x = 0$ km, owing to the channel convergence. The model difference between elevation and transport phase (Figure 13d) decreases onshore over the outer shelf and then increases over the inner shelf until about $x = 80$ km where the phase difference decreases rapidly to about 10° at $x = 0$ km, indicative of a relatively weakly damped progressive wave propagating upriver. The model M_2 velocity amplitude, maximum bottom stress, and mean dissipation (Figure 13e) all show relative maxima at the offshore edge of the river mouth sill at $x = 140$ km. The maximum current is 1.14 m/s, only 9% smaller than that found over the inner shelf to the northwest, however, the maximum bottom stress and dissipation are reduced by roughly 35% and 45% owing to the decrease in both current amplitude and the inner shelf C_d from 0.0013 to 0.001. The incident model M_2 energy flux at the shelf break is 7.1×10^4 W/m, of which about 81% is dissipated over the inner shelf and 19% propagates upriver at $x = 0$ km.

The agreement between model and observed elevation and transport along the river mouth transect (Figure 13), although not as good as in the open shelf channel (Figure 8), supports the basic conceptual model of treating this shelf/river mouth region as a convergent cross-shelf channel. The lack of agreement is probably due in part to the complexity of the river mouth geometry, the paucity of long-term observations, and the oversimplification of the model. To determine if the basic results shown in Figure 13 are sensitive to changes in channel geometry and C_d distribution, model runs were made with different depth and width profiles and C_d distributions inshore of 170 km. The model results (not shown) suggest that (1) the convergence in the river mouth channel must extend offshore to at least 150 km, (2) reasonable variations in w_{min} from 0.06 to 0.10 and in the bottom depth profile over the inner shelf do not change the basic character of the tidal wave within the convergence, and (3) the effective inner shelf C_d must be of order 0.001 ± 0.0002. We conclude that fluid mud layers found in the Amazon River mouth significantly reduce the bottom friction felt by the incident tide within the river mouth.

5. Vertical Structure of M_2 Currents at M2

We describe here the vertical structure of the M_2 tidal current at the open shelf siteM2, based on moored current measurements. This site is located on the outer edge of the Amazon shelf delta in 65 m of water (Figures 2 and 7). On February 9, 1990, a surface toroid mooring was deployed at M2 supporting three vector-averaging current meters (VACMs) at design depths of 3, 32, and 54 m. VACMs are normally deployed with the current speed (rotor) and direction (vane) sensors at the bottom of the instrument housing, however, here

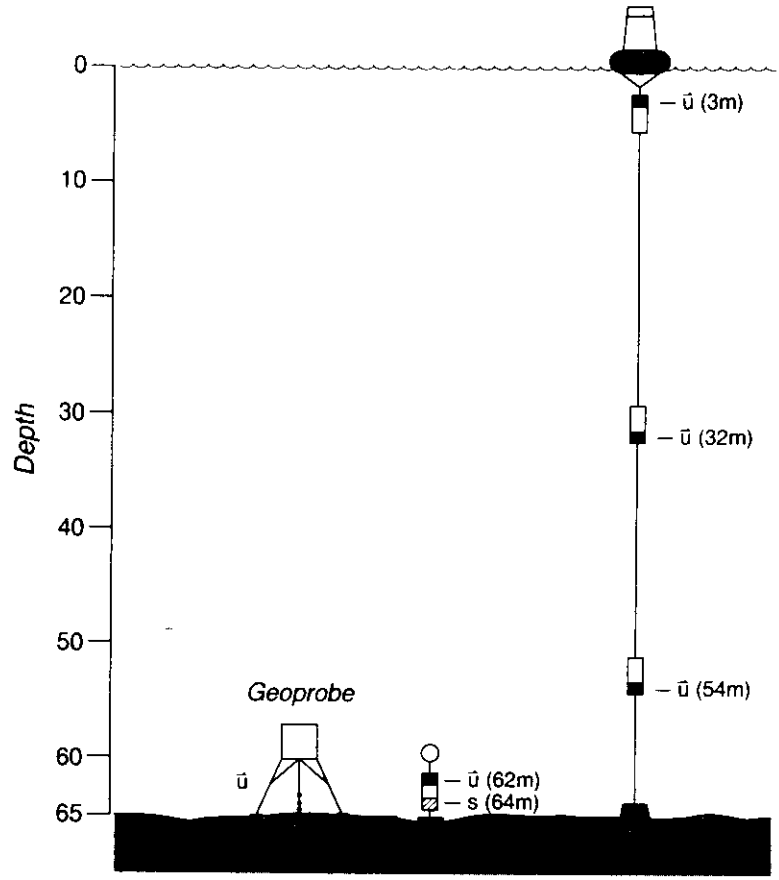

Figure 14. Schematic of M2 moored instrumentation used to study vertical structure of tidal currents. Instrument depths are approximate. The Geoprobe was equipped with three electromagnetic current meters which recorded useful current data. The surface M_2 tide at this site has an amplitude of 1.04 m.

the topmost VACM was deployed inverted to place the current sensors as close to the surface as possible in order to sample in the Amazon surface plume [*Lentz*, this issue; *Lentz and Limeburner*, this issue]. To sample close to the bottom, a short subsurface mooring was deployed which supported a dual-rotor, inverted VACM designed to measure speed at a nominal height of 2.07 m above bottom (mab) and velocity at 3.97 mab. The dual-rotor VACM also measured pressure, and all VACMs were equipped with SeaBird conductivity sensors. On February 11, 1990, the bottom tripod Geoprobe was deployed at M2. This system used Marsh–McBirney electromagnetic current sensors to measure currents at four nominal levels above the bottom (0.27, 0.60, 0.97, and 1.30 mab) and was also equipped with an acoustic altimeter to measure instrument height above the bottom as well as pressure, temperature, and suspended-sediment sensors [*Cacchione and Drake*, 1979]. A schematic of the moored instrumentation deployed at M2 is shown in Figure 14.

The bottom surfacial sediment at M2 was extremely fine grained (mean grain size about 1.0 μm [*Cacchione et al.*, 1995]. As a result, both the Geoprobe and subsurface mooring sank into the seabed upon deployment. Within the first 6 hours after touchdown, the Geoprobe sank about 47 cm into the seabed, burying the lowest current sensor. Then over the next 5 days the Geoprobe slowly sank an additional 3 cm. On February 25 the seafloor suddenly rose about 44 cm around Geoprobe over a 14-hour period, burying all but the top current sensor [*Cacchione et al.*, 1995]. The initial sinking of Geoprobe and this later burial event effectively reduced the period of current and pressure data useful for tidal analysis to 1700 UT on February 11 to 1500 UT on February 25 (period A). The nominal heights of the top three Geoprobe current sensors during this period are taken as the design height minus 49 cm, yielding heights of 0.11, 0.48, and 0.81 mab, respectively.

The penetration of the subsurface mooring into the seabed cannot be determined directly from the VACM pressure record. Instead, the following method was used to estimate the heights of the two VACM rotors above bottom. The Geoprobe and subsurface mooring were deployed about 0.7 km apart. Assuming that the bottom boundary layer structure and bottom stress are constant over that separation and that the unstratified steady state log layer extends up to the upper VACM rotor during maximum flood and ebb currents (as suggested by *Cacchione et al.* [1995]), we solve the following equation for the height above bottom of the lower rotor

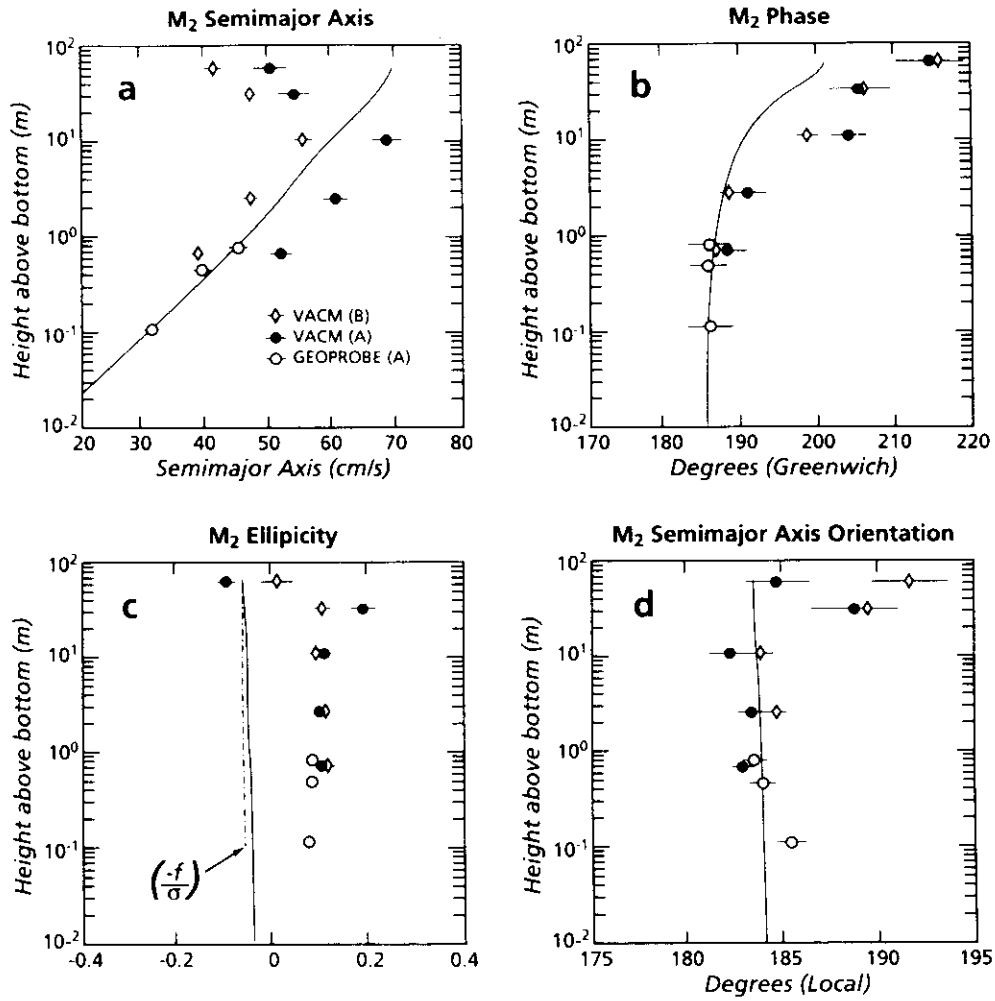

Figure 15. Vertical structure of the M_2 current ellipse parameters at the M2 mooring site. (a) The semimajor axis, (b) the phase, (c) ellipticity (ratio of semiminor to semimajor axes), and (d) orientation. A positive ellipticity indicates counterclockwise rotation of the current vector with time. The orientation of flood is given counterclockwise relative to 45°N, the local cross-isobath direction, so that an orientation of 180°L (local) indicates that flood (the semimajor axis) is pointing directly onshore across the local isobaths. The results of tidal analysis of the Geoprobe and vector-averaging current meter (VACM) data for period A and VACM data for period B are shown together for comparison. The horizontal brackets represent the standard error in the ellipse parameters based on the tidal fit (see Appendix A) and do not include any estimation of instrument measurement error (see Appendix B). The solid lines represent the parameter profiles obtained from the eddy viscosity model. The experimental and model results have been plotted as a function of height above bottom using a logarithmic scale to allow clear display of the near-bottom results and to illustrate the approximate log-layer behavior of the near-bottom velocity.

$$z_\ell = \frac{\Delta z}{e^{\left(\frac{\Delta u}{k u_*}\right)} - 1}, \tag{4}$$

where Δz is the vertical separation of the VACM rotors, Δu is the difference in rotor speed between upper and lower rotors, u_* is the Geoprobe-derived friction velocity, and k is von Karman's constant ($k = 0.4$). While there is much scatter in the resulting 53 estimates of z_ℓ (varying between 0.24 and 1.23 m), the mean $z_\ell = 0.70 \pm 0.24$ m, suggesting that the subsurface mooring had sunk on average roughly 1.37 m into the seabed during period A. The resulting height above bottom of the lower and upper VACM rotors are then 0.70 and 2.68 mab. The values of u_* for these 53 profiles ranged from about 1.3 to 3.0 cm/s. The resulting z_0 ranged from 0.03 to 1.82 cm, giving a mean value of $z_0 = 0.1 \pm 0.3$ cm, in good agreement with the mean value of $z_0 = 0.3$ cm for period A reported by *Cacchione et al.* [1995].

The M2 surface buoy broke free on April 16, 1990, and the three VACMs which dropped to the bottom were later recovered through dragging. These three instruments provided good current data for the period of 0100 UT on February 10 to 1100 UT on April 16 (period B), which overlaps the period of useful Geoprobe current data. The subsurface mooring was recovered

Table 6. M_2 Current and Bottom Stress Ellipse Parameters at AMASSEDS Mooring Site M2 for Period A

Height Above Bottom, m	Semimajor Axis, cm/s	Semiminor Axis, cm/s	Inclination, °L	Phase, °G	Instrument Type
62.0	50.7 ± 2.7	−4.8 ± 1.0	184.8 ± 1.7	214.4 ± 4.5	VACM
33.0	54.2 ± 2.7	10.3 ± 1.3	188.8 ± 2.2	205.2 ± 4.1	VACM
11.0	68.9 ± 2.2	7.5 ± 0.9	182.3 ± 1.1	203.9 ± 2.5	VACM
2.68*	60.7 ± 1.9	5.6 ± 0.4	183.4 ± 0.6	190.6 ± 2.5	VACM
0.81	45.2 ± 1.5	3.7 ± 0.3	183.5 ± 0.6	185.6 ± 2.7	Geoprobe
0.70*	52.0 ± 1.8	5.0 ± 1.3	182.9 ± 0.6	187.7 ± 2.7	VACM†
0.48	39.6 ± 1.3	3.2 ± 0.3	183.9 ± 0.7	185.4 ± 2.7	Geoprobe
0.11	31.5 ± 1.1	2.3 ± 0.3	185.4 ± 0.7	185.5 ± 2.8	Geoprobe
τ_b	5.6 ± 0.6	0.5 ± 0.1	183.4 ± 1.3	182.2 ± 8.6	Geoprobe

Period A covered 1800 UT on February 11 to 1300 UT on February 25, 1990, when the Geoprobe and vector-averaging current meters (VACMs) deployed there provided simultaneous current measurements. The inclination or orientation of flood current is given in degrees local measured counterclockwise from 45°N, the average cross-shelf direction along the moored array transect.

*Value denotes estimated height.
†The lower rotor of the dual-rotor VACM was used.

August 12 and returned good current data through period B and good pressure data through 0900 UT on August 11. As a result, tidal analyses of the Geoprobe and VACM current and pressure data were conducted for their 13.8-day common time period (period A), and similar analyses were conducted on the longer VACM data during the 65.5-day period B (see Appendix A for details).

The resulting estimates of the M_2 current ellipse parameters for periods A and B are shown in Figure 15 and listed in Tables 6 and 7. Owing to the shortness of period A and the large spring–neap and monthly tidal variability, the amplitude of the M_2 semimajor axis is larger (by about 10 cm/s) over most of the water column during period A than B. During both periods the semimajor axis has a maximum in excess of 50 cm/s at 11 mab and then decreases approximately linearly as a function of log (height above bottom) toward the bottom. The basic accuracy of the Geoprobe current sensors is about ±2 cm/s, so that the downward concave curvature of the Geoprobe semimajor axis profile may be real and may reflect weak sediment stratification effects [*Cacchione et al.*, 1995].

Our best estimate of the height of the lower VACM rotor (0.70 mab) places it below the height of the top Geoprobe current sensor (0.81 mab), so that the VACM and Geoprobe profiles should merge in Figure 15 during period A. The uncertainty in the VACM velocity measurements is difficult to estimate since the VACM rotor is known to overspeed in unsteady flow [*Saunders*, 1980], and the precise height of the near-bottom rotor is not known within at least 25 cm (see Appendix B). Since the wave velocities measured with Geoprobe varied from roughly 5 to 15 cm/s and were smaller by a factor of 3 to 5 than the peak flood and ebb currents, the near-bottom rotor experienced nonreversing flows during the stronger currents, and overspeeding should not exceed 5% in the stronger flows [*Beardsley*, 1987]. Thus, a small decrease (say, of order 3%) in the near-bottom VACM semimajor axis to correct for overspeeding and an upward shift of order 25 cm would bring the near-bottom VACM profile into alignment with the Geoprobe profile, resulting in a downward concave amplitude profile over the lowest 2 m above the bottom. The accuracy of the upper VACM measurements is even more difficult to estimate, especially the

Table 7. Semidiurnal Tidal Current Ellipse Parameters at the AMASSEDS Mooring Sites M1-M3

Site	Water Depth, m	Height Above Bottom, m	Semimajor Axis, cm/s	Semiminor Axis, cm/s	Inclination, °L	Phase, °G
			M2			
M1	18	15	149.1 ± 2.9	−1.3 ± 3.7	194.8 ± 1.4	218.1 ± 1.1
		2	126.7 ± 3.4	14.7 ± 1.9	190.2 ± 0.9	199.2 ± 1.5
M2	65	62	41.7 ± 1.4	0.5 ± 1.4	191.7 ± 2.0	215.6 ± 1.9
		33	47.4 ± 1.0	5.0 ± 0.7	189.5 ± 0.9	205.4 ± 1.2
		11	55.7 ± 1.0	5.0 ± 0.6	183.9 ± 0.7	198.6 ± 1.1
		3	47.4 ± 0.9	5.0 ± 0.4	184.7 ± 0.5	188.3 ± 1.1
M3	103	61	35.0 ± 0.7	−6.7 ± 0.9	194.8 ± 1.5	182.4 ± 1.2
		10	20.5 ± 1.4	−2.0 ± 0.8	170.0 ± 2.3	185.2 ± 3.9
			S2			
M1	18	15	31.0 ± 3.7	−3.1 ± 4.7	197.2 ± 3.9	257.8 ± 3.2
		2	20.8 ± 4.3	2.2 ± 2.4	188.0 ± 3.1	233.6 ± 5.4
M2	65	62	8.2 ± 1.7	−0.2 ± 1.8	179.0 ± 5.7	249.4 ± 5.4
		33	9.4 ± 1.2	1.0 ± 0.9	188.5 ± 2.6	240.2 ± 3.3
		11	10.6 ± 1.3	1.3 ± 0.8	184.4 ± 2.0	232.8 ± 3.2
		3	9.4 ± 1.1	1.3 ± 0.5	184.7 ± 1.4	221.8 ± 3.2
M3	103	61	8.1 ± 0.9	−1.8 ± 1.0	197.5 ± 4.0	215.5 ± 3.3
		10	5.2 ± 1.7	−0.8 ± 1.0	178.0 ± 5.6	214.2 ± 9.6
			N2			
M1	18	15	29.0 ± 2.9	−3.1 ± 3.7	190.2 ± 7.5	223.1 ± 5.8
		2	21.8 ± 3.3	3.0 ± 2.0	194.4 ± 5.4	200.2 ± 8.9
M2	65	62	9.4 ± 1.3	0.3 ± 1.4	183.7 ± 8.6	211.8 ± 8.2
		33	8.7 ± 0.9	0.3 ± 0.7	196.2 ± 4.9	196.8 ± 6.1
		11	9.2 ± 1.0	1.4 ± 0.6	183.3 ± 4.1	193.8 ± 6.5
		3	8.9 ± 0.9	1.8 ± 0.4	187.6 ± 2.9	189.3 ± 6.1
M3	103	61	6.0 ± 0.7	0.6 ± 0.9	193.3 ± 8.3	359.3 ± 6.6
		10	3.4 ± 1.4	0.4 ± 0.8	183.0 ± 13.7	355.9 ± 23.7

The inclination or orientation of flood current is given in degrees local measured counterclockwise from 45°N, the average cross-shelf direction along the moored array transect, and phase is given in degrees Greenwich. The locations of the mooring sites and the data measurement periods are listed in Table 4.

54-m instrument, since the effect of rotor overspeeding, which is usually more pronounced at depth under a surface mooring, should be reduced by instrument tilt, which increases with depth. Despite these large uncertainties we conclude that the M_2 semimajor axis profile exhibits a bottom boundary layer structure, with current amplitude increasing approximately linearly with log (height above bottom) to a maximum value roughly near 11 mab and then decreasing with height to the surface.

The M_2 phase decreases smoothly from about 215°G at the surface to about 186°G near the bottom (Figure 15). This means that maximum flood (and ebb) currents occur about 1 hour earlier near the bottom

than at the surface, qualitatively consistent with the dynamical idea of a frictional boundary layer in an oscillatory pressure-driven flow. The M_2 ellipticity or ratio of semiminor axis to semimajor axis varies between -0.1 and $+0.2$ through the water column (with positive ellipticity meaning counterclockwise rotation of the velocity vector with time). The depth-averaged ellipticity is 0.077 (period A) and 0.084 (period B), which is similar in magnitude but opposite in sign to the theoretical value of $(-f/\sigma) = -0.061$ for a plane Poincáre wave. The orientation of the M_2 semimajor axis during flood exhibits some small scatter versus depth about a depth-averaged value of about 187°L (232°N). Since the VACM compass has an uncertainty of $\pm 3 - 5°$, the M_2 flood current exhibits essentially little, if any, veering with depth and is oriented about 7° away from the cross-isobath direction at this site.

The Amazon surface plume was frequently present at the M2 site, causing salinities in the top 5–10 m to drop as low as 30‰ during period A and 15‰ during period B [*Lentz and Limeburner*, this issue]. Beneath the plume in oceanic water at depths greater than about 20 m, the salinity remained quite constant near 36.2‰, and local stratification was controlled by temperature (except very close to the bottom where suspended sediment concentrations got large enough at times to cause significant stratification [*Cacchione et al.*, 1995]. Within the bottom 1–2 m, vertical temperature gradients were relatively weak, with estimates of maximum values of the Brunt–Väisälä frequency $N < 0.017$ rad/s and gradient Richardson number $Ri < 0.05$ during period A when sediment effects are ignored. These low values of N and Ri suggest that the tidal bottom boundary layer may satisfy homogeneous dynamics to lowest order, at least near the bottom.

We next consider a simple vertical model for the local tidal currents driven in a constant depth and density ocean by an imposed plane-wave surface tide. The governing momentum equations are

$$\begin{aligned} \frac{\partial u}{\partial t} - fv &= -\frac{\partial p}{\partial x} + \frac{\partial}{\partial z}\left(A\,\frac{\partial u}{\partial z}\right), \\ \frac{\partial v}{\partial t} + fu &= \qquad + \frac{\partial}{\partial z}\left(A\,\frac{\partial v}{\partial z}\right), \end{aligned} \tag{5}$$

where f is the Coriolis parameter and the pressure gradient $\partial p/\partial x = P_{x0}\cos(\sigma t)$ is oriented in the onshore $(+x)$ direction. The eddy viscosity A has a linear-constant shape given by

$$\begin{aligned} A &= ku_*z \qquad z < \delta_I, \\ A &= ku_*\delta_I \qquad z > \delta_I, \end{aligned} \tag{6}$$

where k is von Karman's constant, u_* is the bottom-friction velocity, and δ_I is the matching height defined as

$$\delta_I = \frac{1}{6}\,\delta = \frac{1}{6}\,\frac{k\bar{u}_*}{\sigma}, \tag{7}$$

where $\bar{u}_*$ is the average friction velocity over a tidal cycle and δ is the boundary layer scale height. *Trowbridge and Madsen* [1984] used this eddy viscosity formulation to model the nonrotating turbulent oscillatory boundary layer beneath gravity waves and found excellent agreement with the laboratory data of *Jonsson and Carlsen* [1976]. This eddy viscosity shape gives a logarithmic velocity profile in a constant stress layer next to the bottom, yet does not increase indefinitely into the interior of the flow. The boundary conditions on velocity are no slip at the bottom and zero stress at the surface, i.e.,

$$\begin{aligned} (u, v) &= 0 \text{ at } z = z_0, \\ \left(A\,\frac{\partial u}{\partial z},\ A\,\frac{\partial v}{\partial z}\right) &= 0 \text{ at } z = h, \end{aligned} \tag{8}$$

where z_0 is the bottom roughness length and h is the water depth. Since the observed M_2 tidal current is nearly rectilinear, we expect turbulent momentum fluxes in the bottom boundary layer to vary significantly over a tidal cycle (as demonstrated by the Geoprobe data of *Cacchione et al.* [1995]), and thus make u_* time dependent following *Trowbridge and Madsen* [1984].

Given P_{x0}, z_0 and the eddy-viscosity profile A, the momentum equations and boundary conditions can be readily solved numerically to give the velocity profile as a function of time. The numerical scheme is straightforward, using backward difference in time and a control volume approach in the vertical [*Patankar*, 1980; *Lentz*, 1995]. A logarithmic grid is used in the vertical, with increasing grid spacing extending from z_0 to h. The velocity is written in complex form $(\vec{u} = u + iv)$ and the resulting equations for $\vec{u}$ at vertical grid points form a tridiagonal matrix which is easily solved by Gaussian elimination.

Since the eddy viscosity A depends on u_* which can change with time and is not known a priori, an iterative approach is taken, whereby an initial value of u_* is used to determine A and $\vec{u}$, which is then used to compute new values of u_*, A, and $\vec{u}$. This process is repeated until the difference in successive values of u_* is < 0.005 cm/s. Since $\vec{u}$ is indeterminant when $u_* = 0$ and it is physically unlikely that the turbulence level adjusts instantaneously to the near-bottom flow, we prescribe a lower bound on u_* by requiring that $u_* \geq 0.1\,u_{*\max}$ at each time step, where $u_{*\max}$ is the maximum value of u_* during the tidal cycle [*Lavelle and Mofjeld*, 1983]. The resulting tidal currents are not strongly dependent on the exact value of this minimum u_*, provided it is small but nonzero.

To apply this model to the observed M_2 velocity data, we ran the model for several tidal cycles until equilibrium was reached and then computed the tidal current ellipse parameters at each level over one tidal cycle. Experiments were conducted varying P_{x0} and z_0 until the model profile of the semimajor axis agreed well with the Geoprobe data over the lowest 1 mab. The semimajor axis and phase profiles do not vary much if the Coriolis parameter f is set to zero, since f/σ is so small.

The model results are shown in Figure 15, superimposed on the Geoprobe and VACM tidal ellipse data. The best qualitative agreement was found for $z_0 = 0.13$ cm, which is consistent with the Geoprobe and dual-rotor VACM results discussed earlier, and $P_{x0} = 0.94 \times 10^{-4}$ m^2/s. Both model semimajor axis and phase lag increase with height to maximum values near the surface. The model u_* is periodic, with a maximum amplitude of 2.8 cm/s which compares well with the value of 2.4 cm/s estimated from Geoprobe. The resulting eddy viscosity is also periodic, with a mean $A = 630$ cm^2/s at $\delta_I = 8.5$ m, and the model boundary layer scale height $\delta = 51$ m, about 80% of the water column. The model predicts small negative ellipticity and little veering in inclination. The subtidal flow in the surface plume is strongly aligned in the along-shelf direction, and the cross-shelf shear in $\partial v/\partial x$ (ignored in (5)) can be comparable with f [*Lentz*, this issue), effectively making the tidal ellipticity in the surface quite variable in time. Below the surface layer the observed ellipticities are small but positive, indicating counterclockwise rotation of the M_2 velocity vector. This suggests that the actual pressure gradient forcing is not simply a plane wave but, instead, must involve at least an incident and reflected plane wave at different orientations.

Even with the large uncertainties in the VACM M_2 ellipse parameters, it is clear that this homogeneous model does not simulate the observed tidal boundary layer structure away from the bottom. The model fit is good within the constant stress layer a few meters above the bottom during peak flow where the eddy viscosity profile is approximately linear. This result can be used to assess if stratification effects are important. In particular, if we take $N = 0.01$ rad/s as a mean value over the lower half of the water column (see Table 8) and assume a logarithmic velocity profile (consistent with Figure 15), then the height z_c above the bottom where the Richardson number becomes equal to one fourth is

$$z_c = u_{*\max}/(2kN) = 3.5 \text{ m} \tag{9}$$

during peak flow. Although N is quite variable (with a standard deviation comparable to its mean value), the small size of z_c relative to δ_I suggests that temperature stratification effects begin to influence the tidal boundary layer dynamics, on average, at depths just above the Geoprobe measurement heights, even at peak flows. Whether a local tidal model which explicitly incorporates stratification and more sophisticated turbulent mixing physics could better predict the observed tidal velocities is not known.

Table 8. Mean and Standard Deviation of the Brunt-Väisälä Frequency Squared N^2 Estimated for Periods A and B at AMASSEDS Mooring Site M2

	Period A		Period B	
Depth, m	Mean, rad^2/s^2	Standard Deviation, rad^2/s^2	Mean, rad^2/s^2	Standard Deviation, rad^2/s^2
2	10.2×10^{-4}	26.6×10^{-4}	45.2×10^{-4}	78.8×10^{-4}
17.5	6.8×10^{-4}	5.1×10^{-4}	24.4×10^{-4}	14.5×10^{-4}
43	3.1×10^{-4}	0.6×10^{-4}	1.2×10^{-4}	1.2×10^{-4}
58	0.7×10^{-4}	0.9×10^{-4}	0.2×10^{-4}	0.6×10^{-4}

The Brunt–Väisälä frequency squared (in radians squared per second squared) is approximated here as $N^2 = -0.001g\ (\partial\sigma_t/\partial z)$, where g is gravity and $\partial\sigma_t/\partial z$ is the vertical gradient of sigma-t. Period A is the 13.8-day period of simultaneous Geoprobe and moored VACM measurements, and period B is the 65-day period when the VACMs returned good data at AMASSEDS mooring site M2. N^2 has been estimated at the middepths between moored in situ temperature and conductivity measurements made at nominal depths of 1, 3, 32, 54, and 62 m. The mean water depth is 65 m. The conductivity record at 62 m exhibited a slow drift and was not used. Instead, the salinity at 62 m was set equal to the salinity at 54 m. This should make little difference in the estimation of stratification since more than 95% of the variance in σ_t and $\partial\sigma_t/\partial z$ measured or estimated with the 54- and 62-m instruments is due to temperature variation. At 32 m, more than 80% of the variance in σ_t is due to temperature. Salinity fluctuations caused more than 85% of the variation in σ_t and $\partial\sigma_t/\partial z$ between the 1- and 3-m instruments.

The observed near-surface decrease in the M_2 semimajor axis at the M2 site suggests the presence of an energetic internal tidal current which is out of phase with the surface barotropic tidal current. The Amazon surface plume was frequently present at the M2 site, causing the mean salinity at the 3-m VACM to drop to about 25‰ during period B. Since the surface plume generally has a thickness of only 5–10 m over the midshelf above the outer delta [*Lentz and Limeburner*, this issue], the density structure in this region which includes the M2 site can be crudely characterized as a two-layer fluid. Following *Rattray* [1960], we consider the onshore propagation of a long surface gravity wave in a nonrotating, two-layer fluid over a step decrease in the depth of the lower layer, where here the mean thickness of the upper layer is constant across the depth change and the abrupt change in bottom depth is meant to model the seaward end of the subaqueous delta where the total water depth decreases from about 70 to 30 m over a horizontal distance of about 20 km. For depth and density parameters appropriate for the mid-Amazon shelf (see Appendix C), the model predicts that an internal tide (with an interfacial amplitude of about 1.8 times the surface tide) will propagate in both directions away from the depth change. This internal tide will lead to either upper or lower layer intensification of the total tidal current, depending on distance from the depth change scaled by the internal-tide wavelength. About one half an internal-tide wavelength (20 km) seaward of the depth change, the internal tide will be out of phase with the surface tide and cause the lower layer tidal velocity to be a maximum, while one half an internal-tide wavelength (18 km) shoreward of the depth change, the internal and surface tides will be out of phase and cause surface layer intensification. While this model is much too simple, it does suggest that the semidiurnal barotropic tidal flow over the outer edge of the subaqueous delta can generate an energetic internal tide (in the presence of the Amazon surface plume), and that whether the resulting net tidal current is either interior intensified (as observed at the M2 site) or surface intensified (as observed at the M1 site) depends on the distance of the site from the region of rapid bottom depth change. We should note, however, that while the energy in the internal tide may reach 5% that of the surface tide near the generation region, the flux of energy out of the surface tide into the internal tide is much weaker, so that the dynamics of the surface barotropic tide (described in earlier sections) should be unchanged to lowest order.

6. M_2 Energy Flux Over the Amazon Shelf

We consider next the net energy flux over the Amazon shelf and into the Amazon and Para Rivers due to the M_2 tide. We first use ADCP transport measurements and coastal sea level data to estimate the M_2 energy flux into the Amazon River mouth, then use similar measurements to estimate the M_2 energy flux and dissipation in the Para River. These estimates are then combined with estimates of the M_2 energy flux derived from the variable-width channel model to describe the pattern of energy flux over the Amazon shelf.

6.1. M_2 Energy Flux Into Amazon River Mouth

During the November 1991 AMASSEDS cruise, ADCP measurements were obtained in the Amazon River mouth during transits of the R/V *Iselin* in and out of Belem to the AMASSEDS working area. The ADCP data included a 25-hour anchor station on November 16, 1991, at RM1 (Figure 2) as well as two complete transects covering the outer river mouth. The total ADCP data set includes 127 hourly and vertically averaged velocity estimates (Figure 16) spread over a period of about 50 days (October 11–December 1). The observed currents in the area have maximum speeds in excess of 1 m/s and are mainly polarized normal to the local topography.

Using the empirical technique described by *Candela et al.* [1992], we obtain the M_2 tidal current ellipse pattern shown in Figure 17. The M_2 semimajor axis increases onshore and toward the entrance of the Para River from 0.5 to 0.75 m/s. The contours of constant phase propagate inward normal to the local bathymetry, indicating a phase speed of about 25 km/h or 7 m/s for the M_2 wave in the area. The semiminor axis is generally small, indicating that the M_2 ellipse is nearly rectilinear with a tendency to rotate counterclockwise to the north and clockwise to the south in the river mouth. The geographical orientation of the semimajor axis shows a tidal current conforming with the convergent shape of the river mouth region.

The deduced steady flow pattern (Figure 16) is weak but consistent with the magnitude of the river discharge reported for this time of year (about 0.1 Sv). To Figure 16 is added the steady current field obtained from a similar analysis on ADCP data obtained in the Para River (to be described later), which matches reasonably well with the steady field obtained from the Amazon River mouth ADCP observations. The residual currents (Figure 16) are large and represent the unexplained 19% of the current variability. They consist of unresolved tidal variability, measurement noise, and other incoherent flow structures related to eddy activity with scales small in relation to the dimensions of the area covered by the observations.

The rate of change of mechanical energy of a fluid element is given by *Godin* [1988] as

$$\frac{D}{Dt}\left[\frac{1}{2}\rho \mid \mathbf{v} \mid^2 + \rho g z\right] = -\nabla \cdot p\mathbf{v} + \rho\,(T+F) \cdot \mathbf{v} \quad , \quad (10)$$

where ρ is water density, $\mathbf{v}$ is the current velocity vector, p is pressure, T is the tidal force, and F represents friction. This equation simply states that the rate of change of potential and kinetic energy within a fluid element is equal to the energy flux divergence plus the power added (or extracted) by the tidal and friction forces. Integrating over the volume and considering the

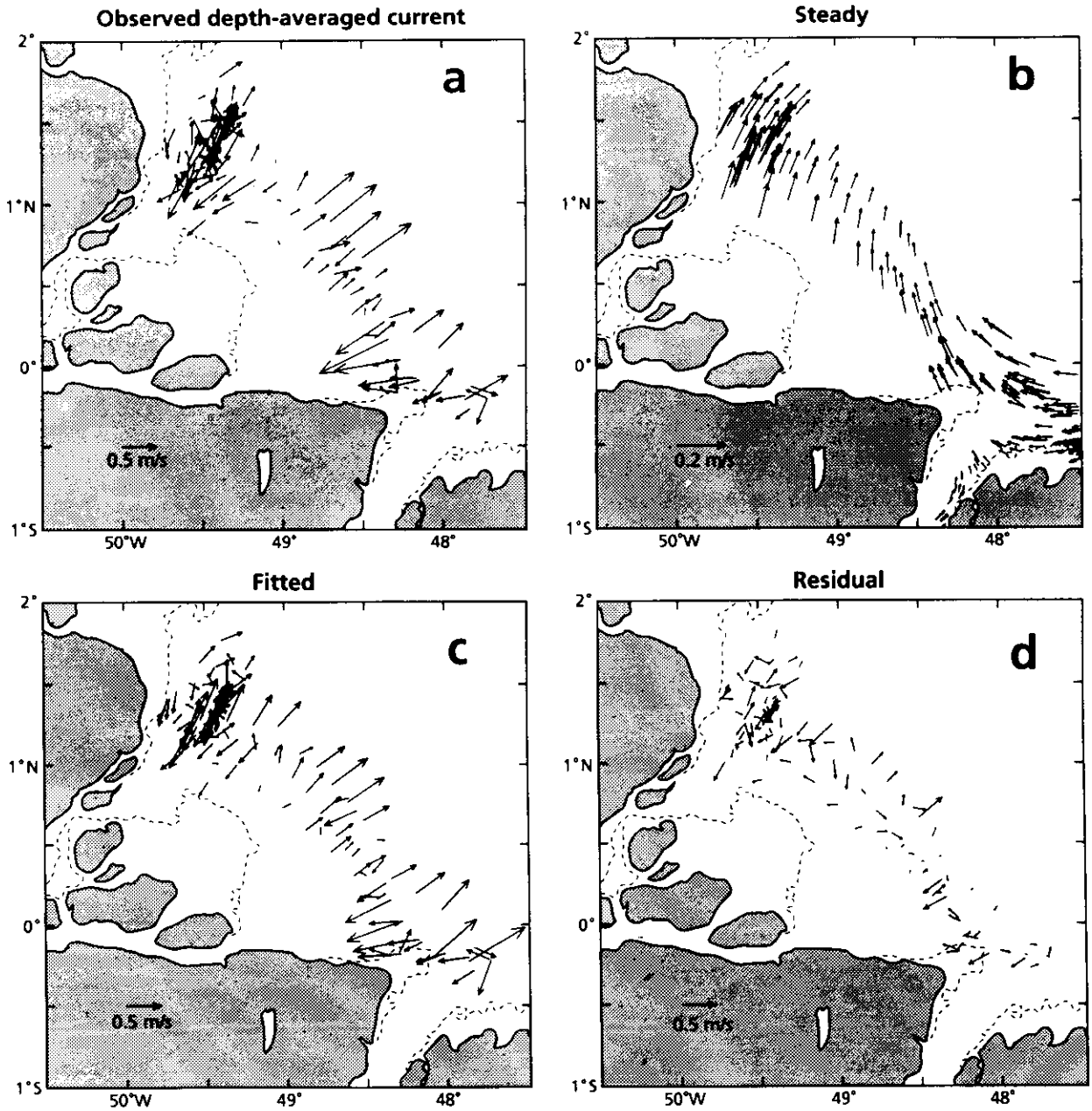

Figure 16. ADCP vertically averaged current measurements obtained in the Amazon River mouth during the November 1991 AMASSEDS cruise. The vectors shown represent hourly averaged currents (a) which have been decomposed into a steady fitted component (b), a semidiurnal tidal fitted component (c), and a residual field (d). The steady flow field includes results from ADCP measurements made off the Para River. Note the difference in current scale between the steady and other components. The fitting is based on first-degree polynomial expansions of the east and north current components for the M_2 and S_2 constituents and the steady component. The fitted fields account for about 80% of the variance in the measurements. The distribution of ADCP data is shown in Figure 17. The 5-m isobath is shown for reference.

divergence theorem and the pressure to be hydrostatic, we find that the integral of the vector $p\mathbf{v} = \rho\, g z\, \mathbf{v}$ over the surface of the volume gives the change of mechanical energy inside the volume.

We want to estimate the net energy flux into the Amazon River mouth due to the M_2 tide. Therefore we need to integrate the energy flux vector per unit area $\mathbf{P}$ given by

$$\mathbf{P} = \rho\, g\, \zeta\, \mathbf{v}, \tag{11}$$

along a contour closing the mouth region and average over a tidal cycle. For a tidal constituent like M_2, $\zeta = \zeta_0 \cos \sigma t$ and $\mathbf{v} = [\mathbf{M} \cos(\sigma \mathbf{t} - \phi), \mathbf{m} \sin(\sigma \mathbf{t} - \phi)]$,

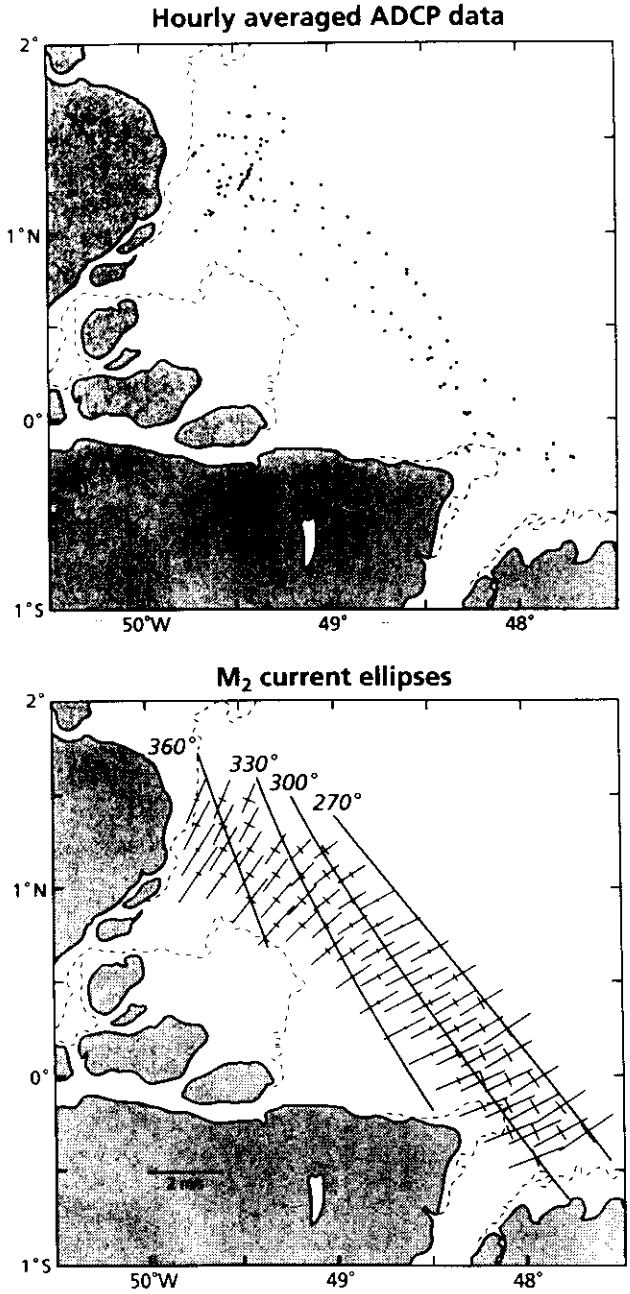

Figure 17. M_2 current cotidal chart for the Amazon River mouth based on 127 hourly averaged and depth-averaged ADCP current measurements made during the November 1991 AMASSEDS cruise. (top) The distribution of the ADCP data and (bottom) the fitted current ellipses, with the phase of maximum flood (onshore) flow given in degrees Greenwich with a contour interval of 30°.

taking phase measurements with respect to high water and a coordinate system referenced to the semimajor axis of the current ellipse. In these expressions, σ is the tidal frequency, M is the semimajor axis, m is the semiminor axis, ζ_0 is the elevation amplitude, and ϕ is the phase difference between high water and maximum current velocity. After averaging over a tidal cycle, the net energy flux vector per unit area is given by $\mathbf{P}_n = 1/2\ \rho g\ \zeta_0\ [M\ \cos\ \phi,\ -m\ \sin\ \phi]$.

Figure 18 shows a map of the Amazon River mouth where we have selected five points (denoted by open circles) within the ADCP survey area where we estimate $\mathbf{P}_n$. At these points the values for $\mathbf{v}$ are obtained from Figure 17, and elevation amplitude and phase are estimated using the following approach. From coastal sea level stations (also shown as open circles) at both ends of the arc we first interpolate the M_2 elevation amplitude and phase at the five positions marked by the solid

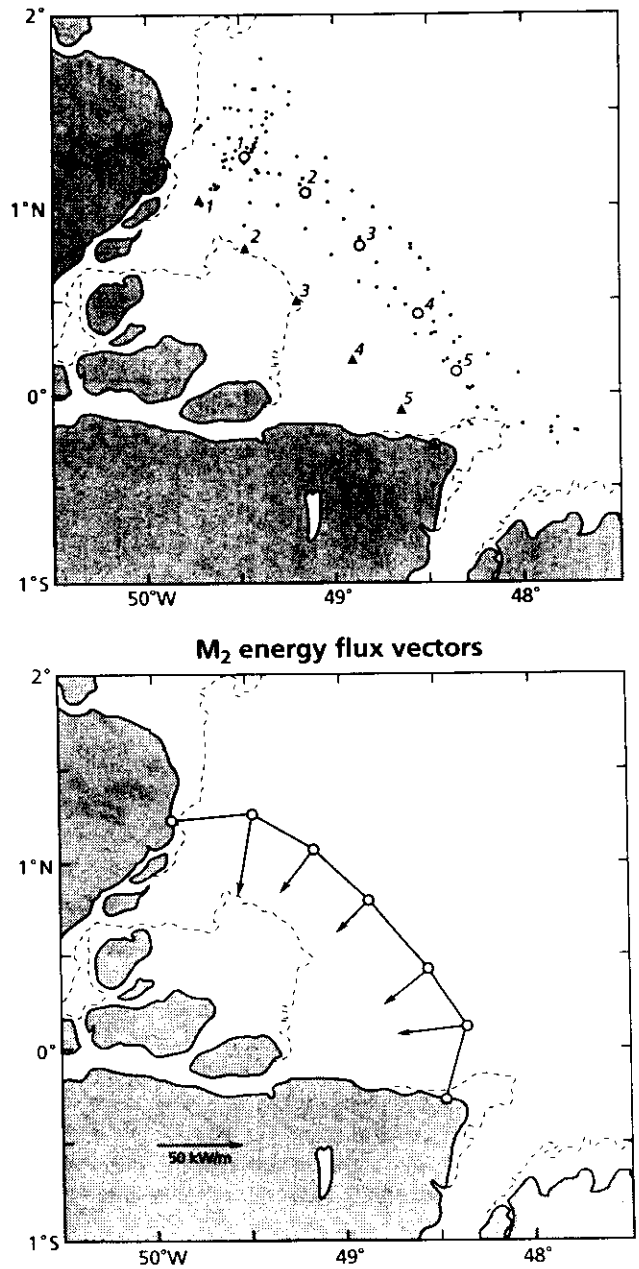

Figure 18. M_2 net tidal energy flux into the Amazon River. (top) Locations of points where M_2 currents (open circles) and elevations (triangles) were estimated from ADCP and coastal sea level data, respectively. The elevation estimates were then shifted to the current points using the approach described in section 6, and (bottom) the net energy flux vectors normal to the arc computed. The total net energy flux integrated along the arc is 4.7×10^9 W.

triangles. On the basis of Figure 6, we then estimate that between the numbered triangles and circles there is no difference in elevation amplitude, but there is a constant difference in phase of 20°, with maximum elevation occurring about 40 minutes earlier at the circles. The resulting net energy flux vectors normal to the arc are shown in Figure 18 (bottom). The energy flux is largest in front of the North and South Channels and smaller in between where the water depth shallows onto Banco Santa Rosa, and no prominent entrance to the river mouth is found. Integrating along the arc yields a total net M_2 energy flux of 4.7×10^9W entering the Amazon River mouth. The principal uncertainty in this result is due to the uncertainty in the elevation phase estimates at the circle points; an increase in the phase difference from 20 to 30° leads to a 20% decrease in the total net energy flux.

6.2. M_2 Energy Flux in the Para River

The equation for the rate of change of mechanical energy given above (see (11)) indicates that within a channel the divergence of the net energy flux should be balanced by friction and by the rate of work done by the tidal force. In a shallow channel the rate of work done by the tidal force is at least 2 orders of magnitude smaller than that due to friction, so that it can be safely neglected in what follows.

Using ADCP data collected during the November 1991 AMASSEDS cruise, we have selected those ADCP current measurements in the entrance of the Para River that reach up to Belem, resulting in 108 hourly and vertically averaged current measurements (Figure 19). Based on an analysis similar to that given above, we show in Figure 19 the M_2 tidal ellipse characteristics in this area. The amplitude of the M_2 semimajor axis current increases upstream from values of 0.6 m/s at the entrance to 1 m/s near Belem. The phase contours indicate that the tidal current takes about 3 hours to get from the river entrance to Belem. The semiminor axis shows a basically rectilinear current within the river, and the orientation of the semimajor axis is aligned with the local channel configuration.

Figure 20 shows four stations (denoted by triangles) where sea level data are available. To estimate the energy flux through cross-channel sections at these locations, we combine the M_2 elevation amplitude and phase values from these four sea level stations with current estimates (obtained from Figure 19) at the nearby points marked with open circles in Figure 20 (top). Figure 20 (bottom) shows a plot of the net energy flux estimates as a function of along-channel distance. While there is considerable scatter in the flux estimates, the general slope of about 3.8×10^3W/m is consistent with dissipation due to quadratic bottom friction with $C_d = 0.003$. It is important to emphasize here that the data used in these calculations were not taken to estimate tidal energy fluxes; instead, this region was sporadically sampled in time, sea level and currents were not measured simultaneously, and the ADCP currents used are very rough approximations of the cross-channel average. Ideally, elevation and currents should be sampled simultaneously since dissipation is expected to vary both with

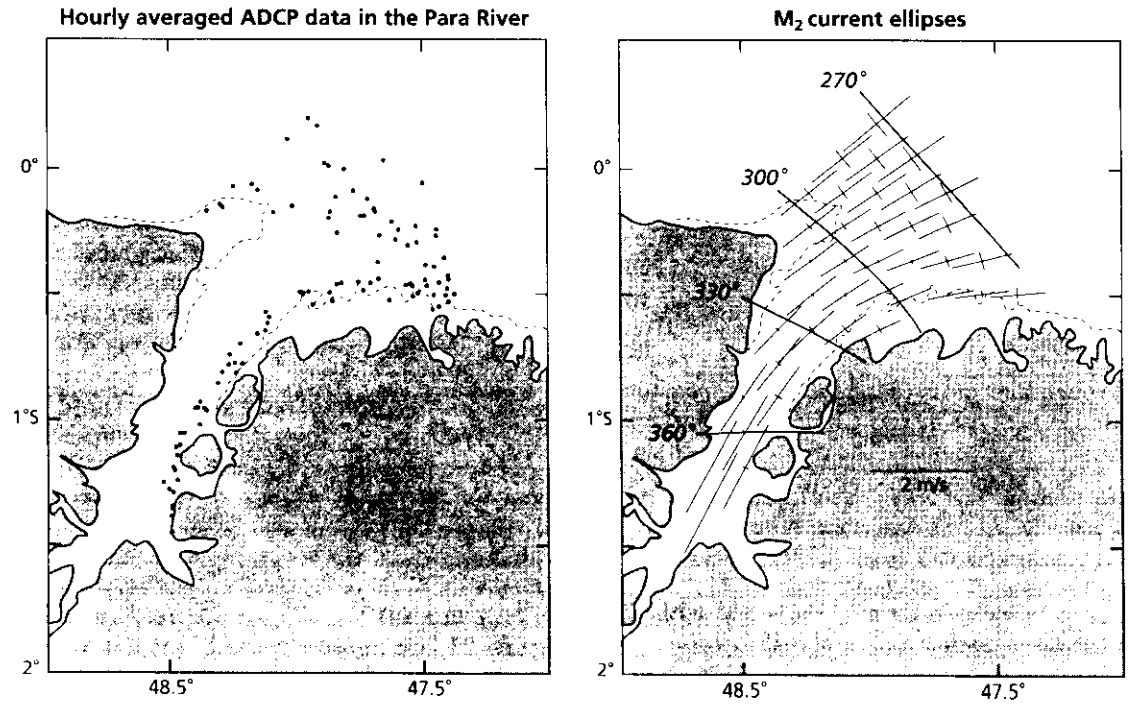

Figure 19. M_2 current cotidal chart for the Para River entrance based on 108 hourly and depth-averaged ADCP current measurements made during the November 1991 AMASSEDS cruise. (left) The distribution of the ADCP data and (right) the fitted current ellipses with the phase of maximum flood (onshore) flow given in degrees Greenwich with a contour interval of 30°.

of the Amazon River during peak discharge, III, Currents, *Cont. Shelf Res.*, *6*, 73–86, 1986.

Defant, A., *Physical Oceanography*, *2*, 598 pp., Pergamon, New York, 1961.

EG&G Consultants, Current and hydrographic measurements of the North Brazil Coastal Current between 2° and 7°N latitude, Waltham, Mass., 1981.

Ferraz, L. A'dCarvalho, Tidal and current prediction for the Amazon's North Channel using a hydrodynamical-numerical model, M.S. thesis, 85 pp., Naval Postgraduate School, Monterey, Calif., 1975.

Flather, R. A., and N. S. Heaps, Tidal computations for Morecambe Bay, *Geophys. J. Roy. Astron. Soc.*, *42*, 489–517, 1975.

Forman, M. G., Manual for tidal heights analysis and prediction, *Pac. Mar. Sci. Rep. 77-10*, 97 pp., Inst. of Ocean Sci., Victoria, B.C., 1977.

Forman, M. G., Manual for tidal currents analysis and prediction, *Pac. Mar. Sci. Rep. 78-6*, 97 pp., Inst. of Ocean Sci., Victoria, B.C., 1978.

Garrett, C., Tidal resonance in the Bay of Fundy and the Gulf of Maine, *Nature*, *238*, 441–443, 1972.

Geyer, W. R., and G. C. Kineke, Observations of currents and water properties in the Amazon frontal zone, *J. Geophys. Res.*, this issue.

Geyer, W. R., R. C. Beardsley, J. Candela, B. M. Castro, R. V. Legeckis, S. J. Lentz, R. Limeburner, L. B. Miranda, and J. D. Trowbridge, The physical oceanography of the Amazon outflow, *Oceanography*, *4*, 8–14, 1991.

Gibbs, R. J., Currents on the shelf of northeastern South America, *Estuarine Coastal Shelf Sci.*, *14*, 283–299, 1982.

Giese, B. S., and D. A. Jay, Modelling tidal energetics of the Columbia River Estuary, *Estuarine Coastal Shelf Sci.*, *29*, 549–571, 1989.

Godin, G., *Tides*, 290 pp., Centro de Investigación Científica y Educación Superior de Ensenada, Ensenada, Mexico, 1988.

Godin, G., On tidal resonance, *Cont. Shelf Res.*, *13*, 89–107, 1992.

Greenberg, D. A., Modelling the mean barotropic circulation in the Bay of Fundy and Gulf of Maine, *J. Phys. Oceanogr.*, *13*, 886–904, 1983.

Greenberg, D. A., A numerical model investigation of tidal phenomena in the Bay of Fundy and the Gulf of Maine, *Mar. Geod.*, *2*, 161–187, 1979.

Heath, R. A., Tidal energy loss in coastal embayments, *Estuarine Coastal Shelf Sci.*, *12*, 279–290, 1981.

Jonsson, I. G., and N. A. Carlsen, Experimental and theoretical investigations in an oscillatory turbulent boundary layer, *J. Hydraul. Res.*, *14*(1), 45–60, 1976.

Kineke, G. C., Fluid muds on the Amazon continental shelf, Ph.D. thesis, 259 pp., Univ. of Wash., Seattle, 1993.

Kineke, G. C., and R. W. Sternberg, Distribution of fluid muds on the Amazon continental shelf, *Mar. Geol.*, in press, 1995.

Knight, D. W., Some field measurements concerned with the behavior of resistant coefficients in a tidal channel, *Estuarine Coastal Shelf Sci.*, *12*, 303–322, 1981.

Lavelle, J. W., and H. O. Mofjeld, Effects of time-varying viscosity on oscillatory turbulent channel flow, *J. Geophys. Res.*, *88*, 7607–7616, 1983.

Lentz, S. J., Sensitivity of the inner-shelf circulation to the form of the eddy-viscosity profile, *J. Phys. Oceanogr.*, in press, 1995.

Lentz, S. J., The Amazon River plume during AMASSEDS: Subtidal current variability and the importance of wind forcing, *J. Geophys. Res.*, this issue.

Lentz, S. J., and R. Limeburner, The Amazon River Plume during AMASSEDS: Spatial characteristics and salinity variability, *J. Geophys. Res.*, this issue.

McCullough, J., Vector-Averaging Current Meter speed calibration and recording technique, *Tech. Rep. WHOI-75-44*, 35 pp., Woods Hole Oceanogr. Inst., Woods Hole, Mass., 1975.

Muller-Karger, F. E., C. R. McClain, and P. L. Richardson, The dispersal of the Amazon's water, *Nature*, *333*, 56–69, 1988.

National Oceanic & Atmospheric Administration (NOAA), *Tide Tables* 1974: *East Coast of North and South America*, 288 pp., National Ocean Survey, Washington, D.C., 1973.

Nittrouer, C. A., M. T. Sharara, and D. J. DeMaster, Variations of sediment texture on the Amazon continental shelf, *J. Sediment. Petrol.*, *53*, 179–191, 1983.

Nittrouer, C. A., T. B. Curtin, and D. J. DeMaster, Concentration and flux of suspended sediment on the Amazon continental shelf, *Cont. Shelf Res.*, *6*, 151–174, 1986.

Nittrouer, C. A., D. J. DeMaster, A. G. Figueiredo, and J. M. Rine, AMASSEDS: An interdisciplinary investigation of a complex coastal environment, *Oceanography*, *4*, 3–7, 1991.

Oltman, R. E., Reconnaissance investigations of the discharge and water quality of the Amazon River, *U.S. Geol. Surv., Circ. 552*, 16 pp., 1968.

Patankar, S. V., *Numerical Heat Transfer and Fluid Flow*, 197 pp., Hemisphere, McGraw-Hill, New York, 1980.

Platzman, G. W., Normal modes of the world ocean, IV, Synthesis of diurnal and semidiurnal tides, *J. Phys. Oceanogr.*, *14*, 1532–1550, 1984.

Platzman, G. W., G. A. Curtis, K. S. Hansen, and R. D Slater, Normal modes of the world ocean, II, Description of modes in the period range 8 to 80 hours, *J. Phys. Oceanogr.*, *11*, 570–603, 1981.

Rao, D. B., Natural oscillations of the Bay of Fundy, *J. Fish. Res. Board Can.*, *25*, 1097–1114, 1968.

Rattray, M., On the coastal generation of internal tides, *Tellus*, *12*, 54–62, 1960.

Saunders, P. M., Overspeeding of a Savonius rotor, *Deep Sea Res., Part A*, *27*, 755–759, 1980.

Schwiderski, E. W., Global ocean tides, II, The semi-

diurnal principal lunar tide (M_2), atlas of tidal charts and maps, *NSWC Tech. Rep. 79-414*, 87 pp., Nav. Surface Weapons Cent., Dahlgren, Va, 1979.

Schwiderski, E. W., Global ocean tides, III, The semidiurnal principal solar tide (S_2), atlas of tidal charts and maps, *NSWC Tech. Rep. 31-122*, 96 pp., Nav. Surface Weapons Cent., Dahlgren, Va.,1981.

Soulsby, R. L., and K. R. Dyer, The form of the nearbed velocity profile in a tidally accelerating flow. J. Geophys. Res., 86, 8067–8074, 1981.

Stephens, J. A., R. J. Uncles, M. L. Barton, and F. Fitzpatrick, Bulk properties of intertidal sediments in a muddy, macrotidal estuary, *Mar. Geol., 103*, 445–460, 1992.

Sternberg, R. W., G. C. Kineke, and R. Johnson, An instrument system for profiling suspended sediment, fluid and flow conditions in shallow marine environments, *Cont. Shelf Res., 11*, 109–122, 1991.

Trowbridge, J. H., and G. C. Kineke, Structure and dynamics of fluid muds over the Amazon continental shelf, *J. Geophys. Res., 99*, 865–874, 1994

Trowbridge, J. H., and O. S. Madsen, Turbulent-wave boundary layers, 1, Model formulation and first-order solution, *J. Geophys. Res., 89*, 7989–7998, 1984.

Uncles, R. J., and J. A. Stephens, Computed and observed currents, elevations and salinity in a branching estuary, *Estuaries, 13*, 133–144, 1990.

R. C. Beardsley, J. Candela, W. R. Geyer, S. J. Lentz, and R. Limeburner, Department of Physical Oceanography, Woods Hole Oceanographic Institution, Woods Hole, MA 02543

D. Cacchione, U.S. Geological Survey, Menlo Park, CA 94025

N. Carneiro, Directoria de Hidrografia e Navegacao, 24400-000, Niteroi, Brazil

B. M. Castro, Instituto Oceanográfica, Universidade de São Paulo, 05508-900, São Paulo, Brazil

(Received September 23, 1993; revised March 10, 1994; accepted April 28, 1994.)

Pergamon

Continental Shelf Research, Vol. 16, No. 5/6, pp. 575–616, 1996

0278–4343/96 $15.00 + 0.00

0278–4343(95)00051–8

Physical oceanography of the Amazon shelf

W. ROCKWELL GEYER,* ROBERT C. BEARDSLEY,* STEVEN J. LENTZ,* JULIO CANDELA,* RICHARD LIMEBURNER,* WILLIAM E. JOHNS,† BELMIRO M. CASTRO‡ and IVAN DIAS SOARES§

(*Received* 27 *July* 1994; *accepted* 2 *June* 1995)

Abstract—The Amazon shelf is subject to energetic forcing from a number of different sources, including near-resonant semi-diurnal tides, large buoyancy flux from the Amazon River discharge, wind stress from the northeasterly tradewinds and strong along-shelf flow associated with the North Brazil Current. Although the large volume of river discharge produces a pronounced salinity anomaly, the water motions on the shelf are dominated by the other forcing factors. Tidal velocities of up to 200 cm s^{-1} are generally oriented in the cross-shelf direction. Tide-induced mixing influences the position and structure of the bottom salinity front that separates the well-mixed nearshore region from the stratified plume. High concentrations of suspended sediment trapped along the frontal zone increase the stability of the tidal boundary layer and thus reduce the bottom stress. At subtidal frequencies, motion is primarily along-shelf toward the northwest, both in the plume and in the ambient, high-salinity water of the outer-shelf. The plume is generally 5–10 m thick, with a salinity of 20–30 psu. The along-shelf velocity within the plume varies as a function of the along-shelf wind stress. This variability results in large temporal variations in plume structure and freshwater content on the shelf. The net northwestward motion of the Amazon plume and of the ambient shelf water appears to be the result of a large-scale pressure gradient associated with the North Brazil Current system.

INTRODUCTION

A Multidisciplinary Amazon Shelf SEDiment Study (AmasSeds) addresses the interaction between physical oceanographic processes, sediment transport, biogeochemical transformations and sedimentation in the world's largest riverine dispersal system (Nittrouer *et al.*, 1991; AmasSeds Group, 1990). Previous investigations have found a complex depositional pattern of sediment and chemical species (Nittrouer and DeMaster, 1986) indicating intense physical disturbance of the seabed and large temporal and spatial variability of the sediment transport and deposition on the shelf. These early investigations did not resolve the variability of the physical regime in sufficient detail to determine the scales of variation or the mechanisms forcing these variations (Curtin and Legeckis, 1986; Curtin, 1986a,b). AmasSeds was designed to provide adequate temporal and spatial

*Woods Hole Oceanographic Institution, Woods Hole, MA 02543, U.S.A.
†Rosenstiel School of Marine and Atmospheric Science, University of Miami, Miami, FL 33124, U.S.A.
‡Universidade de São Paulo, Instituto Oceanografico, São Paulo, SP, Brazil.
§Departamento Fisica, Fundaçao Universidade do Rio Grande, Rio Grande, Brazil.

coverage to identify the important scales of physical variability and to discern the dominant transport mechanisms of physical transport and the impact of these processes on the sediments, chemical compounds and biological communities present on the Amazon shelf.

This paper provides a synthesis of the results from the physical oceanographic component of AmasSeds. It describes how the various physical processes occurring on the Amazon shelf interact with each other and influence the distribution and transport of suspended material on the Amazon shelf.

BACKGROUND

The physical setting

The Amazon River watershed extends across the vast Amazon rain forest to the crest of the Andes (Fig. 1) with an area of approximately 7×10^6 km^2 (Nittrouer and DeMaster, 1986) making it the largest drainage basin in the world. The riverine discharge to the ocean averages 180,000 m^3 s^{-1} (Oltman, 1968) accounting for 16% of the global freshwater

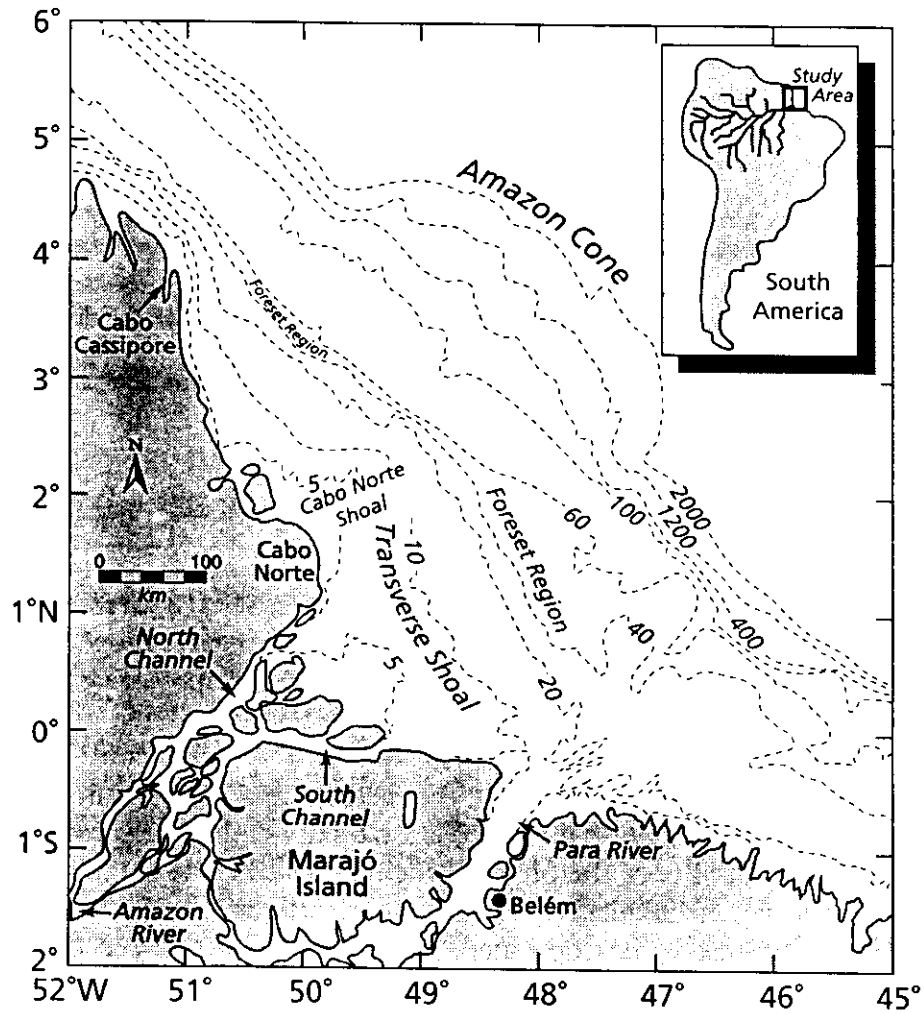

Fig. 1. Bathymetric map of the Amazon shelf, with some of the important physical features indicated. The inset shows the extensive drainage area of the Amazon River and its tributaries.

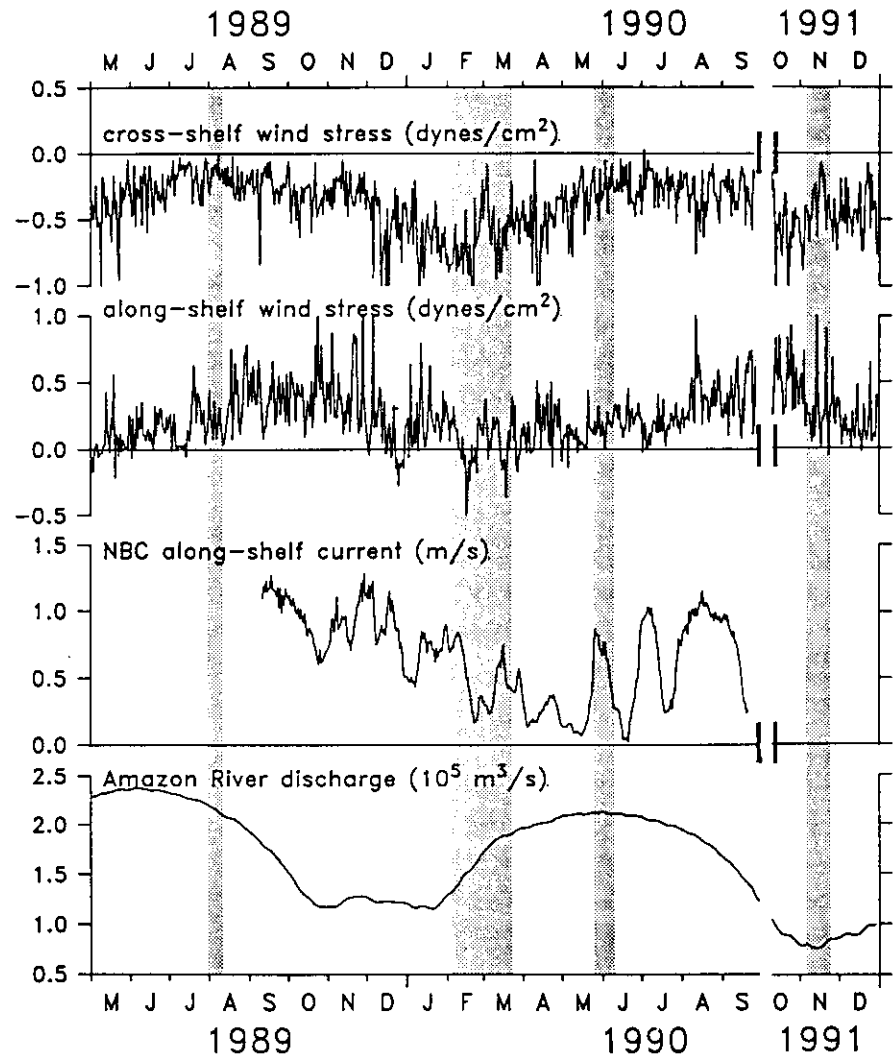

Fig. 2. Time series of the important variables influencing the Amazon shelf during AmasSeds. Amazon River discharge is obtained at Obidos (Nittrouer and DeMaster, 1996), representing approximately 90% of what arrives at the mouth. Current observations were obtained within the North Brazil Current at 60-m depth, close to the 500-m isobath (see Fig. 3). Along-shelf (toward 315°) and across-shelf (toward 45°) winds are from the European Centre for Medium Range Weather Forecasting (ECMWF). The dates of the cruises are indicated by shading.

run-off (Baumgartner and Reichel, 1975). Peak discharge, averaging 220,000 m^3 s^{-1}, typically occurs in May (Fig. 2) and minimum discharge, averaging 100,000 m^3 s^{-1}, typically occurs in November (Richey *et al.*, 1986).

The Amazon enters the Atlantic at the equator through two channels, the North and South Channels. These channels debouch into a broad, shallow, inner shelf, with water depths of less than 15 m extending seaward 100–200 km from the river-mouth channels. A bar extends across the river-mouth region, approximately 100 km from the mouth (the transverse shoal indicated on Fig. 1) with minimum depths of approximately 9.5 m. A near-bottom salinity front is usually located near the river-mouth bar, separating well-mixed, nearly fresh water on the landward side, from strongly stratified water with high near-bottom salinities on the seaward side (Gibbs, 1970; Nittrouer *et al.*, 1986; Geyer *et al.*, 1991).

To the south, the Amazon shelf is bounded by the Para River (Fig. 1), a wide estuary that has a modest freshwater input relative to the Amazon. To the north of the river mouth, the shallow Cabo Norte shoal partially obstructs the Amazon outflow from flowing directly alongshore into the inner shelf region to the northwest. The broad inner-shelf region extends along the coast for 200 km northwest of the shoal, eventually narrowing at Cabo Cassiporé. The nearly flat inner shelf (slope $<10^{-4}$) is the landward portion of the Amazon delta (referred to geomorphologically as the topset beds). It joins the more steeply sloping foreset beds (slope $>10^{-3}$) between the 30- and 60-m isobaths, where the highest sediment accumulation rates occur (Kuehl *et al.*, 1986). The shelf break is located along the 100-m isobath. Seaward of the shelf break is the Amazon cone, a pronounced depositional feature created during a period of low sea level (Damuth and Kumar, 1975).

Forcing variables

The large freshwater discharge is only one of several important factors that influence the oceanography of the Amazon shelf. The North Brazil Current (NBC) is a strong western boundary current, which originates in the South Equatorial Current and flows across the equator and along the continental margin, past the mouth of the Amazon. At 4°N, the NBC has a large seasonal variation, ranging from a maximum transport of 35 Sv (1 Sv = 10^6 m^3 s^{-1}) in July–August, to a minimum of 10 Sv in April–May, with an annual mean of approximately 25 Sv (Johns, personal communication, 1995). The transport is dominated by flow in the upper 150 m and measurements by Candela *et al.* (1992) suggest that the NBC transport over the shelf may be as much as 3–5 Sv (Fig. 2). The NBC exhibits large mesoscale transport fluctuations, with periods of 25–40 days and 60–90 days. The higher frequency fluctuations are strongly surface-trapped and more energetic in July–August, while the lower frequency fluctuations are present year-round and are associated with the propagation of large anticyclonic eddies northwestward along the margin (Johns *et al.*, 1990; Johns, personal communication, 1995).

Atmospheric forcing over the Amazon shelf is dominated by the tradewinds. Figure 2 shows the annual variation of wind stress, with maximum stresses corresponding to the northeast trade winds in December–April. While the winds are oriented approximately perpendicular to the coast, Lentz (1995a) shows that fluctuations in both the along- and cross-shelf components of the wind stress strongly influence the flow of Amazon River water over the shelf. The tradewinds also generate moderate surface gravity waves that propagate onto the Amazon shelf. Maximum wave energy occurs during the maximum wind stress in December–April.

The strongest currents over the shelf are due to the semi-diurnal tides. The wide shelf amplifies the tidal wave, with near-resonant conditions north of the river mouth that lead to tidal ranges of up to 6 m near Cabo Norte. Tidal currents are generally oriented cross-shelf, with current speeds reaching 200 cm s^{-1} in the frontal zone (Gibbs, 1982; Nittrouer *et al.*, 1986; Beardsley *et al.*, 1995). The semi-diurnal tide exhibits a strong spring-neap and monthly modulation, which contributes to the subtidal variation of stratification and possibly the along-shelf flow.

Another important factor influencing the physical regime is suspended sediment discharge from the Amazon. High concentrations of suspended sediment, termed "fluid muds" (with concentration >10 g l^{-1}), accumulate along the near-bottom salinity front (Kineke *et al.*, 1996; Kineke and Sternberg, 1995). The suspended load is so great that the

density anomaly due to the sediment exceeds that due to salinity variations in the near-bottom water, thus influencing near-bottom stratification. The stratification by fluid mud reduces the bottom stress in the inner shelf, inhibiting vertical mixing and reducing tide-induced bottom stress and dissipation (Trowbridge and Kineke, 1994).

OBSERVATIONAL PROGRAM

AmasSeds involved a variety of physical oceanographic observations. Four shelf-wide hydrographic surveys were performed between August 1989 and November 1991, during different parts of the river discharge cycle (falling, rising, high and low) (Fig. 2)—note that the cruises were not all performed within the same annual cycle. On each survey, conductivity, temperature and light transmission were measured using a Neil Brown Mk III conductivity–temperature–depth (CTD) recorder and a Seatech transmissometer (5-cm pathlength). Shipboard measurements of velocity were obtained with an RDI acoustic Doppler current profiler (ADCP). The ADCP was equipped with either a 150 kHz or 600 kHz transducer. The 600 kHz unit was used at anchor stations for higher vertical resolution. However, the 600 kHz unit did not reliably provide ship speed over the soft sediments of the inner shelf, therefore, the 150 kHz unit was used for underway measurements. The hydrographic surveys involved a number of other water-column measurements by other disciplines (see AmasSeds papers), including detailed measurements of suspended-sediment distribution (see also Kineke and Sternberg, 1995).

Smaller-scale surveys and anchor-station measurements were made during three cruises, to resolve the variations in currents and water properties within the frontal zone, the region of strong near-bottom salinity gradients where much of the mixing between fresh and salt water appeared to occur. Anchor stations were performed usually for 25 h, to resolve the diurnal and semi-diurnal variations in currents and water properties, and to allow estimation of the non-tidal residual currents and salinity structure. The anchor-station measurements were concentrated along two transects, referred to as the River-Mouth Transect and the Open-Shelf Transect (Fig. 3). Velocity data were obtained during the anchor stations with both the 600 kHz ADCP and electromagnetic current meters lowered on an instrumented tripod (Geyer and Kineke, 1995; Kineke and Sternberg, 1995). Because the frontal zone is the region of maximum fluid-mud concentration, a major component of the frontal-zone measurements was directed at quantifying the fluid-mud distribution and determining its influence on flow and other water properties.

A moored array of current meters, with temperature and conductivity sensors, was deployed across the shelf about 150 km northwest of Cabo Norte, between February and June 1990 (Fig. 3). The M1 mooring site was at the 18-m isobath, close to the seaward limit of the bottom salinity front. The M2 mooring site was located at the 65-m isobath, at the base of the foreset beds where the most rapid sediment accumulation occurs. These moorings were equipped with Vector-Averaging Current Meters (VACMs) and Seabird temperature and conductivity sensors at all instrument depths (see inset, Fig. 3). A Vector-Averaging Wind Recorder was deployed on a surface toroid buoy at the 65-m site. A special dual-rotor VACM was deployed near the bottom at the 65-m site, in an attempt to measure the near-bed shear. The M3 mooring site, instrumented with an Interocean S4 current meter and three SensorData current meters, was located at the 105-m isobath to provide information concerning the outer-shelf forcing. Additional current measurements were obtained at the 65-m M2 site, using a bottom tripod equipped with a vertical array of

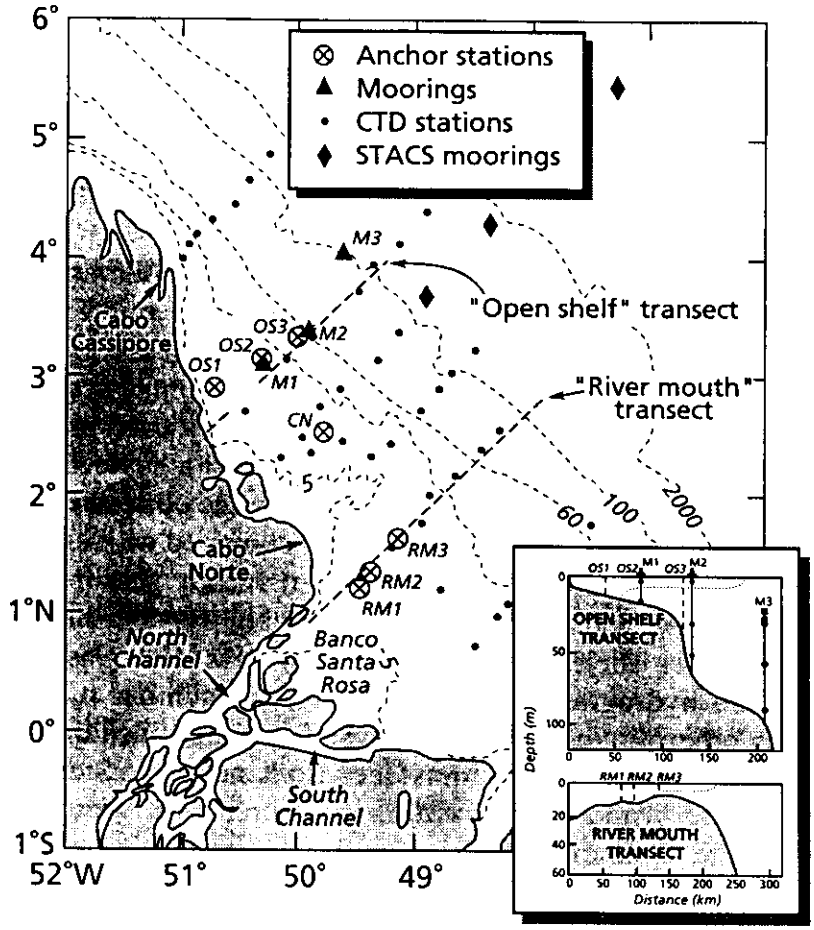

Fig. 3. Measurement locations for major components of the AmasSeds physical oceanography program. Moored instruments were deployed from February to April 1990. Shipboard measurements (including hydrographic and ADCP surveys, anchor stations and drifter releases) were performed during four cruises in August 1989, March 1990, May–June 1990 and November 1991. Also shown, are the locations of moorings deployed from September 1989 to January 1991 as part of the STACS program.

four Marsh–McBirney electromagnetic current meters for measuring the near-bed shear, a high frequency pressure sensor for determining wave forcing and other instruments for monitoring sediment transport and deposition (Cacchione *et al.*, 1995; Sternberg *et al.*, 1996). A wave-rider buoy deployed at M1 was lost.

An additional moored array was deployed seaward of the AmasSeds array, as part of the Subtropical Atlantic Climate Studies (STACS) program (Johns *et al.*, 1990). Three moorings were deployed between September 1989 and January 1991 at depths of 483, 2037 and 3421 m, along a line perpendicular to the shelf break, roughly continuing the AmasSeds array off the shelf (Fig. 3).

Satellite-tracked drifters were deployed during each cruise to obtain direct Langrangian current measurements over the Amazon shelf. The Draper Lab Low Cost Drifters (LCDs) consist of a small surface float attached to a holey sock drogue, centered at 2.5–10-m depth. Usually, two drifters were released near the river mouth during each cruise, with the drogue depth chosen for the float to track the surface freshwater plume or the underlying water. Satellite imagery was obtained from the NOAA Advanced Very High

Resolution Radiometer (AVHRR) to determine surface reflectance, which is related to the surface suspended-sediment concentration (Stumpf *et al.*, 1993).

TIDES ON THE AMAZON SHELF

Ocean forcing

Tides on the Amazon shelf are forced primarily by the deep ocean tides. Cartwright *et al.* (1991; referred to as CRS91) constructed cotidal charts of the principal semi-diurnal and diurnal tides in the Atlantic Ocean. These were based on a harmonic analysis of sea-surface height; estimates were made using GEOSAT altimeter data obtained during the Exact Repeat Mission. Their charts show that the three principal semi-diurnal constituents each exhibit a broad region of small phase change and large amplitude adjacent to the Amazon shelf, with amplitudes varying from 70–85 cm for M_2. The relative amplitudes of the two smaller constituents S_2 and N_2, to M_2, are about $S_2/M_2 = 0.31$ and $N_2/M_2 = 0.21$, respectively, indicating a large spring-neap variation $[(M_2 + S_2)/(M_2 - S_2) = 1.9]$ and monthly variation $[(M_2 + S_2 + N_2)/(M_2 - S_2 - N_2) = 3.2]$ in semi-diurnal forcing. The diurnal tides on the Amazon shelf are much smaller, with the two principal constituents K_1 and O_1 each having an amplitude of 6–8 cm near the Amazon shelf. Thus the primary tidal forcing on the Amazon shelf is semi-diurnal, with the M_2 being the dominant constituent.

Shelf response

The response of the Amazon shelf to the offshore semi-diurnal tidal forcing is complex, in part because of the topography of the Amazon river mouth and shelf region. Figure 4

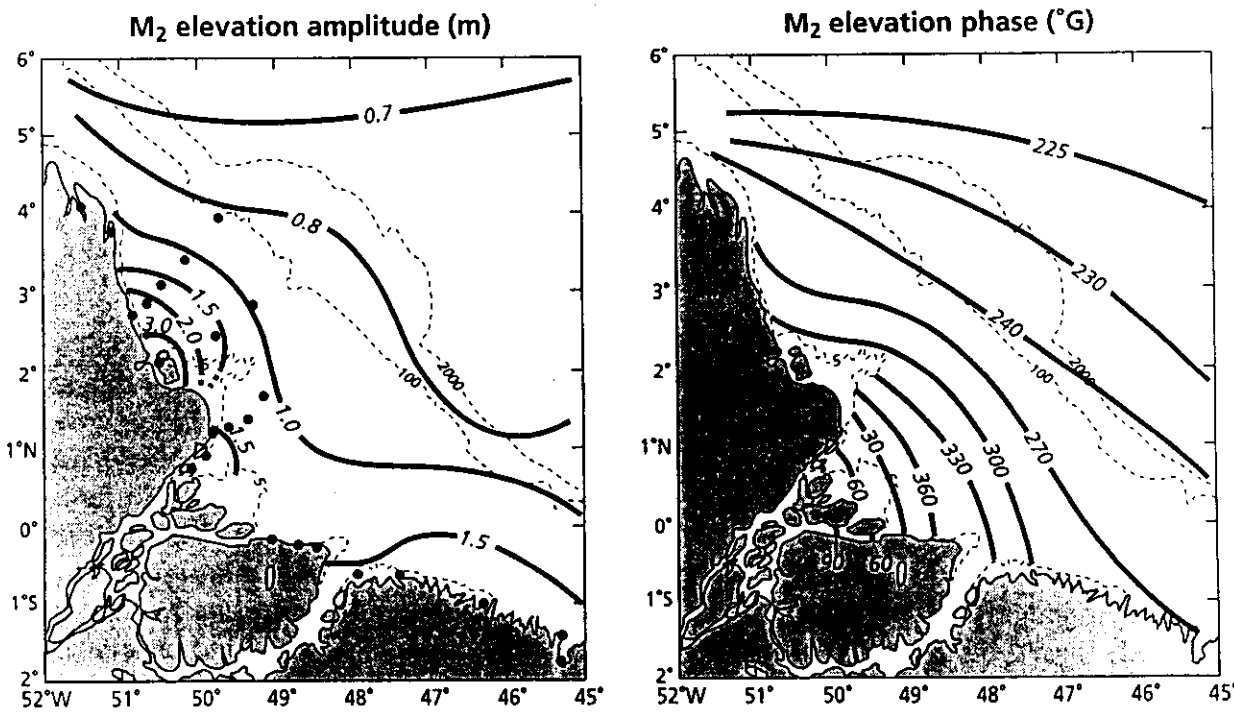

Fig. 4. M_2 elevation amplitude (m) in left panel and elevation phase (°G) in right panel for Amazon shelf. These cotidal charts have been drawn from elevation data at the shelf stations, denoted by dots, and altimetric results from CRS91 seaward of the shelf break. (From Beardsley *et al.*, 1995; reproduced with permission of the American Geophysical Union.)

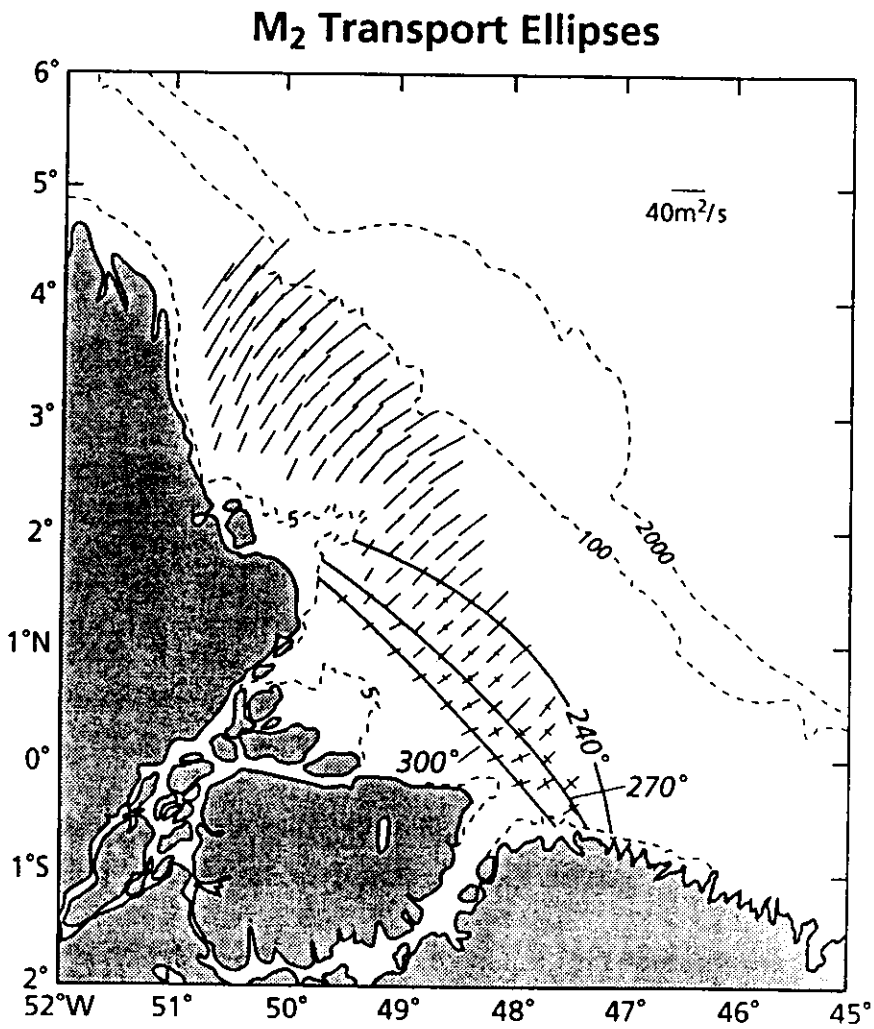

Fig. 5. M_2 volume transport cotidal chart for the Amazon shelf, based on an empirical fit of 1327 hourly averaged ADCP transport measurements and anchor and moored current time series collected during AmasSeds. The fit is based on polynomial spatial functions with tidal periodicity. The fitted transport ellipses are shown with the phase of maximum landward (flood) flow, given in °G, with a contour interval of 30°. (From Beardsley *et al.*, 1995; reproduced with permission of the American Geophysical Union.)

presents cotidal charts for the M_2 surface elevation and transport fields over the Amazon river mouth and shelf, as constructed by Beardsley *et al.* (1995). The elevation cotidal charts combine CRS91 offshore elevation information with AmasSeds moored and anchor-station data and with Brazilian Navy coastal sea-level data to show contours of equal elevation amplitude and Greenwich phase of maximum elevation. The transport chart (Fig. 5) illustrates the M_2 transport ellipse (showing the semi-major and semi-minor axes, their geographical orientation and phase of the maximum transport in the direction of flood), based on an analysis of the AmasSeds shipboard ADCP and moored current data, using the empirical approach developed by Candela *et al.* (1992).

The M_2 tidal wave generally propagates landward across the shelf and into the Amazon and Para Rivers. However, there is a marked difference in the structure of the M_2 tide in front of the river mouth and over the shelf to the north, between Cabo Norte and Cabo Cassiporé. In this northern shelf region, the M_2 tide reaches a maximum amplitude in

excess of 3 m for the nearshore area, where the shelf width is a maximum. The phase lag in maximum elevation between the shelf break and the coast is roughly 75°. The M_2 transport ellipses are nearly rectilinear and oriented across the local topography. The maximum transport occurs near the shelf break and the semi-major axes decrease monotonically in the landward direction. There is some veering in the orientation of the ellipses in this region, to follow the northern coastline as the wave progresses landward. There is little cross-shelf phase lag in transport, so that the phase difference between M_2 elevation and transport increases from roughly 45° at the shelf break to over 80° nearshore. This change in the relative phase of elevation to transport indicates that the M_2 tide approaches a damped standing wave as it propagates across the shelf into this region.

South of Cabo Norte, the M_2 tidal wave propagates across the shelf and into the Amazon and Para Rivers, primarily as a damped progressive wave, consistent with the well-known observation that the semi-diurnal tides propagate upriver through the river mouth (Defant, 1961; Ferraz and A'dCarvalho, 1975). The M_2 elevation reaches a maximum amplitude of approximately 1.5 m at the entrances of the Amazon North and South Channels and the mouth of the Para River, and then decays slowly upstream. The M_2 transport ellipses are generally oriented across the topography into the river mouths, but are less rectilinear, especially near the Para River. The semi-major axes decrease in magnitude onshore. Both M_2 elevation and transport show a continuous increase in phase as the tide progresses across the shelf and upriver, with a mean difference between elevation and transport phase of roughly 30° within the North Channel. South of the Para River, the M_2 tide behaves more as a damped standing wave, with less phase lag across the shelf and a maximum elevation amplitude of roughly 1.9 m at the coast near 46.5°W. The other principal semi-diurnal constituents, S_2 and N_2 (not shown), exhibit qualitatively similar behavior over the Amazon shelf and river-mouth region.

Vertical structure

The vertical structure of the semi-diurnal tidal currents was examined at AmasSeds anchor stations and the M2 mooring site. Figure 6 shows a sequence of vertical profiles of velocity, salinity and suspended-sediment concentration obtained over one semi-diurnal tidal cycle at the Open-Shelf anchor station OS2 (Fig. 3) during 15 March 1990. These observations are qualitatively similar to other anchor-station observations made in the frontal zone (Geyer and Kineke, 1995). The cross-shelf velocity component is dominated by the semi-diurnal tidal flow, with an amplitude of 140–160 cm s^{-1}. The along-shelf velocity component also exhibits a semi-diurnal variation, although of smaller amplitude. This station is located on the seaward side of the near-bottom frontal zone (between brackish riverine and salty shelf water) which tends to parallel the 10-m and 15-m isobaths. The large temporal fluctuations in salinity at the site are due principally to the cross-shelf advection of the front by the tidal current, with minimum near-bottom salinities occurring at the end of ebb.

The oscillatory tidal flow has an interior region of minimum vertical shear located above a bottom boundary layer of thickness 3–4 m. The concentration of suspended sediment increases roughly exponentially near the bottom, reaching maximum concentrations well above 10 g l^{-1} in the bottom 1–2 m at this station. Trowbridge and Kineke (1994) have shown that these fluid muds tend to stably stratify the near-bottom flow and lead to greatly reduced near-bottom stress. As a result, the tidal boundary layer over a fluid-mud layer is

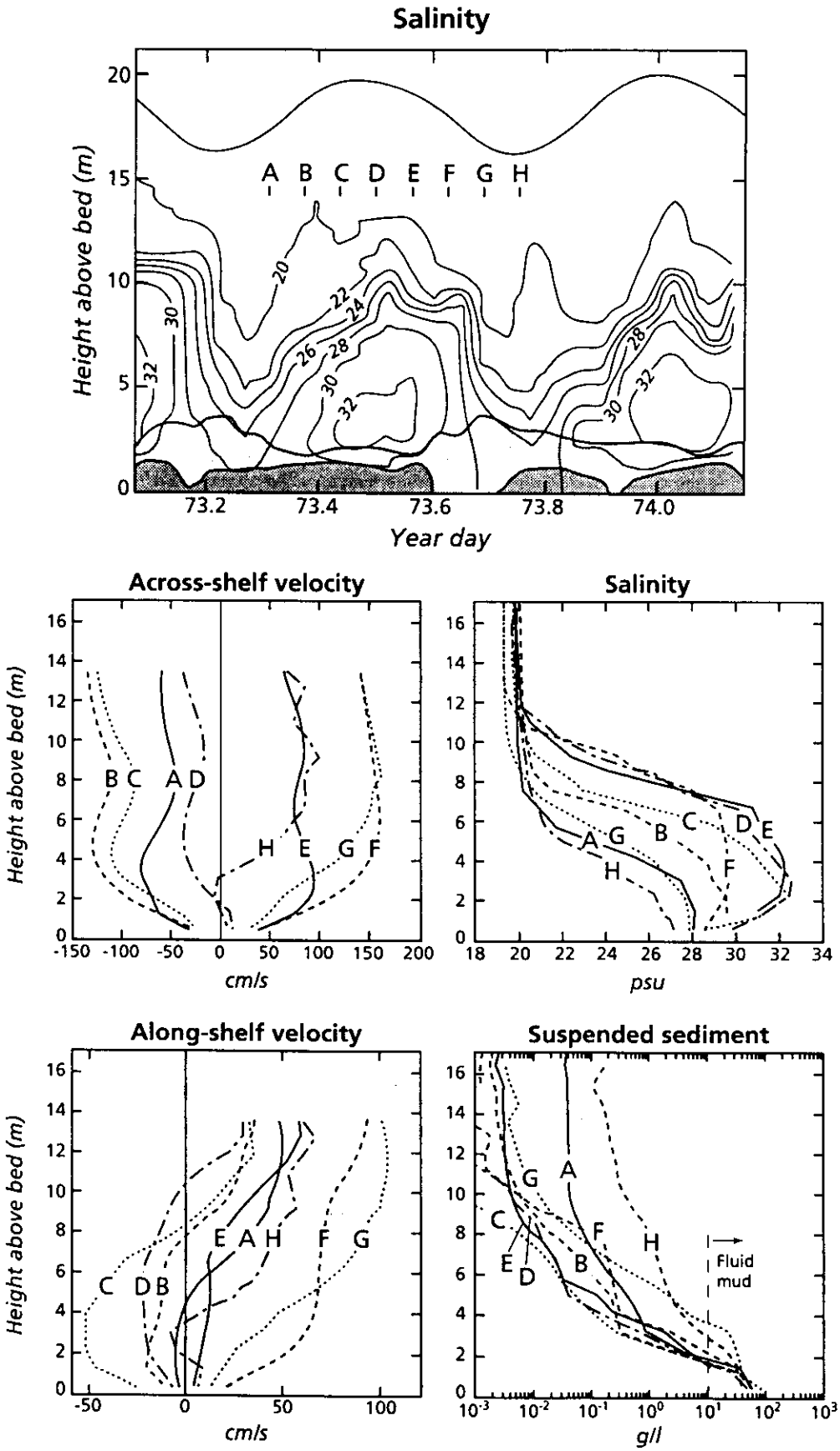
Salinity
Height above bed (m)
Year day
A B C D E F G H
Across-shelf velocity
cm/s
Salinity
psu
Along-shelf velocity
cm/s
Suspended sediment
g/l
Fluid mud

much thinner (in the order of a few meters) than would be expected for an unstratified flow over a flat sandy bottom (where the boundary layer would extend through the water column), and the effective friction exerted by the bottom on the overlying fluid can be greatly reduced. Because fluid muds are found near the mouth and over much of the subaqueous delta between Cabo Norte and Cabo Cassiporé (Kineke and Sternberg, 1995) their influence on the dynamics of the tides is significant and will be discussed below.

At the M2 mooring site, the depth-averaged semi-diurnal tidal currents are oriented within 5° of the cross-isobath direction and the M_2 component has a maximum amplitude of about 70 cm s^{-1} at a height of roughly 11 m above the bottom. The surficial sediments at this site are relatively consolidated with no fluid mud and the near-bottom velocity profiles are characteristic of a homogeneous log layer (corrected for tidal acceleration and deceleration effects) during periods of stronger flows when bottom stresses are large, i.e. friction velocity $u_* > 1$ cm s^{-1} (Cacchione *et al.*, 1995). The near-bottom M_2 current leads the near-surface current by approximately 30° (about 1 h), consistent with an oscillatory frictional bottom boundary layer (e.g. Soulsby, 1990).

The M_2 velocity profile at the M2 mooring site exhibits a subsurface maximum above the bottom boundary layer, which suggests the presence of an internal tide, centered about the strong pycnocline at 5–10 m depth. Beardsley *et al.* (1995) used the two-layer model of Rattray (1960) to show that the barotropic, semi-diurnal tidal currents over the seaward face of the subaqueous delta can excite an internal tide in the stratified water column, which radiates both landward and seaward from the delta face. The model predicts that less than 5% of the incident barotropic tidal energy is converted into the internal tide, so that the dynamics of the semi-diurnal tide are not strongly modified by stratification. This internal tidal motion is distinct from the interactions between the tides and the density structure within the bottom salinity front, which occurs approximately 50 km landward of the M2 mooring (see the section on the Amazon River outflow, the frontal zone).

A conceptual model for the M_2 tide

Beardsley *et al.* (1995) have constructed a simple conceptual model for the barotropic M_2 tide over the Amazon shelf, based on the cotidal charts shown in Fig. 4 and other AmasSeds data. They applied a simple variable-width-channel tidal model to the observed elevation and transport data obtained in the Cabo Norte–Cabo Cassiporé region, and found that the best data/model fit was obtained when: (a) the channel width was reduced nearshore to model the convergence of the effective coastline, as the tidal wave propagates onshore between the Cabo Norte shoal and Cabo Cassiporé, and (b) the bottom (spatially constant) drag coefficient was reduced to $C_D = 0.0013$. The Cabo Norte shoal extends

Fig. 6. Tidal variations of velocity, salinity and suspended-sediment concentration at open-shelf anchor station OS2 on 15 March 1990. Top panel shows salinity, water depth and fluid-mud thickness as a function of time through a 25-h sampling period. The fluid-mud layer is shown as stippled, with suspended-sediment concentrations exceeding 10 g l^{-1} and 50 g l^{-1} indicated by light and dark stippling, respectively. The lower panels show vertical profiles of along- and cross-shelf current, salinity and suspended-sediment concentration, observed at 2-h intervals during the times indicated by letters A–H in the top panel. Note that the region of high shear in the cross-shelf velocity profiles is confined to the lowest 2–5 m of the water column, indicating that most of the tidal boundary layer occurs in the fluid-mud layer. (Adapted from Geyer and Kineke, 1995; reproduced with permission of the American Geophysical Union.)

roughly 90 km offshore, with water depths less than 5 m (see Fig. 1), and acts as a partial barrier to separate the tide as it propagates into the North Channel and the Cabo Norte–Cabo Cassiporé embayment. This partial barrier causes convergence of tidal energy within the embayment and leads to local resonance, with maximum elevation at the head. The resonant period of this embayment is approximately 11.9 h. The variable-width-channel model also indicates that most of the tidal-energy dissipation occurs over the middle and inner shelf (in water depths less than 20 m), where the tidal currents are largest and fluid muds may be present. Trowbridge and Kineke (1994) showed that a fluid-mud layer (like that shown in Fig. 6) can reduce the local bottom drag coefficient to minimum values as low as $C_D = 0.00016$. The data/model comparison suggests that the M_2 tide, in essence, integrates over spatial variations in the fluid-mud distribution on scales up to 50 km, resulting in a significant reduction in the bottom stress (and bottom drag coefficient) experienced by the tide.

Beardsley *et al.* (1995) also applied the variable-width-channel tidal model to the North Channel region. Although there was less field data for comparison, the best data/model fit supports the idea that the M_2 tide propagates cross-shelf and upriver as a damped progressive wave, with the effective bottom friction reduced by fluid muds in the river mouth.

THE AMAZON RIVER OUTFLOW

The Amazon River outflow goes through several different zones on the shelf, each with distinct hydrographic characteristics and dynamics. Figure 7 provides a schematic of these different zones. The river-mouth zone is the shallow, well-mixed region where the Amazon debouches onto the shelf. The inner shelf is the shallow (<15 m) well-mixed zone extending northwestward along the coast. The frontal zone is a region of strong near-bottom salinity gradients, across which the bottom-water salinity increases from nearly fresh to oceanic values. The plume is the surface layer of brackish water, typically less than 10 m thick, which extends seaward from the frontal zone over the outer shelf. The outer shelf is defined here as the region seaward of the frontal zone and beneath the plume, extending from roughly the 20-m isobath to the shelf break.

The river mouth and inner-shelf

The Amazon River joins the shelf through two main channels, the North and South Channels. These channels are approximately 10 km wide and 20 m deep as they wind through a network of islands toward the sea. It is generally presumed that most of the freshwater discharge goes through the North Channel, based on the observed salinity anomalies (Lentz and Limeburner, 1995), although we are not aware of any direct observations of relative discharge. If one assumes that 65% of the flow passes through the North Channel, the mean outflow during high discharge would be 160,000 $m^3 s^{-1}$, which would correspond to a net seaward velocity of 80 cm s^{-1}. Although this is quite an energetic outflow, tidal velocities of up to 250 cm s^{-1} (United States Defense Mapping Agency, Chart 24320) are strong enough to reverse the flow within both channels.

The water in the river-mouth channels is believed to be entirely fresh even at low discharge, based on observations by Gibbs (1970). These are supported by AmasSeds observations during November 1991, which indicate that 2-psu water never got closer than

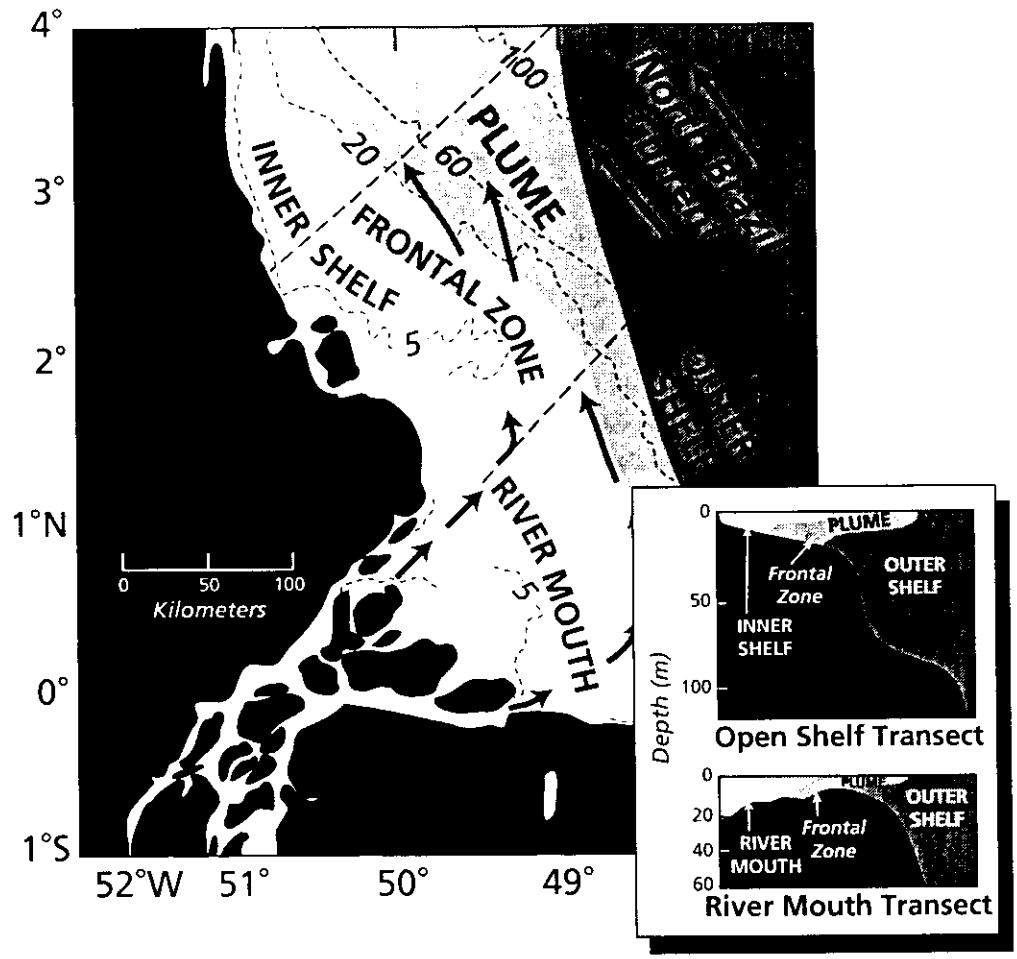

Fig. 7. Schematic showing the different regions of the Amazon shelf, as described in the text. The river-mouth region is perennially fresh. Along the shelf to the north is the well-mixed but brackish inner-shelf water. Seaward of these two regions is the frontal zone, the transition between well-mixed and highly stratified conditions. Beyond and seaward of the frontal zone is the plume and beneath the plume is the outer-shelf water, which appears to be indistinguishable from water of the North Brazil Current.

60 km seaward of the mouth of the North Channel (Limeburner *et al.*, 1992). The freshness of the Amazon mouth is maintained in part by the magnitude of discharge, which even during low flow is enough to produce a strong, net seaward current at the mouth (in a tidally averaged sense). It is also maintained by the strong vertical mixing associated with tidal flow that occurs over the broad inner-shelf region, which breaks down the vertical density structure before the salinity intrusion can reach the river-mouth channels.

As the fresh water leaves the river-mouth region, most of it is directed across the inner shelf into the frontal zone and the plume. An unknown fraction of fresh water appears to continue along the coast, crossing the Cabo Norte shoal. This inference is based in part on satellite images of surface reflectance obtained in August 1989 (Fig. 8), which show streaks in turbidity that may be indicative of the direction of near-surface flow. The orientation of the streaks on 1 August 1989 suggests that the surface water is flowing around the shoal, but on 9 August, the turbidity suggests that the flow is directed over the shoal. The very shallow water on the shoal, combined with the strong tidal currents on the inner shelf, should maintain well-mixed conditions and should impede the along-shelf flow due to tide-, wind- and wave-induced turbulence. This well-mixed inner-shelf region does not

appear to be a major conduit of fresh water, based on tidally averaged velocity data at the inner Open-Shelf anchor station (OS1, Fig. 3), which indicates weak (0–30 cm s^{-1}) along-shelf flows, compared to the 50–100 cm s^{-1} along-shelf flows observed in the frontal zone and plume (Geyer and Kineke, 1995; Lentz, 1995a). The sedimentary characteristics of the shoreline to the north of Cabo Norte (Allison *et al.*, 1995) indicate that little Amazon sediment accumulates; in fact the shoreline is erosional until Cabo Cassiporé, where the sediment-laden frontal zone approaches the coast.

The frontal zone

The frontal zone is defined here as the transition region between the well-mixed nearshore waters and the strongly stratified, surface plume that extends over the middle and outer shelf. It is distinguished by a strong, cross-shelf gradient in near-bottom salinity that extends continuously along the inner shelf from the Para River to Cabo Cassiporé, between the 10- and 20-m isobaths (Fig. 9). The seaward limit of the frontal zone (where the bottom salinity reaches 35–36 psu) is remarkably constant in position, occurring close to the 20-m isobath in all observations. However, the landward extent of the front varies by as much as 80 km, due mainly to variations in river discharge and tidal amplitude (Geyer, 1995). The front extends farther landward during neap tides and low discharge. The mean position of the front on the River-Mouth Transect is close to the crest of transverse shoal (approximately 9.5 m depth). It roughly follows the 10-m isobath across the river-mouth region, deepening to the 15-m isobath as it extends to the north.

Transverse structure of the frontal zone. Examples of the observed transverse structure in the frontal zone at the River-Mouth and Open-Shelf Transects are shown in Fig. 10. These observations were obtained during high run-off conditions in June 1990. At the River-Mouth Transect, low-salinity water is observed near the surface on the landward side of the front. A pronounced bottom salinity front is found near the crest of the river-mouth bar, across which the salinity increases from 10 to 25 psu in 10 km. Seaward of the bar, the near-bottom salinity continues to increase, reaching 36 psu near the 20-m isobath, where the bottom slope becomes steeper near the edge of the foreset beds. The bottom salinity front is the lift-off point for the Amazon plume, which is seen here extending at least 60 km beyond the front in the upper water column.

Also shown, are contours of fluid-mud concentration. The fluid-mud layers are thickest and have the highest concentrations at the bottom salinity front. The suspended-sediment distribution is similar to an estuarine turbidity maximum and similar processes appear to contribute to sediment trapping in the Amazon frontal zone, as in other estuarine regimes (see Kineke *et al.*, 1996).

The tidally averaged, cross-shelf velocity obtained at the RM2 anchor station is indicated by arrows. Cross-shelf velocities of 55 cm s^{-1} are observed in the surface layer, dropping to 10 cm s^{-1} near the bottom. This flow is slightly stronger but similar in structure to other current observations obtained at the River-Mouth anchor stations (Geyer and Kineke, 1995). Not shown, is a strong along-shelf component of flow observed during this anchor station, which reaches 80 cm s^{-1} near the surface and drops to less than 10 cm s^{-1} near the bottom. More typical along-shelf velocities are 10–20 cm s^{-1}, observed during other River-Mouth anchor stations. The vertical shear in the cross-shelf direction indicates that Amazon water is advected across the front into the plume in an estuarine-like manner.

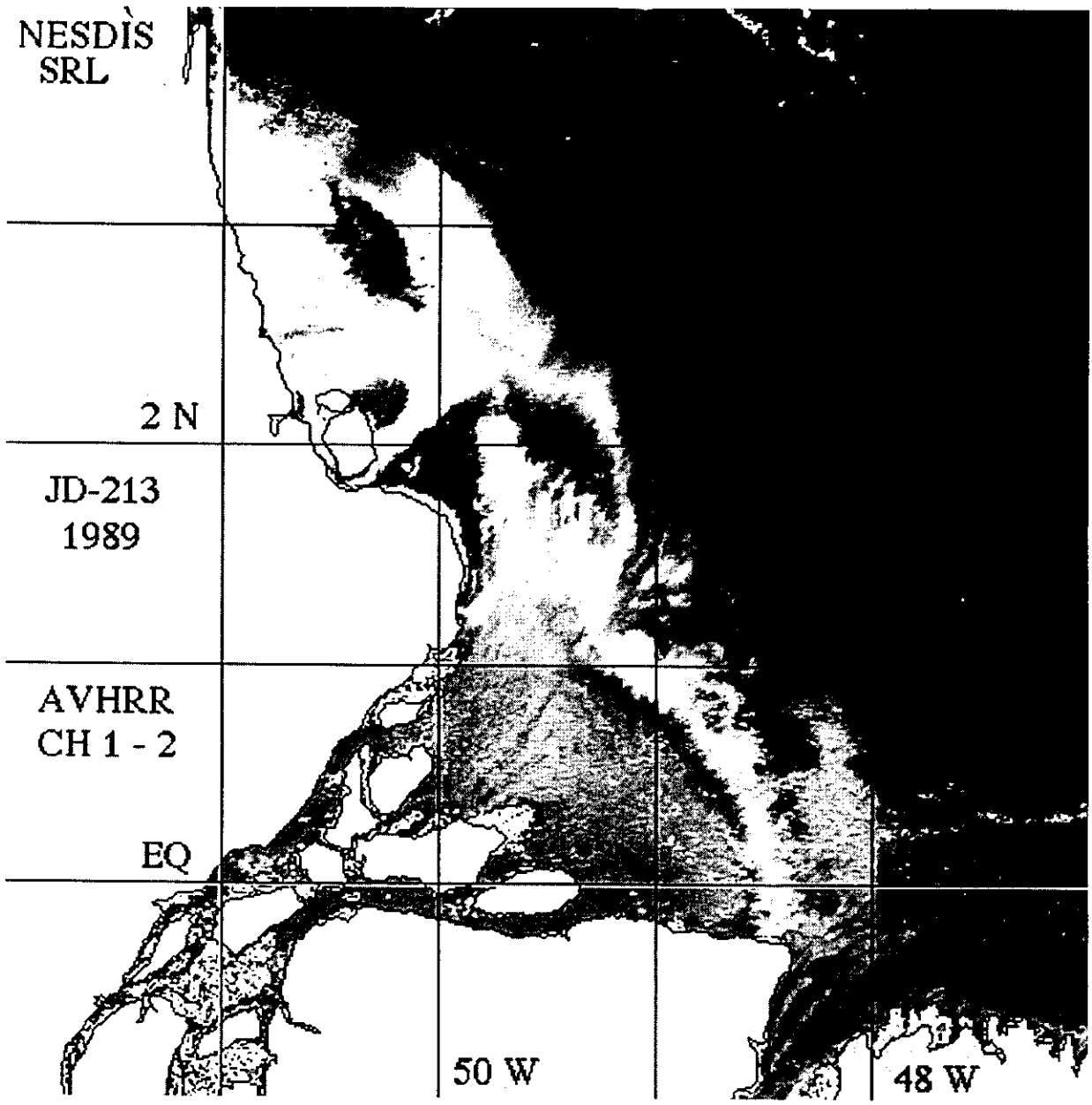

Fig. 8. Satellite images of albedo, using NOAA's Advanced Very High Resolution Radiometer (AVHRR). The images were generated by taking the difference between channel 2 and channel 1. This quantity has been found to correlate well with near-surface suspended sediment in other environments (Stumpf *et al.*, 1993) and it reduces the influence of thin clouds and haze. The plume emanating from the North Channel is evident in the two images. During 1 August 1989 (JD-213), it is directed seaward, but during 9 August 1989 (JD-221), it follows the coast to the northwest. This variability is likely to be associated with variations in wind and possibly with tidal amplitude variations. (Figures supplied by R. Legeckis.)

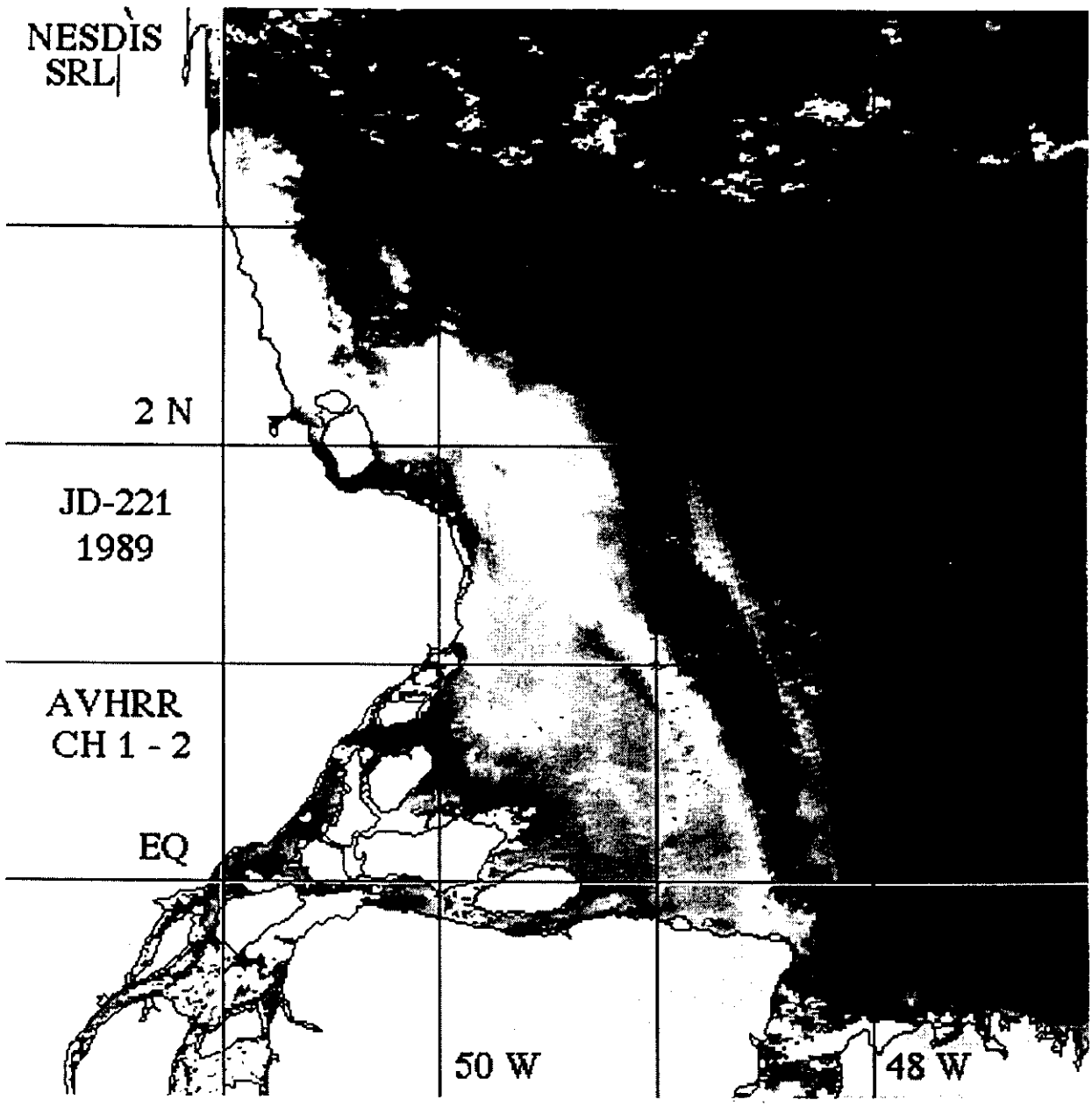

Fig. 8. (*Continued.*)

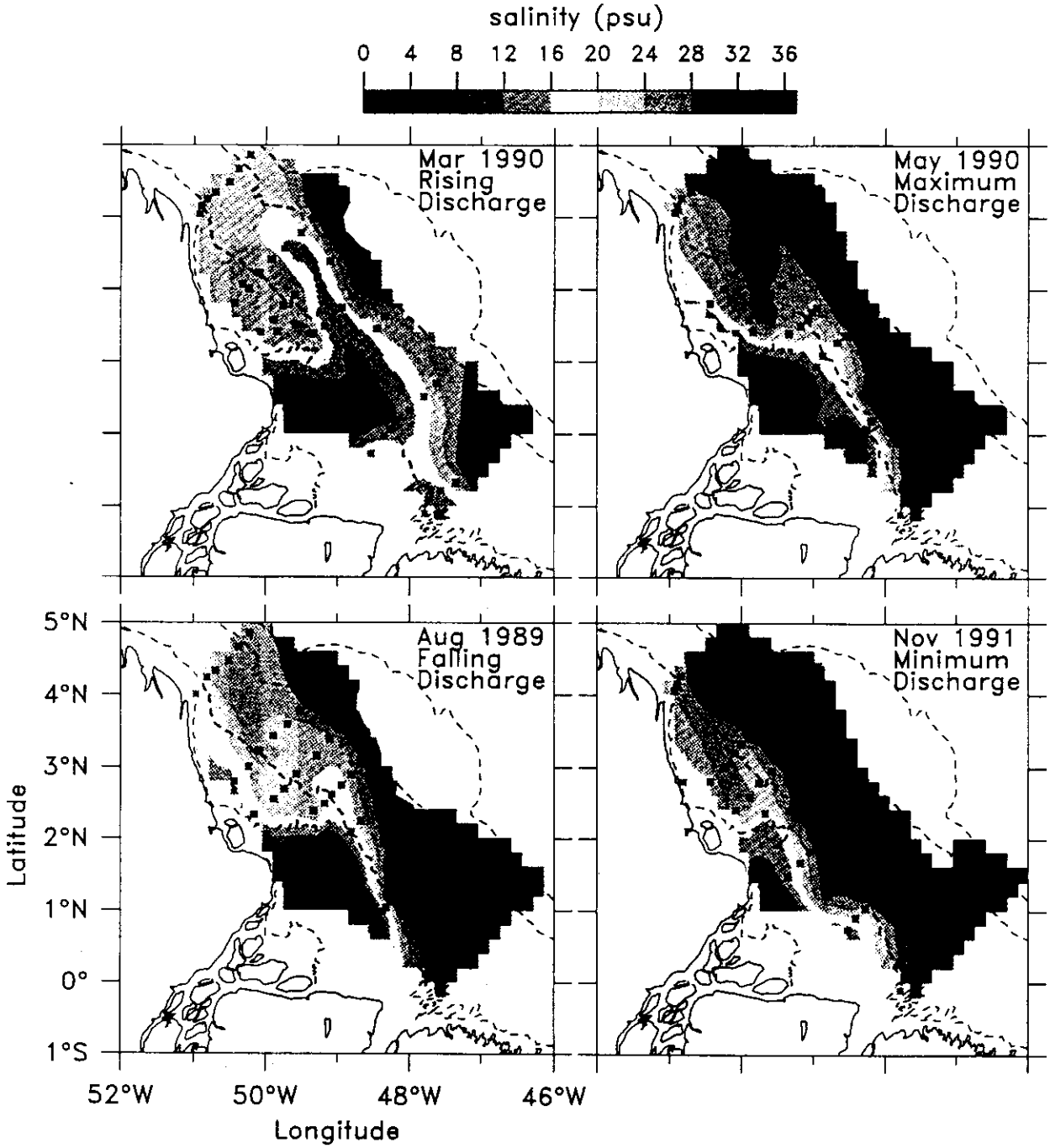

Fig. 14. Near-surface salinity contours obtained during the four large-scale hydrographic cruises, corresponding to different stages in the annual discharge cycle (Lentz and Limeburner, 1995; reproduced with permission of the American Geophysical Union). Much of the variability is not, in fact, due to variations in discharge, but rather to variations in along-shelf winds (see text).

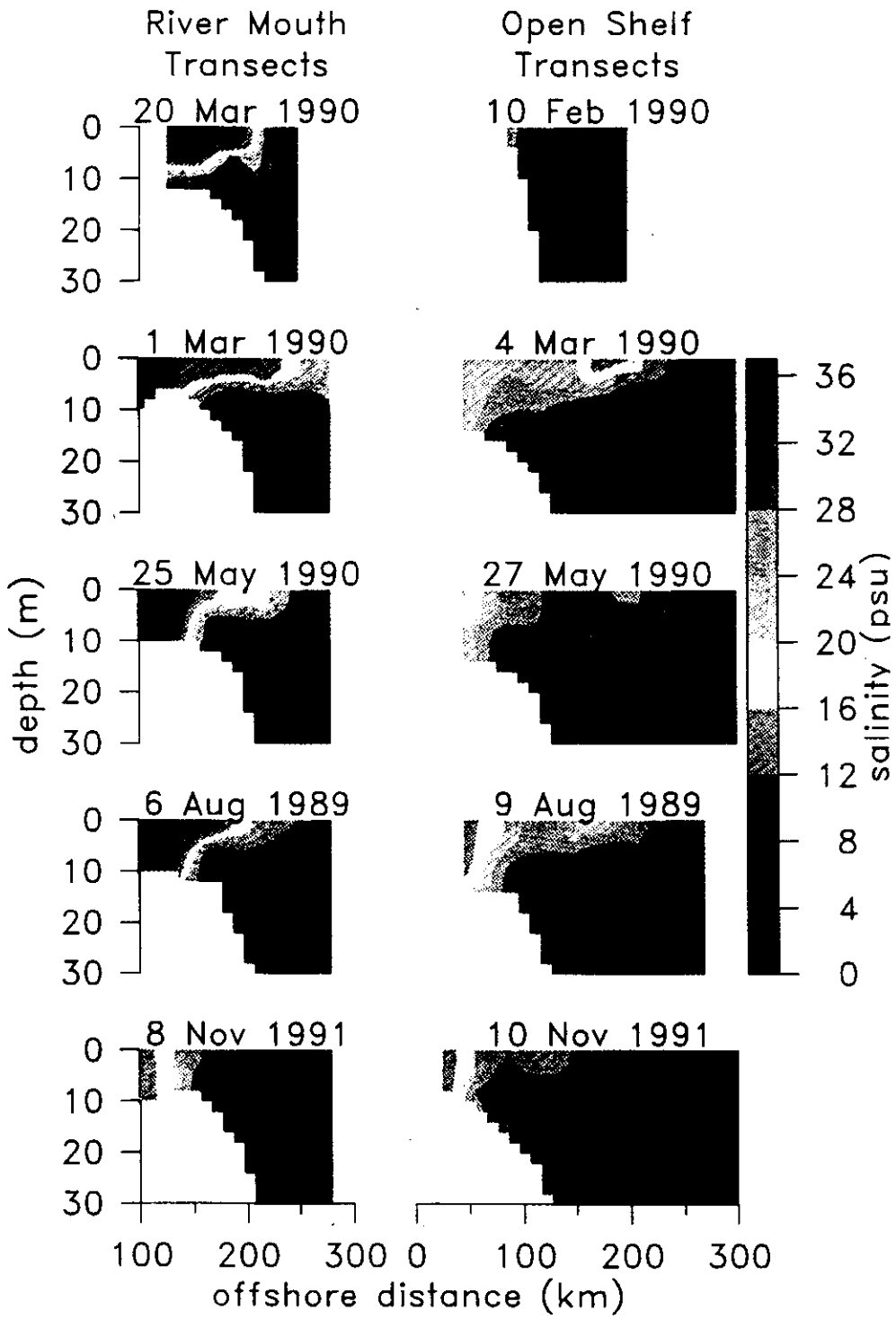

Fig. 15. Cross-sections across the plume at the River-Mouth and Open-Shelf Transects during various surveys, under different wind and run-off conditions (Lentz and Limeburner, 1995; reproduced with permission of the American Geophysical Union). The plume thickness remains nearly constant, but its offshore extent and freshwater content vary tremendously due to variations in atmospheric forcing over the shelf.

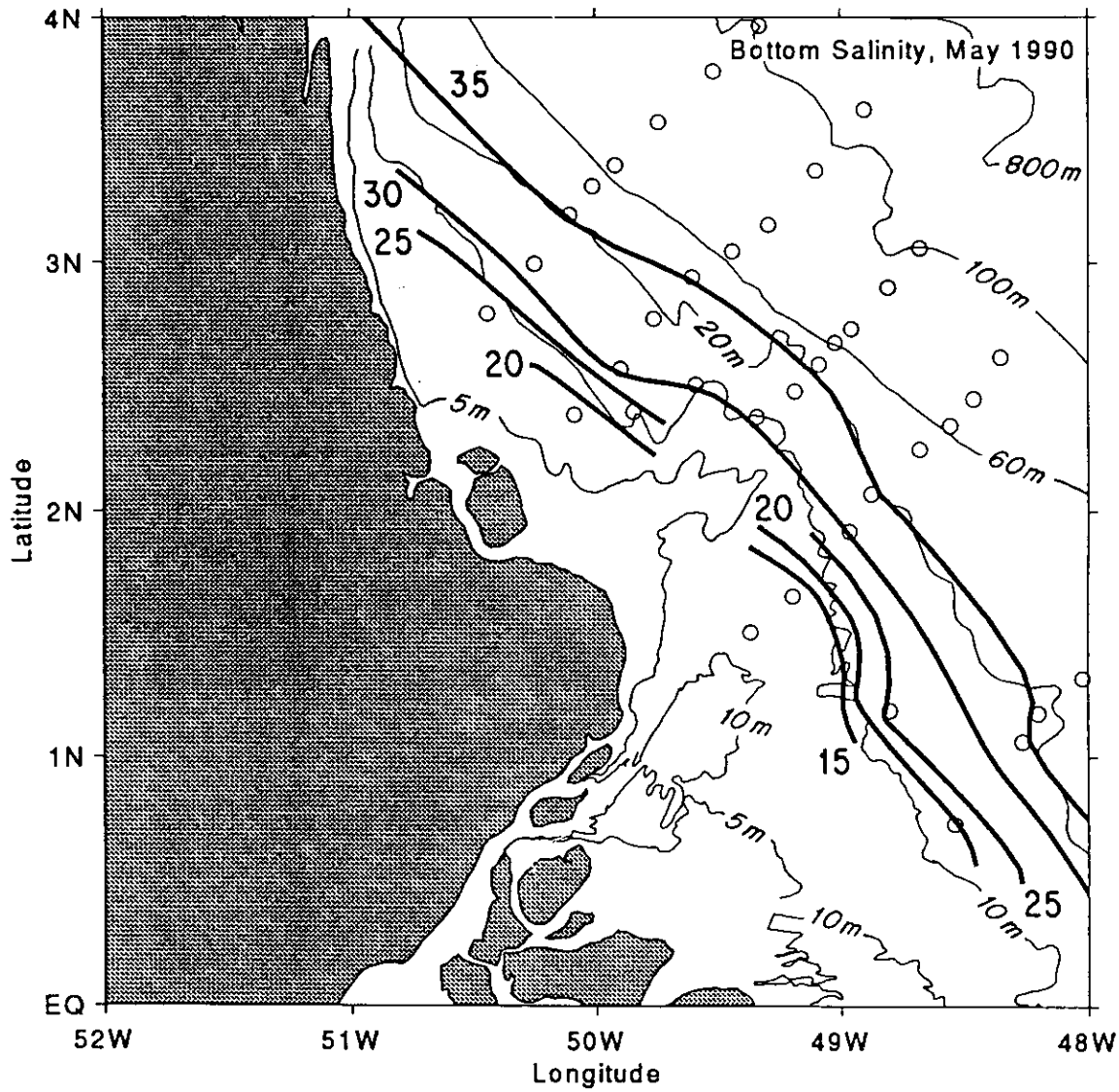

Fig. 9. Contours of near-bottom salinity obtained during the shelfwide hydrographic survey in May 1990. The bottom salinity front follows the general trend of the isobaths, between 10- and 20-m depth. (Adapted from Lentz and Limeburner, 1995.)

However, the absence of a net landward near-bottom flow at this and other River-Mouth anchor stations (except during low-discharge conditions) and the presence of significant along-shelf flow, indicate that the subtidal flow is three-dimensional, unlike the classic two-dimensional estuarine paradigm. The presence of low, but measurable, salinity in the water landward of the front (Fig. 10) also suggests that along-shelf advection contributes to the salt balance (Geyer and Kineke, 1995).

The cross-shelf structure at the Open-Shelf Transect (200 km northwest of the River-Mouth Transect) also indicates a strong near-bottom salinity front, located near the 15-m isobath. The nearshore salinity is considerably higher than at the river mouth, although still well below oceanic values. The plume has a relatively high salinity of 30 psu during this period; however, the salinity of the plume is highly variable, based on moored and shipboard hydrographic data (Lentz and Limeburner, 1995).

The highest concentrations of suspended sediment are located in the vicinity of the

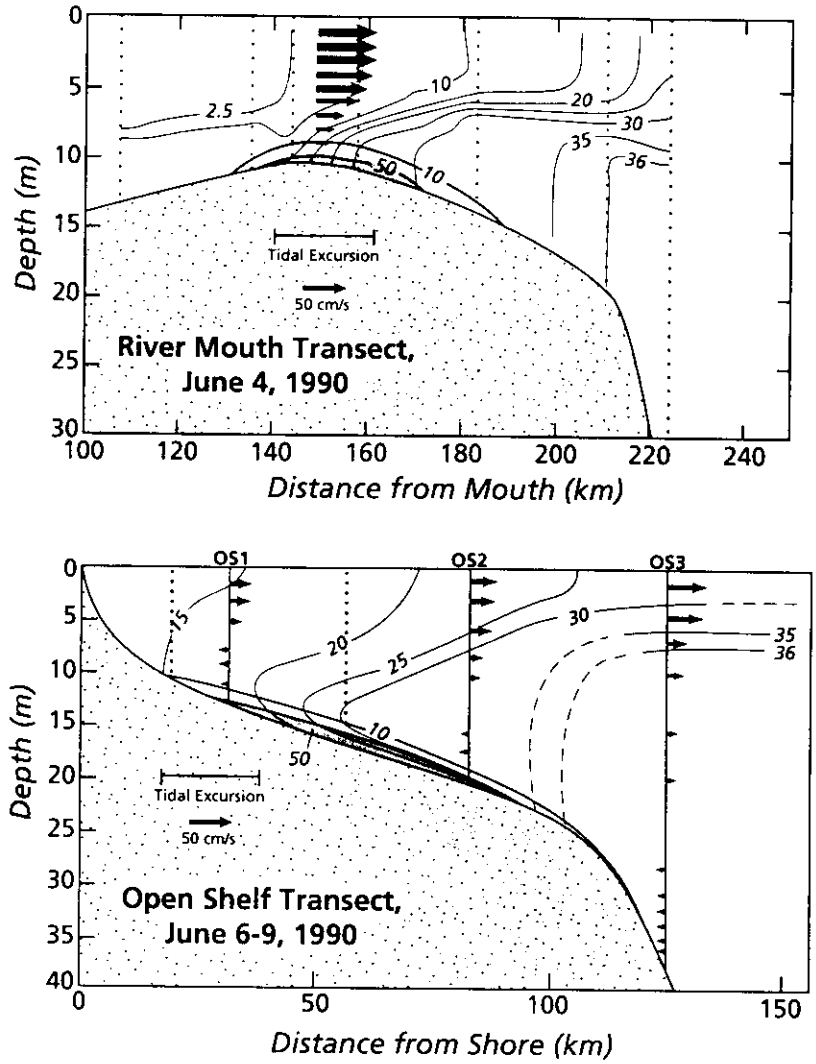

Fig. 10. Cross-sections across the frontal zone at the River-Mouth Transect (upper) and Open-Shelf Transect (lower) obtained in June 1990. Salinity and suspended-sediment contours are shown, as well as vectors indicating the tidally averaged cross-shelf velocity. At the River-Mouth Transect, the tidally averaged flow shows the dominance of the river outflow, with no deep return flow. At the Open-Shelf Transect there is an estuarine-like circulation, driven by the cross-shelf density gradient, as well as upwelling due to Ekman veering in the bottom boundary layer.

bottom salinity front. Near-bottom concentrations at the OS2 anchor station reach more than 200 g l^{-1} and fluid mud extends 1–3 m above the bed (Kineke and Sternberg, 1995). Water with anomalously low salinity is found in the fluid-mud layer. The apparent density inversion is compensated by the fluid mud, which dominates the density variation in the bottom meter of the water column (Kineke *et al.*, 1996). The presence of the near-bottom salinity minimum suggests that there is net seaward advection in the turbid lower layer, carrying sediment from the low-salinity inner shelf toward the foreset beds (Kineke *et al.*, 1996).

The velocity data show a net seaward flow in the surface water of approximately 20 cm s^{-1} and a landward flow of several cm s^{-1} in the deep water. The along-shelf flow (not shown) is much stronger, with near-surface speeds of 30, 70 and 90 cm s^{-1} at the OS1, OS2 and OS3 anchor stations, respectively. The moored observations indicate that there is

considerable temporal variation in the flow at several day and longer time scales (Lentz, 1995a), but the velocities shown in Fig. 10 appear to be representative of conditions during moderate to high river discharge. The cross-shelf flow resembles estuarine circulation and is driven in part by the cross-shelf pressure gradient associated with the salinity gradient. The Coriolis acceleration acting on the vertically sheared, along-shelf flow, reinforces this cross-shelf flow (see section on the outer shelf).

Tidal variations in the frontal zone. The cross-shelf tidal excursion in the frontal zone results in large tidal variations in salinity and stratification. Variations of currents and salinity through a tidal cycle within the frontal zone at the River-Mouth Transect are shown in Fig. 11. These data were obtained at the RM3 anchor station on the crest of the river-mouth bar (Fig. 3) within two days of the transect shown in the upper panel of Fig. 10. Similar variations are observed at the Open-Shelf Transect (Fig. 6). Near-surface salinities remain nearly uniform, but the cross-shelf advection of the bottom salinity front causes large variations in near-bottom salinity.

At both the River-Mouth and Open-Shelf sites, the highest salinities occur 2–3 m above the bottom. Fluid-mud concentrations below the salinity maximum are great enough to stabilize the salinity inversions. The velocity data at the River-Mouth site indicate a pronounced velocity maximum within the halocline during the flood (profile A). During the ebb, the velocity profile has a more uniform gradient (profile E), suggesting that the turbulent boundary layer extends higher into the water column. During extreme spring tides, the boundary layer during ebb at the River-Mouth Transect was found to extend throughout the water column, although most of the observations in the frontal zone indicate that the tidal boundary layer is limited to a small fraction of the water depth. As noted previously, the strong stratification by fluid mud reduces the bottom stress and the vertical penetration of boundary-layer turbulence.

Spring-neap variations in the frontal zone. The salinity structure within the frontal zone was found to vary as a function of tidal amplitude (Geyer, 1995), with a strongly stratified, salt-wedge-like front occurring during neap tides and a more weakly stratified regime during spring tides. Figure 12 illustrates the changes in frontal structure along the River-Mouth Transect between neap and spring tides. The bottom salinity front was found to penetrate farther landward during neap tides; the frontal position (based on the landward extent of the 20-psu salinity contour) was found to vary by 40 km in the cross-shelf direction, due to variations in tidal amplitude. Similar variations in stratification and frontal position are evident at the Open-Shelf Transect, based on moored observations of salinity. In Fig. 13, the cross-shelf velocity at 3-m depth and the near-surface and near-bottom salinity at the M1 mooring indicate that minimum stratification occurs during periods of strong spring tides. The variation of near-bottom salinity also suggests landward and seaward motion of the front, due to spring-neap variations of the tidal amplitude. This was quantified by Geyer (1995), indicating a displacement of 20 km between spring and neap tides at the Open-Shelf Transect.

This spring-neap variation of stratification suggests that tides provide an important mechanism for vertical mixing in the frontal zone. Geyer (1995) found that the vertical shears induced by tidal currents, were large enough during strong spring tides to overcome the stabilizing influence of stratification by salinity and suspended sediment. This was based on estimates of the gradient Richardson number, the ratio of the magnitude of stratification to the shear squared: $Ri = (-g/\rho_o)(\partial\rho/\partial z)/|\partial\vec{u}/\partial z|^2$ (where g is the acceler-

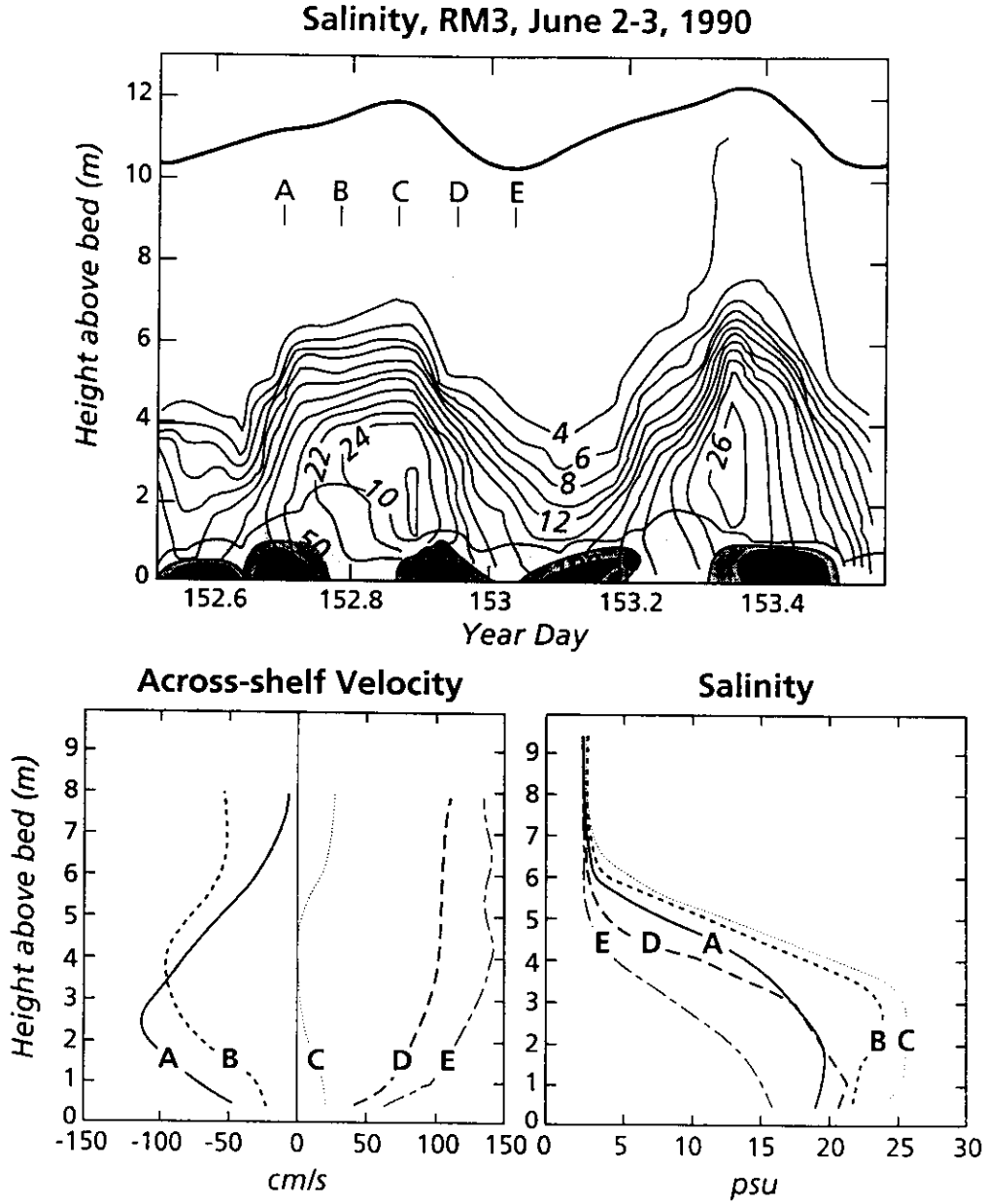

Fig. 11. Salinity and velocity variations at a River-Mouth anchor station during June 1990. Upper panel shows contours of salinity and suspended-sediment concentration as functions of time and depth (from Geyer and Kineke, 1995; reproduced with permission of the American Geophysical Union). Lower panel shows vertical profiles of cross-shelf velocity and salinity at the times indicated in the upper panel.

ation of gravity, ρ_o is the mean density, ρ is the vertically varying density, $\vec{u}$ is the horizontal velocity vector, and z is the vertical coordinate). Based on theoretical (e.g. Miles, 1961) and experimental (e.g. Thorpe, 1971) studies, Ri provides a measure of the stability of a stratified shear flow. When $Ri < 0.25$, the shears become strong enough to overcome the stabilizing density gradient and vertical mixing occurs. During neap tides in the Amazon frontal zone, Ri rarely dropped below the theoretical stability threshold of 0.25 within the pycnocline, but during spring tides there were frequent occurrences of $Ri < 0.25$. Based on the anchor station observations, the 140–200 cm s^{-1} velocities that occur during spring tides usually produce large enough shears to break down the

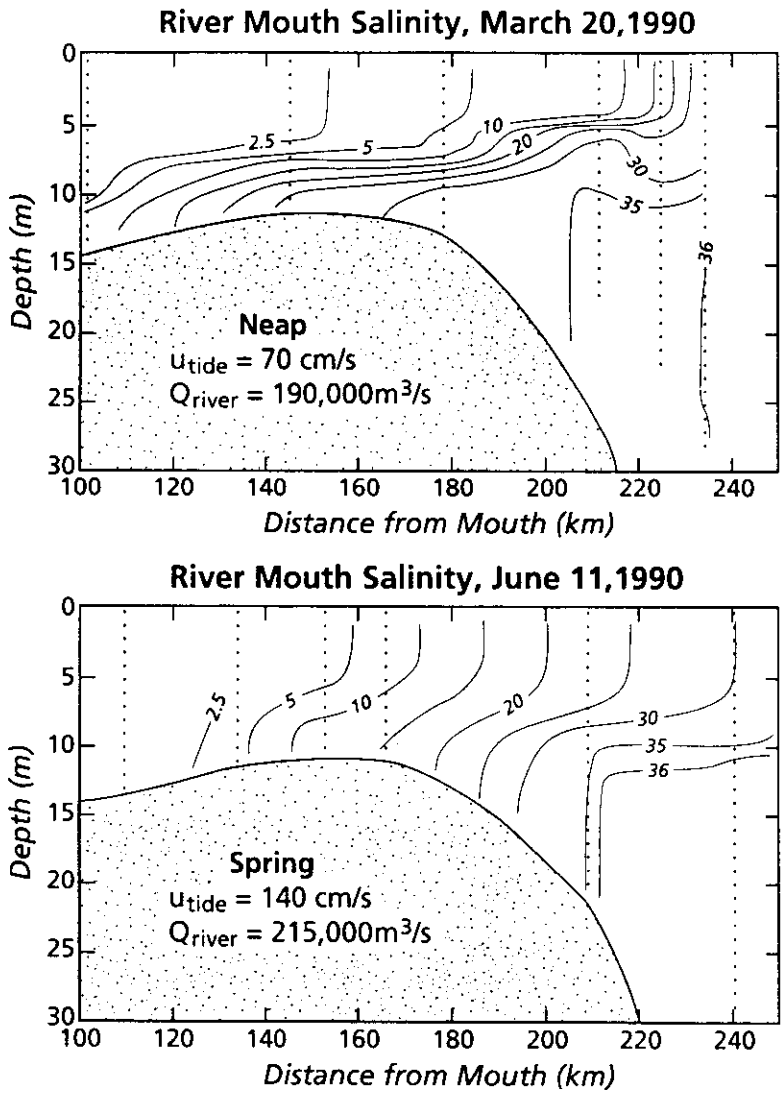

Fig. 12. Salinity sections across the River-Mouth Transect obtained during neap (upper) and spring (lower) conditions (Geyer, 1995; reproduced with permission of the American Geophysical Union). During neap tides, the stratification is much stronger and the front extends farther landward than during spring tides. There is also some influence of discharge variations, although the dominant factor in this example is the variation in tidal amplitude.

stratification in the frontal zone and the 70–100 cm s^{-1} currents that occur during neaps allow the stratification to become re-established.

The density stratification due to suspended sediment was often as large as that due to salinity, thus augmenting the stability of the flow in the frontal zone. In one set of observations in March 1990, the frontal structure persisted during strong spring-tide conditions, due apparently to the increased stratification from fluid mud, which prevented the tidal shear from breaking down the vertical stratification.

The plume

Spatial structure of the plume. After Amazon River water traverses the frontal zone it forms the Amazon plume, a thin but tremendously broad layer of brackish water that can extend from the river mouth many hundreds of kilometers across the shelf and northwest-

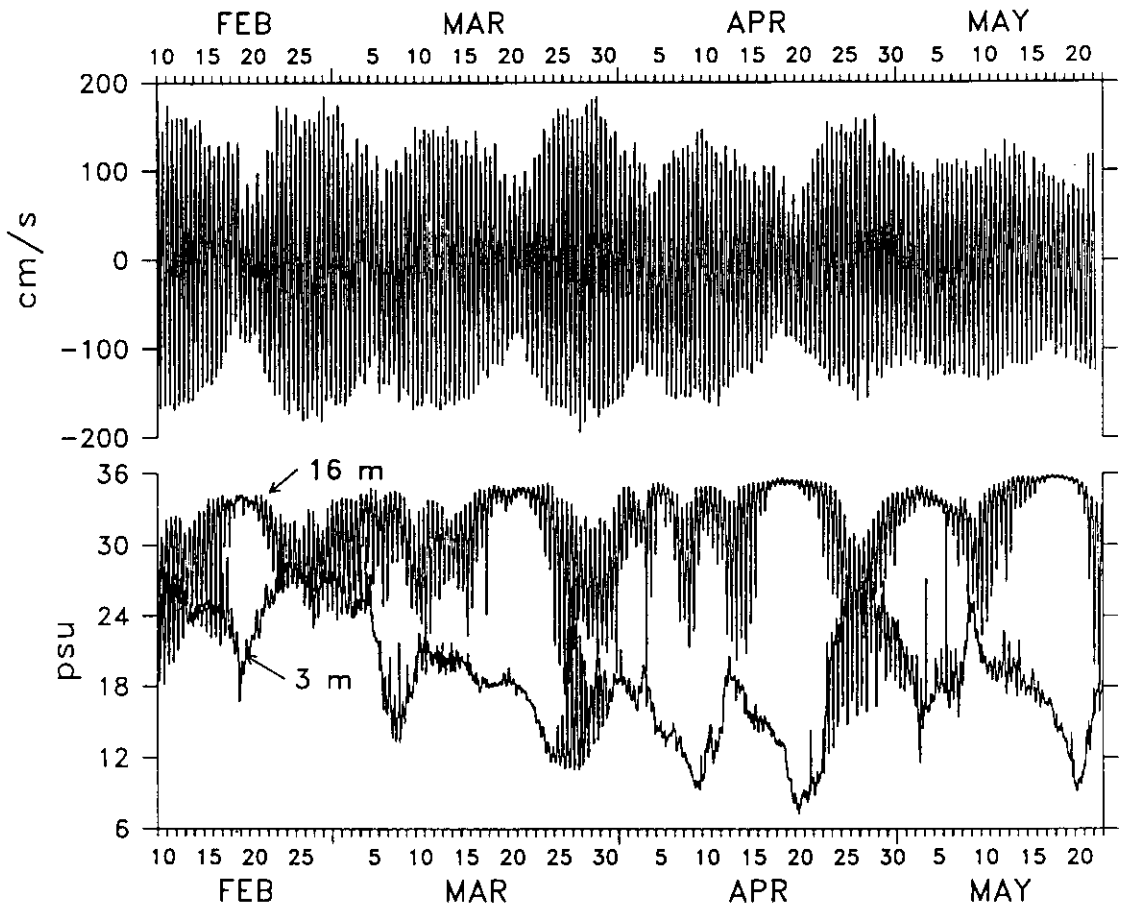

Fig. 13. Time series of velocity and salinity at the inner-shelf M1 mooring. The upper trace is hourly averaged, cross-shelf velocity at 3-m depth, and the lower panel is hourly averaged salinity at 3- and 16-m depth. The tidal motions dominate the record, with a clear indication of the spring-neap variations in magnitude. Vertical stratification, as indicated by the difference between near-surface and near-bottom salinity, also shows spring-neap variation, with maximum stratification occurring during neap tides.

ward along the shelf. Surface salinity maps produced from the four AmasSeds hydrographic cruises illustrate the spatial extent of the plume (Fig. 14). Each survey took approximately seven days to complete, with the ship moving in the direction of the along-shelf flow from southeast to northwest. Due to strong advection over the shelf and large temporal variability at time scales as short as several days, the surveys should not be viewed as either synoptic or as representative of the annual discharge cycle, but instead as approximate descriptions of the plume during different wind and discharge conditions.

In each survey, the low-salinity water was observed to cross the inner shelf at the river mouth, then turn northwestward, forming a tongue of low-salinity water that extends along the middle shelf (Lentz and Limeburner, 1995; Curtin, 1986a,b; Gibbs, 1970). Another zone of low-salinity water was found along the inner shelf, northwest from the river mouth. During all but the March surveys, the seaward limit of the plume extended diagonally across the shelf, suggesting that it spread seaward as it advected to the northwest. During the March survey, the plume bulged seaward from the river mouth beyond the limits of the survey track. The integrated freshwater content on the shelf during March was twice what was found in June, even though the discharge in March was lower than in June (Lentz and Limeburner, 1995). This apparent paradox is explained by

variation in the along-shelf flux of fresh water. When along-shelf flow is strong, the freshwater plume is rapidly carried northwestward, but when the along-shelf flow weakens, fresh water accumulates over the Amazon shelf (Lentz and Limeburner, 1995; Lentz, 1995a). The seaward extent of the plume was most limited during the low-discharge survey, probably reflecting the reduced discharge during this period (Fig. 2).

Sections across the plume illustrate its vertical and cross-shelf structure (Fig. 15). Defined here as the depth of the center of the halocline, the thickness of the plume varied little spatially and temporally from a mean value of 7.3 ± 2.9 m (Lentz and Limeburner, 1995). Beneath the plume, the outer-shelf water had essentially constant salinity of 36.2 psu (except in November 1991, when the ambient salinity increased to 36.3 psu). The salinity within the plume, as well as its seaward extent, varied considerably. Comparison of the Open-Shelf Transects in February and March 1990 indicates that much of the plume variability was not simply due to the seasonal variation of river discharge. Variations in plume extent and salinity appear to be related to variations in wind forcing that occur on time scales of days to weeks (Fig. 2). Although tidal mixing was found to be important within the frontal zone, its influence was not apparent in the plume, probably due to the separation of the plume from bottom-generated turbulence.

Near-surface drifters deployed in the river-mouth region during the four cruises (Fig. 16) showed the northwestward tendency of the plume flow (Limeburner *et al.*, 1995). The trajectories of these drifters were not truly Lagrangian, because they could not follow vertical motions that may be associated with frontal features on the shelf, but they do provide a qualitative assessment of the flow at scales not available with the other measurements. The drifters typically crossed the shelf at a small angle to the isobaths, with mean speeds of 42–128 cm s^{-1} and a maximum along-shelf velocity of almost 200 cm s^{-1}. Many drifters showed strong accelerations near 2°N, which appear to be associated with flow around the Cabo Norte shoal. One of the drifters (deployed in May 1990) crossed the outer shelf before reaching the Cabo Norte shoal, but the others remained on the shelf past Cabo Cassiporé.

Temporal variations of the plume. There is marked variation in along-shelf flow and salinity within the plume on time scales as short as one week, based on the moored current-meter data (shown in Fig. 17; Lentz, 1995a). Near-surface (3-m) salinity observations indicate that the inner-shelf mooring site M1 was always in the plume and the mid-shelf mooring site M2 was in the plume more than 90% of the time. During the mooring deployment, there were several distinct events in which the salinity dropped markedly over the course of several days to one week. Lentz and Limeburner (1995) analyzed the temporal variation of the salinity to determine the relative contributions of vertical mixing, along- and cross-shelf advection to the observed salinity variations. They determined that at the mid-shelf site, the short-term fluctuations in salinity are explained principally by cross-shelf advection of the front, but the large drops in salinity, such as observed in early March and early April 1990, appear to be the result of along-shelf advection. The first of these low-salinity pulses followed the March hydrographic survey, during which the fresh water had accumulated over the shelf due to weak along-shelf flow. The drop in salinity at the M2 mooring occurred when the pool of low-salinity water was transported northwestward, after the along-shelf flow had been re-established. Both the March and April low-salinity events were accompanied by increases in the along-shelf flow at the mid-shelf mooring.

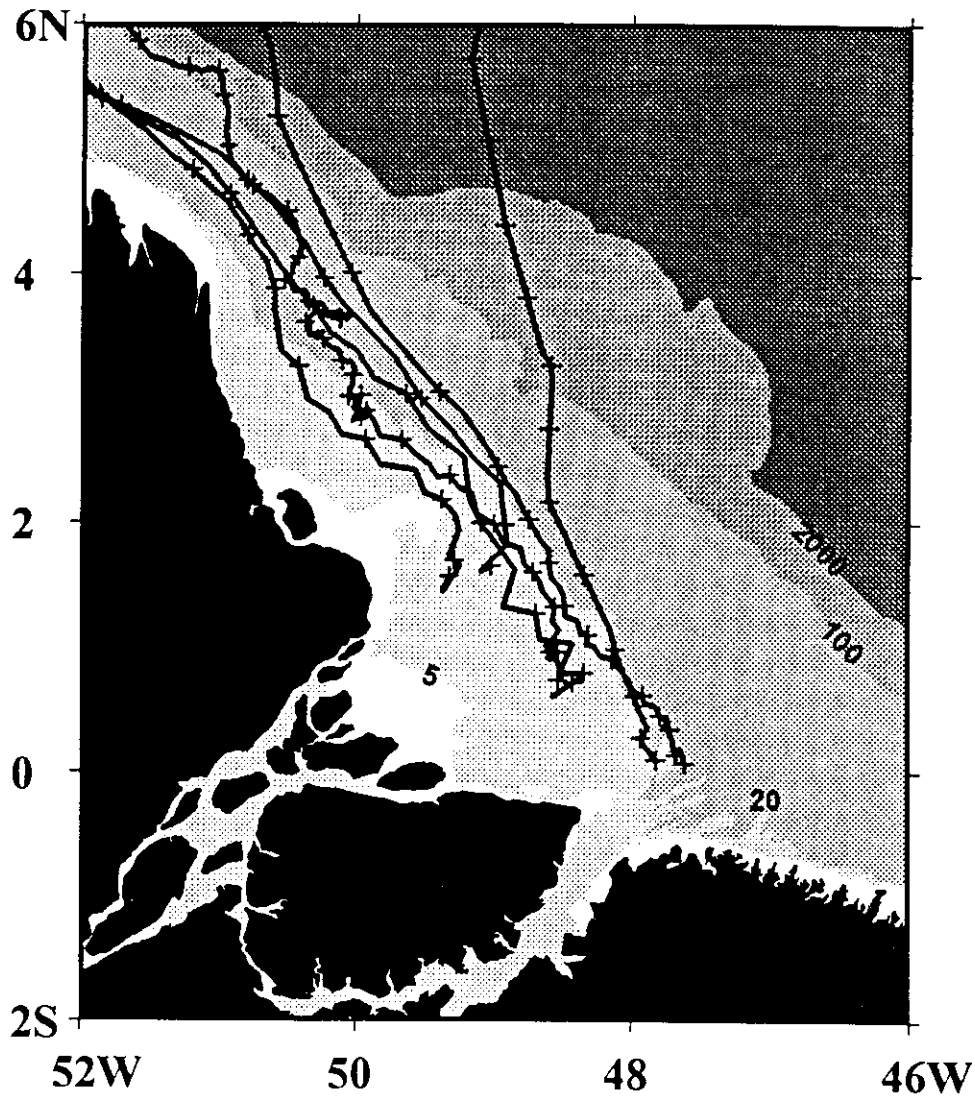

Fig. 16. Trajectories of near-surface drifters (drogues centered at 2.5-m–10-m depth) released in the plume during the four AmasSeds deployment periods (August 1989, March 1990, May 1990 and November 1991). Each 24-h interval is marked by a "+". Average along-shelf velocities were typically 50–100 cm s^{-1}, except during November 1991, when they were 10–25 cm s^{-1}. Bathymetry (in m) is indicated by shading.

The salinity fluctuations at the inner-shelf site are also influenced by along- and cross-shelf advection, but there appears to be an additional contribution due to tide-induced mixing. The large fluctuations occurring around 27 March 1990 and the subsequent increase in tidally averaged salinity appear to result from enhanced vertical mixing during a transition to strong spring tides. The influence of tide-induced mixing at the inner-shelf site is a consequence of its shallow depth (18-m) and its proximity to the frontal zone. Vertical mixing significantly influences the salinity of the plume as it progresses over the shelf, as indicated by the analysis of Lentz and Limeburner (1995). However, it was not determined whether mixing occurs principally at the landward edge of the plume by tidal processes, or whether it occurs throughout the plume due to shear instability or wind mixing. The gradient Richardson numbers at the base of the plume were generally too high to account for local mixing, but the influences of wind stress and waves were not examined.

The moored measurements provide a crude estimate of the freshwater transport along

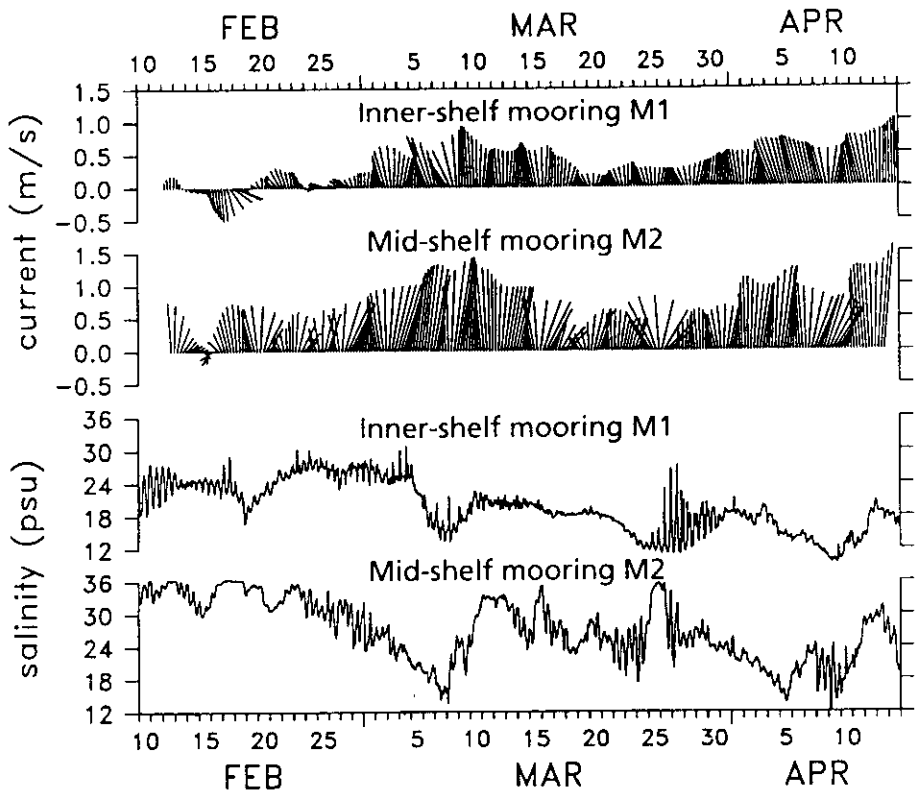

Fig. 17. Time series of current vectors and salinities measured at 3-m depth for the inner- and mid-shelf mooring sites, in water depths of 17 and 61 m, respectively (Geyer *et al.*, 1991; with permission of The Oceanography Society). The current time series are plotted with the along-shelf (northwestward) direction vertical and have been low-pass filtered to remove tidal fluctuations. Note the large amount of current and salinity variability at time scales of days to weeks.

the shelf, based on the assumption that velocity and salinity vary smoothly across the shelf (Lentz and Limeburner, 1995). The results of this analysis (Fig. 18) show that, on average, the freshwater flux at the moored-array transect was comparable to the river discharge over the measurement period. However, there were large variations in the freshwater flux at the moored array on time scales of days to weeks that were not evident in the river discharge. Based on mass conservation, differences between the freshwater flux at the mooring line and the river discharge must result in changes of the freshwater content over the shelf. When freshwater flux at the mooring line reversed during the latter part of February 1990, the resulting convergence of freshwater flux resulted in a large accumulation of low-salinity water over the shelf. This large pool of low-salinity water was observed during the March 1990 survey (Fig. 14), which indicated lower salinities than the high-discharge survey in May–June 1990. The spatial pattern of the freshwater pool was distorted by the temporal changes in the along-shelf flow during the survey, which started on 28 February and ended on 7 March 1990. The along-shelf transport was re-established during this interval (Fig. 18), so the "blob" of low-salinity water was observed as a tongue extending northwestward along the shelf, as the survey progressed northwestward.

Dynamics of the plume. The along-shelf component of wind stress is highly variable (Fig. 2) and although it is small (<1 dyn cm^{-2}), Lentz (1995a) found that it plays a dominent role in the observed fluctuations of the along-shelf motion of the plume. Lentz showed that the

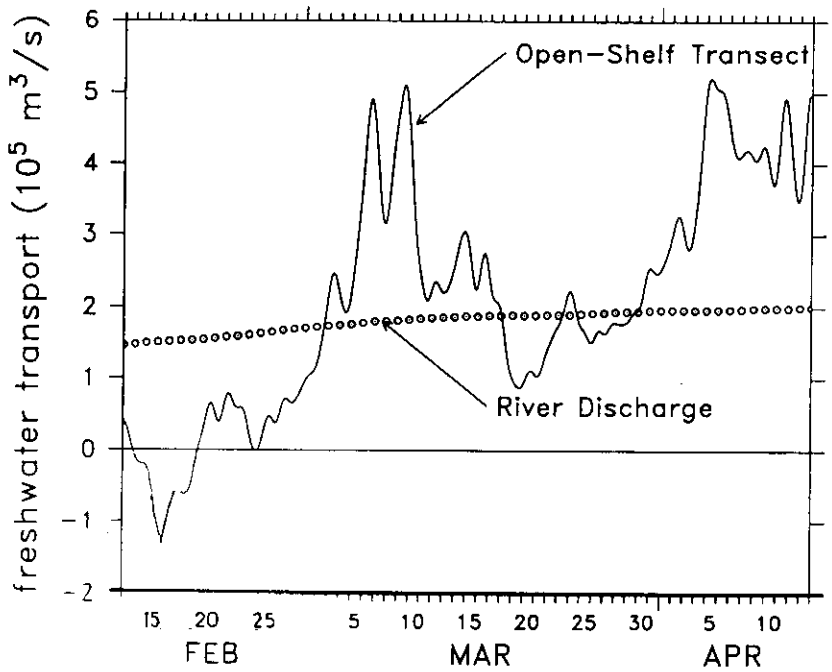

Fig. 18. Estimate of the freshwater transport on the Amazon shelf based on the 3-m data from the inner-shelf and mid-shelf moorings, compared with the estimated river discharge at Obidos (Lentz and Limeburner, 1995; reproduced with permission of the American Geophysical Union). Although the average shelf transport is comparable to the river discharge, the variations are larger than the mean.

along-plume momentum balance at the Open-Shelf Transect is well represented by a simple model that includes only time dependence, wind stress and linearized interfacial friction. Using a value $r = 0.002$ cm s^{-1} as the best-fit for the interfacial friction fractor, the predicted along-shelf velocity agrees well with the observed velocity (Fig. 19); the correlation coefficient between the model and observed along-shelf velocities is 0.77 at the M2 (mid-shelf) site and 0.80 at the M1 (inner-shelf) site. The model not only captures much of the subtidal variability, but also reproduces the observed trend, suggesting that the along-shelf wind stress may be an important factor influencing the plume on monthly and longer time scales. The data/model comparison indicates that in the absence of along-shelf wind stress, there would be a net along-shelf plume flow of 83 cm s^{-1} at the mid-shelf site and 46 cm s^{-1} at the inner-shelf site. This indicates that there is some force other than the local wind stress causing the Amazon plume to flow northwestward.

Observations of the flow beneath the plume indicate a persistent northwestward transport, with a mean of 46 cm s^{-1} at 32-m depth and 11 cm s^{-1} at 62-m depth for the M2 site. This suggests the presence of a mean along-shelf pressure gradient, which drives the flow against the retarding influence of bottom friction. This pressure gradient must be nearly barotropic, because along-shelf density gradients beneath the plume are weak. Thus, the mean sea-surface elevation should slope down toward the northwest. The large shear between the surface plume and the underlying water is explained by the relatively weaker interfacial drag coefficient, in comparison to the bottom drag coefficient. A frictionally driven flow would not normally be expected in water depths of 60 m, but this occurs on the Amazon shelf due to the greatly reduced influence of the Earth's rotation, which allows the influence of bottom friction to extend through the water column. The along-shelf flow is slower at the inner-shelf site, presumably due to the increased influence

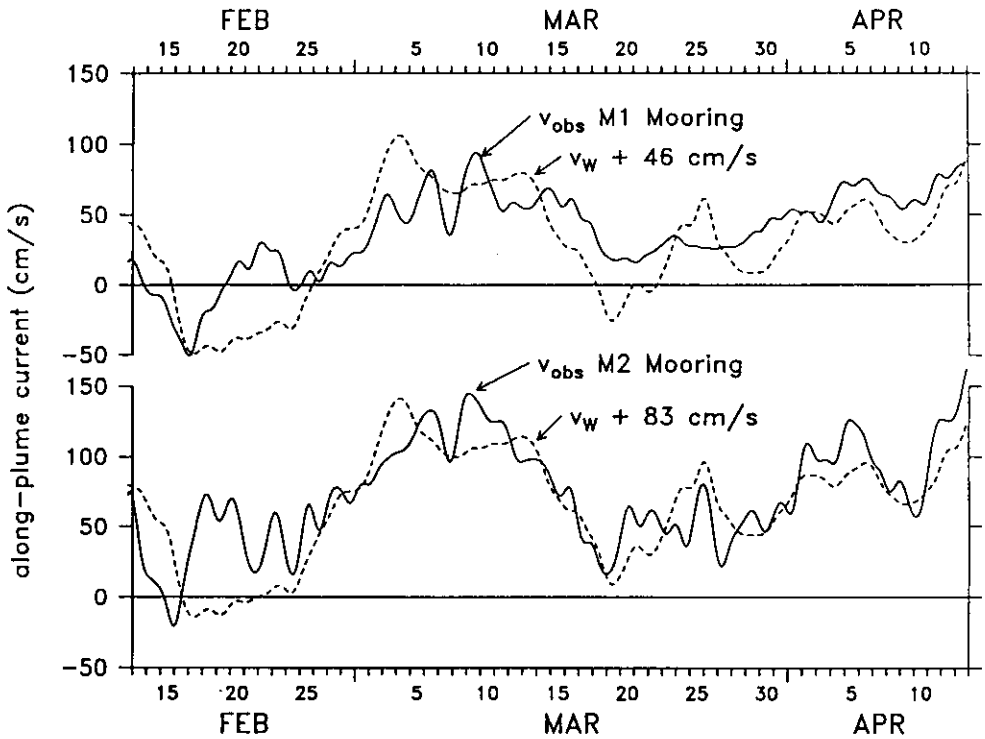

Fig. 19. Comparison of low-pass-filtered along-plume current observations (3-m depth) and the estimated wind-driven along-plume current at the inner- and mid-shelf sites, using a simple momentum balance and the ECMWF winds. Offsets of 46 and 83 cm s^{-1} have been added to the wind-driven current estimates for M1 and M2, respectively. The correlation coefficients between observed and estimated currents are 0.77 for the M2 mooring and 0.80 for the M1 mooring. The drag coefficient used is $r = 0.002$ cm s^{-1}. (From Lentz, 1995a; reproduced with permission of the American Geophysical Union.)

of bottom friction at that site. The origin of the pressure gradient is unknown; it appears to influence the entire Amazon shelf, and it is likely to be associated with the dynamics of the North Brazil Current.

The cross-shelf dynamics of the plume provide an interesting contrast to mid-latitude settings, due to the relatively diminished role of Coriolis acceleration in the Amazon plume. Lentz (1995a) found that time-dependence, baroclinic pressure gradient, wind stress and Coriolis acceleration of the along-shelf flow are all important in the cross-shelf momentum balance at the Open-Shelf Transect. Unlike most mid-latitude river plumes, in which the influence of Coriolis acceleration is usually strong enough to make river plumes turn anti-cyclonically (i.e. to the right in the northern hemisphere), the Amazon plume turns cyclonically (to the left), due to the small value of the Coriolis parameter and the persistence of cross-shelf wind-forcing and the northwestward along-shelf flow. The vertical shear in the along-shelf flow and the cross-shelf density gradient do not tend toward the geostrophic or "thermal wind" balance typical of mid-latitude density fronts; in fact, the geostrophic balance would require a reversal of the vertical shear in the Amazon plume. However, the landward wind stress is large enough to compensate for this imbalance and to maintain the northwestward transport in the plume, in spite of the tendency of rotation to direct the plume seaward.

Lentz (1995a) explained the observed fluctuations in the width of the plume (Fig. 15) based on changes in wind stress and of the Coriolis force, the latter of which is proportional to the strength of the along-shelf flow. When the cross-shelf winds are strong and the

along-shelf flow is weak, the plume becomes narrow (e.g. 10 February 1990) and, conversely, as the cross-shelf winds weaken and the along-shelf flow increases, the plume expands seaward (e.g. 4 March 1990). Lentz (1995a) noted that these dynamics suggest a positive feedback process affecting the along-shelf transport. As the along-shelf flow increases, it broadens the plume and thus further increases the along-shelf transport. Conversely, weak along-shelf flow causes the plume to collapse and further reduces along-shelf transport. This positive feedback may amplify the fluctuations of along-shelf transport of plume water that occur as a result of the variations in wind-forcing.

The amplification of variations in along-shelf transport helps explain the large amount of variability observed in the freshwater content over the shelf. A cartoon of the changes in structure of the plume during different discharge conditions is shown in Fig. 20. When the wind stress is normal to the coast ("intermediate" conditions) the northwestward transport at the Open-Shelf Transect balances the riverine input. The plume roughly parallels the coast. When the wind comes from a more northerly direction ("slow" conditions), as is observed intermittently during the peak of the northeast trades in February and March (Fig. 2), the transport at the Open-Shelf Transect is reduced. The Coriolis acceleration no longer balances the wind stress, so the plume collapses in the transverse direction. The along-shelf transport is reduced essentially to zero and the fresh water starts to accumulate in front of the river mouth. If this condition persists for a week, the freshwater content on the shelf will double. Conversely, if the wind comes from a more southerly direction ("fast" conditions), as during August, the along-shelf wind stress accelerates the plume at the Open-Shelf Transect. The increased offshore Coriolis acceleration causes the plume to broaden, which further increases the along-shelf flux. The increased freshwater transport at the Open-Shelf Transect exceeds the supply from the river and the plume collapses in front of the river mouth.

Based on the shipboard wind data, the four hydrographic surveys (Fig. 14) can be categorized in terms of the three cases shown in Fig. 20. Interestingly, none of the surveys correspond to the "intermediate" conditions. The March 1990 survey catches a transition from "slow" to "fast" conditions, based on the wind forcing. The large bulge at the river mouth during the March survey is explained by a long interval of down-coast winds, which cause fresh water to accumulate at the mouth. However, the wind switched during the survey and the conditions farther to the northwest are characteristic of "fast" plume conditions, with a broad plume of low-salinity water extending across the shelf. The wind data for the other three surveys indicate varying amplitudes of "fast" plume conditions, with the strongest along-shelf winds occurring during the August 1989 survey. The spatial pattern of salinity during August indicates a broadening plume in the vicinity of the Open-Shelf Transect and there is the suggestion of plume collapse in front of the river mouth.

A tongue of low-salinity water was observed during all four large-scale surveys, roughly extending from the tip of the Cabo Norte shoal. The tongue follows a similar trajectory during the first three surveys and it is roughly 50 km closer to shore during the low-discharge survey in November 1991. The location of the tongue relative to the shoal suggests that the maximum freshwater transport is displaced offshore by the presence of the shoal. Frictional effects would be expected to dominate in the shallow waters over the shoal, thus significantly reducing the magnitude of the along-shelf flow in this area. Although no measurements were made over the shoal, mixing by waves and tidal currents probably results in well-mixed conditions. This contrasts the strongly stratified conditions in the plume, in which turbulent mixing is partially suppressed by the stratification. Given

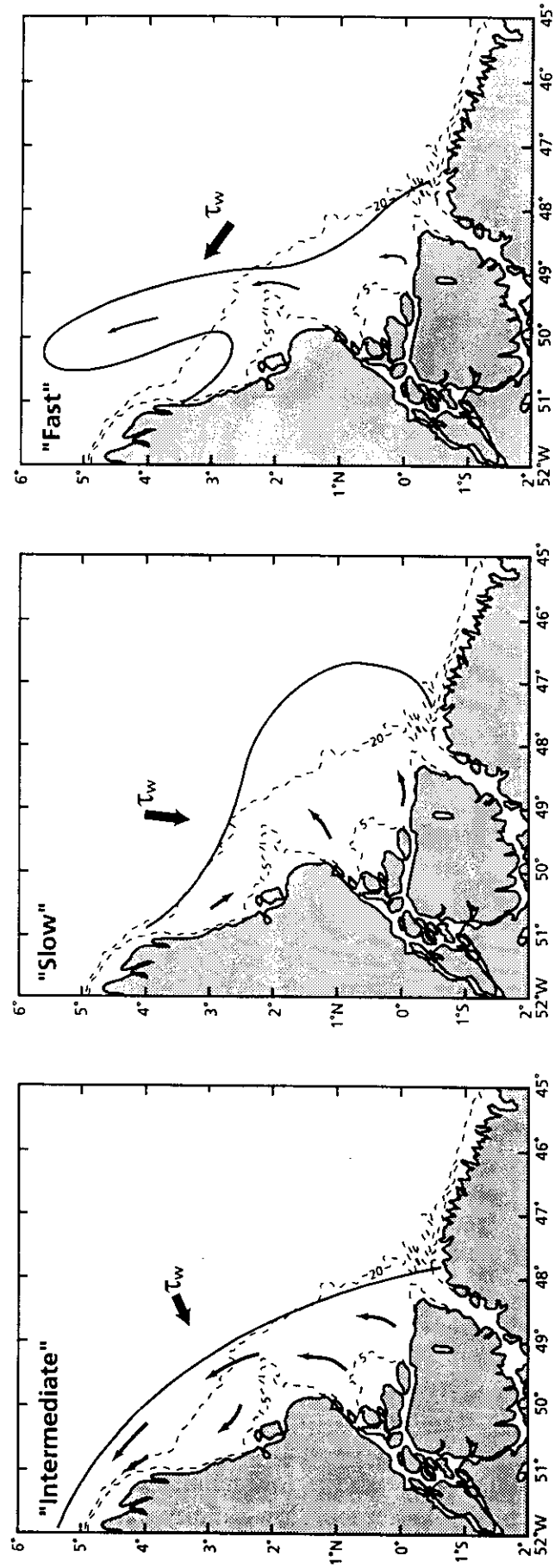

Fig. 20. Schematic of the plume structure during different wind conditions. The near-surface currents and wind stress are shown as thin and thick arrows, respectively. In "intermediate" conditions (left panel), the wind stress is oriented normal to the shelf. In the cross-plume balance, the baroclinic pressure gradient and Coriolis acceleration are balanced by wind stress. In the along-shelf balance, the along-shelf pressure gradient is balanced by bottom friction. In "slow" conditions (center), an adverse along-shelf wind causes the plume to be trapped near the river mouth, where it bulges seaward. In "fast" conditions (right), the influence of favorable along-shelf wind stress on the plume structure is shown. The plume speeds up and the additional contribution of Coriolis acceleration causes it to diverge from the coast.

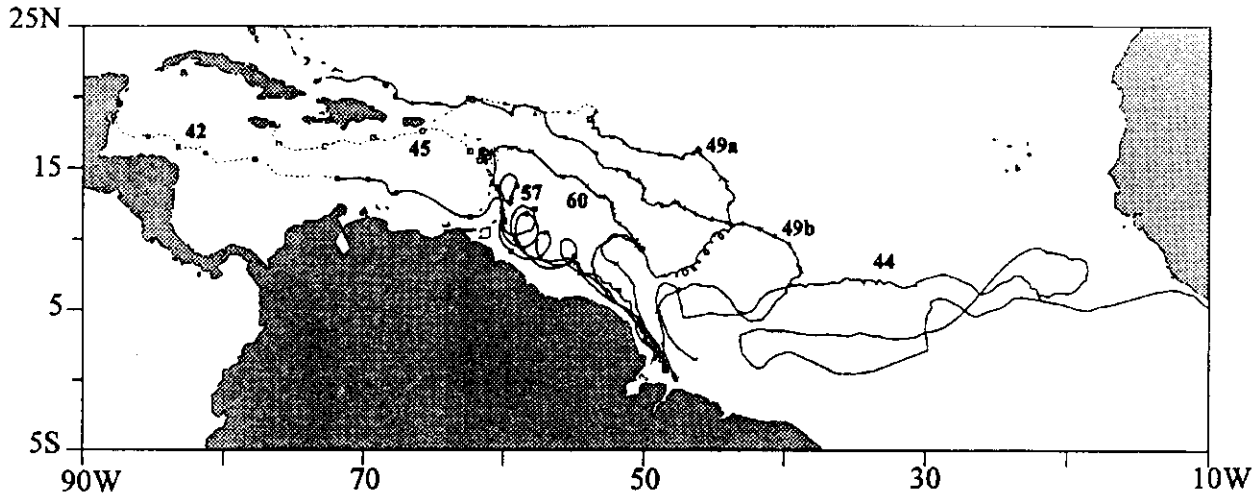

Fig. 21. Trajectories of six satellite-tracked drifters, launched near the mouth of the Amazon River at different stages of the river discharge cycle and one launched in the core of the NBC. The numbers are drifter ID numbers. Drifters 49a and 60 were deployed in August 1989; 45 and 57 in March 1990; 44 in June 1990; 42 and 49b in November 1991. Different symbols identify different drifters and the symbols are plotted every 10 days along each trajectory. A dashed trajectory is shown when a drifter lost its drogue.

the same magnitude of along-shelf forcing, the flow over the shoal should be considerably weaker than the flow farther seaward in the stratified plume. This cross-shelf variation in flow could produce the observed tongue-like pattern advecting low-salinity water. Gibbs (1976) suggested that upwelling of high-salinity water landward of the plume axis may also contribute to the tongue-like structure. The AmasSeds observations also indicate that upwelling may be significant, based on velocity and temperature data (see section on the outer shelf).

The far field

The far-field trajectories of the drifters demonstrate the seasonal variability of the retroflection of the North Brazil Current. Three drifters (two deployed in March 1990 and one deployed in November 1990) went northwestward toward the Carribbean, parallel to the northeastern coast of South America (Fig. 21). These drifter tracks show the distinctive signature of eddies starting downstream of the Demerara Rise (a submarine ridge extending northward from the coast of South America at 54°W), with looping periods of approximately 11 days. The rest of the drifters (two drifters deployed in August 1989, one drifter deployed in June 1990 and one drifter deployed in November 1991) turned away from the coast somewhere between 5° and 10°N, apparently as a result of the NBC retroflection. Three of these drifters eventually went northwestward toward the Windward Islands; one continued nearly to Africa in the North Equatorial Counter Current.

The variation of the drifter trajectories between deployments is consistent with the seasonal variation in the near-surface salinity distribution, determined from analysis of historical hydrographic observations in the NODC data archive (Lentz, 1995b). The mean near-surface salinity field for January–July shows low-salinity water extending northwestward along the coast, whilst in July–December, low-salinity water extends northeastward in the NBC retroflection (Fig. 22; see also Muller-Karger *et al.*, 1988).

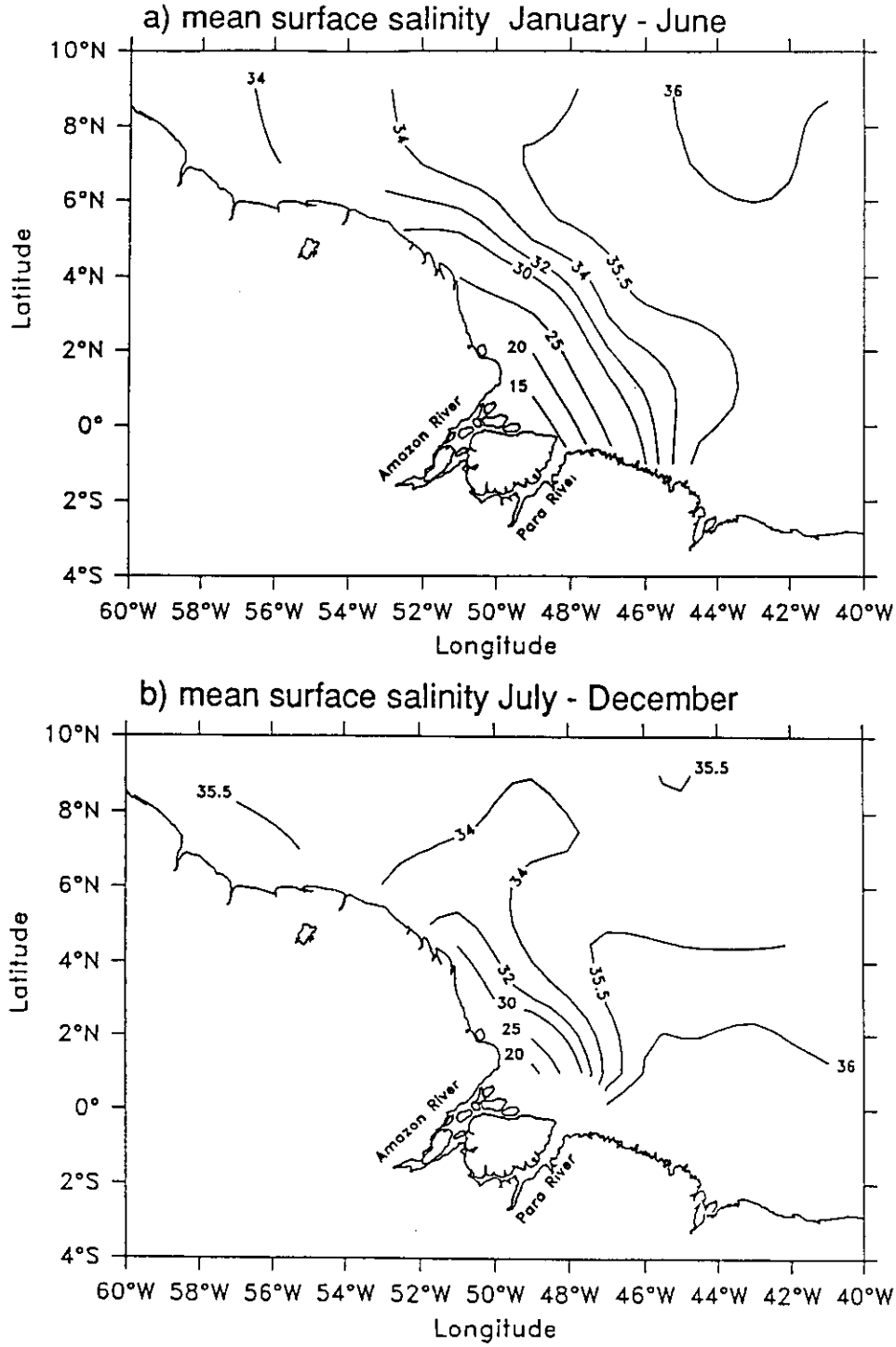

Fig. 22. Mean near-surface salinity based on historical data from NODC during January–June (a) and July–December (b). There is a shift in the far-field salinity distribution between the two periods, due to the variation of the NBC retroflection as well as variation in the along-shelf wind stress. During the January–June period, episodes of southward wind stress lead to an eastward bulging of the isohalines near the equator.

THE OUTER SHELF

The currents over the outer-shelf are northwestward, with speeds exceeding 100 cm s^{-1}. Figure 23 compares the velocities observed at 30-m depth for the AmasSeds M3 site on the

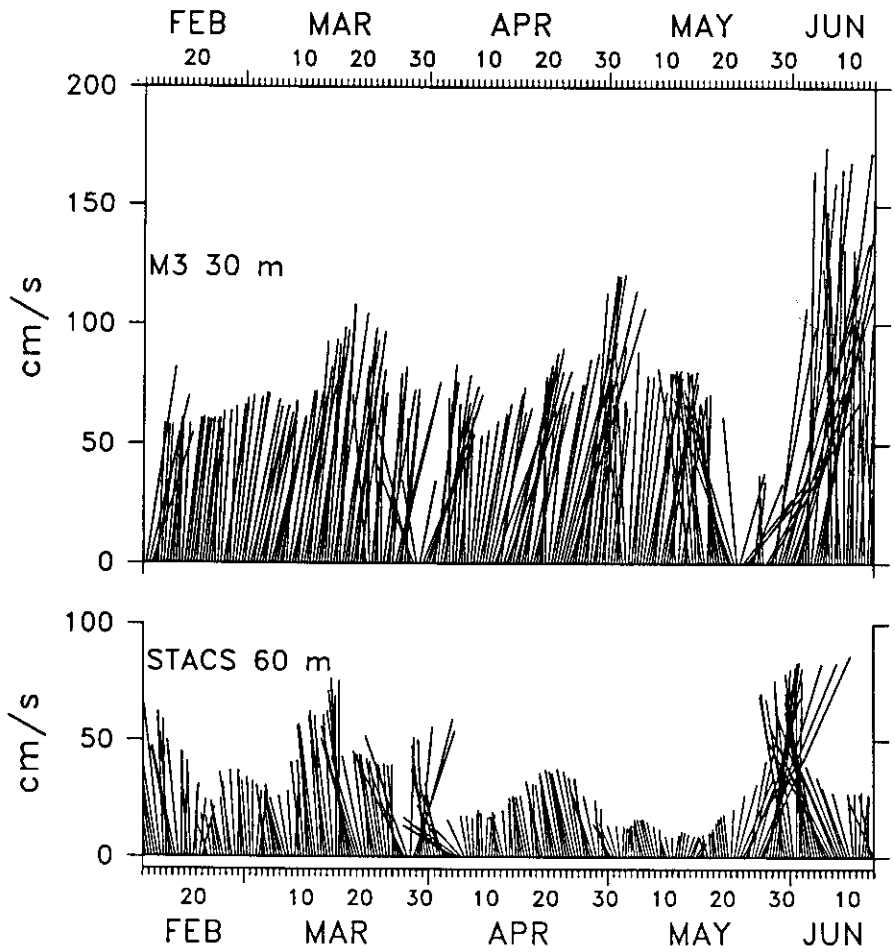

Fig. 23. Vector velocities for the outer-shelf M3 mooring at 30-m depth and the STACS mooring near the 483-m isobath at 60-m depth. The vectors have been rotated such that the along-shelf direction (315°) is upward. There is a visual correspondence of variations between the two locations, but the correlation is low.

105-m isobath, with the flow at 60-m depth for the STACS mooring on the 483-m isobath. During this period, the along-shelf currents over the outer shelf were considerably stronger than those farther seaward, although some of this difference may be due to the depth of the two current measurements. The correlation is weak between the currents at the two locations. Correlations are also weak between the sub-plume currents at the M2 mid-shelf site and those at the M3 outer shelf site. The spatial variability and lack of correlation among the current measurements on the outer shelf and the upper slope suggest a complex flow field, perhaps resulting from meanders and eddies in the NBC. The persistence and strength of the along-shelf flow on the outer shelf supports the notion that the NBC extends onto the shelf, at least during the period of the moored observations.

The STACS current time series indicate that the flow within the NBC reached a minimum between February and June (the period of AmasSeds moored measurements) and reached a maximum between August and November (Fig. 2). The shipboard observations of currents on the outer shelf during AmasSeds do not reflect this seasonal variation. Along-shelf currents were found to be stronger during February–March and June 1990 than in November 1991, when weak northwestward and occasionally southeastward currents were observed. These observations may not reflect seasonal variations, but may in fact reflect shorter-term variations of the NBC. Alternatively, they may be due

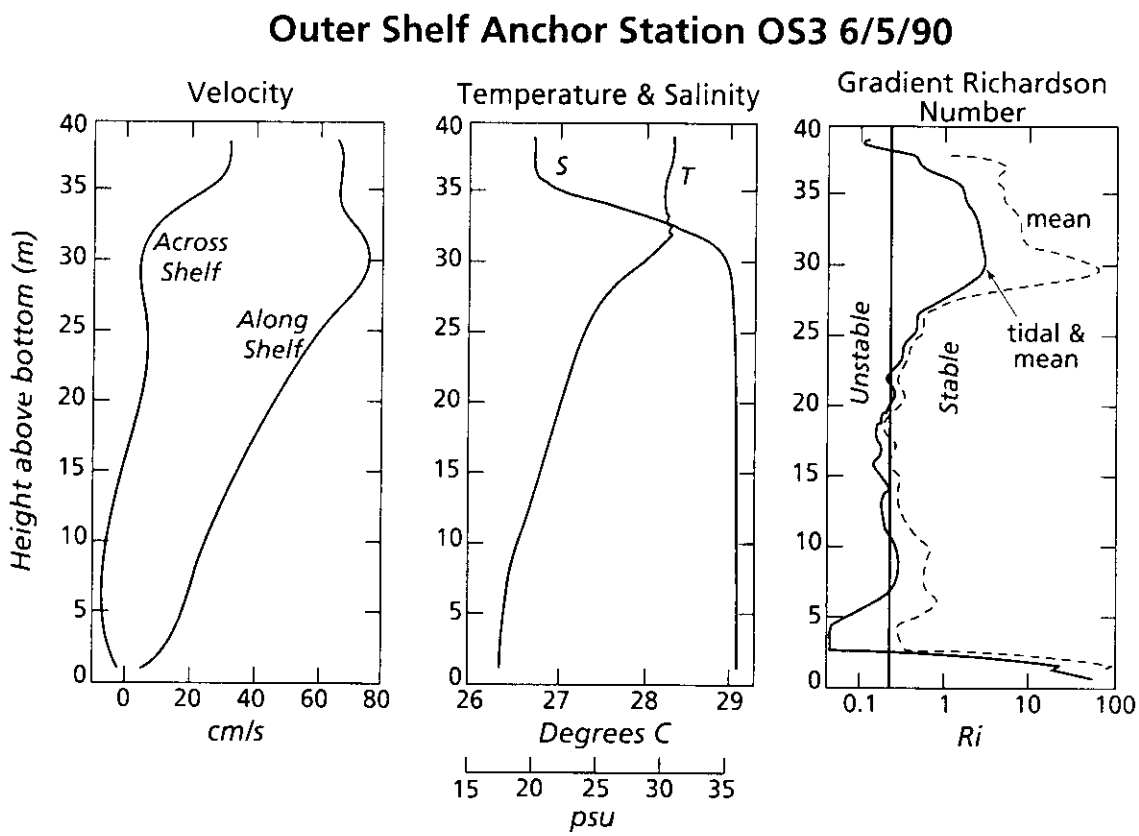

Fig. 24. Vertical profiles of tidally averaged velocity, salinity and gradient Richardson number (based on hourly and tidally averaged quantities) at the Outer-Shelf anchor station OS3 during June 1990. A striking feature of the profiles is the broad, stratified shear layer extending from near the bottom to within 10 m of the water surface, in which $Ri \approx 0.25$. High values of Ri near the bottom are due to stratification by suspended sediment. Upwelling is evident in the cross-shelf velocity.

to seasonal variations in the landward extent of the NBC, although there is no other evidence in the AmasSeds observations of such variations.

Observations at the OS3 anchor station (Fig. 24) illustrate the vertical structure of the flow and water properties beneath the plume. This station at the 40-m isobath was just landward of the broad, gently sloping outer shelf, but the water properties beneath the near-surface plume were similar to those throughout the outer-shelf region. Below 10-m depth, the salinity was uniformly 36.2 psu, virtually the same as NBC water. The along-shelf velocity was strongly sheared across this layer of uniform salinity, increasing from less than 10 cm s^{-1} near the bottom to almost 80 cm s^{-1} at the base of the plume. This strong shear was not associated with the plume, being located in the uniformly high-salinity water. Although there was no salinity gradient in the waters beneath the plume, the temperature gradient was strong enough to influence the stability of the shear flow. Estimates of gradient Richardson number indicate that the flow through most of the shear zone was very close to the theoretical stability threshold of 0.25. A similar result is obtained by calculating Ri from the moored observations at the mid-shelf site M2. The shear and temperature stratification between 30 and 54 m depth lead to near-critical Richardson numbers ($Ri = 0.25 \pm 50\%$) for more than half of the 60-day record (Fig. 25). Thus, marginal stability was a persistent characteristic of the outer-shelf flow.

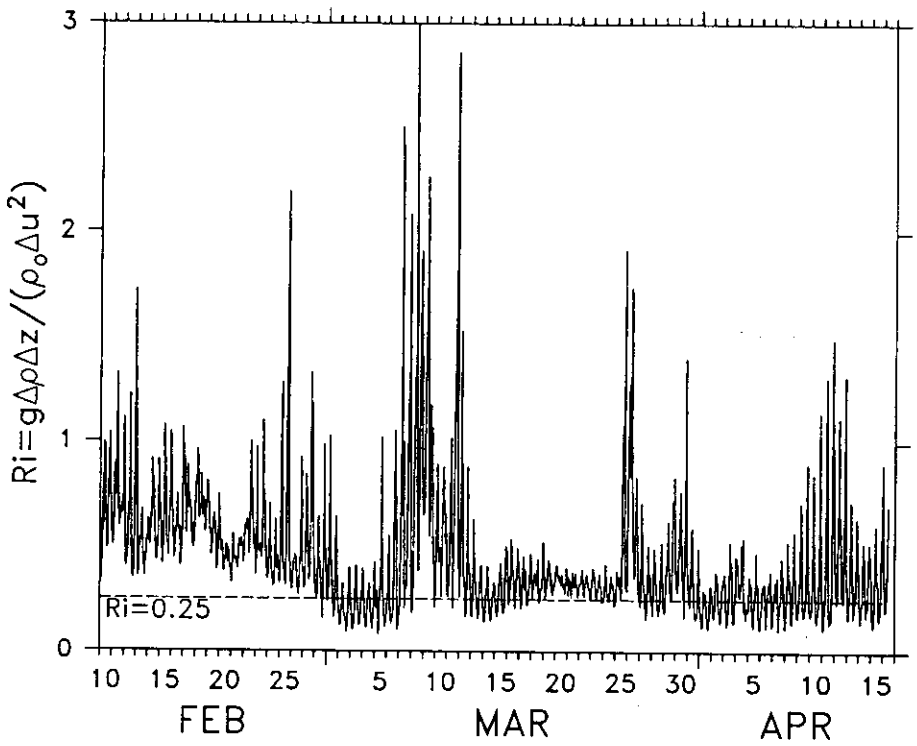

Fig. 25. Gradient Richardson number *Ri* calculated between 30- and 54-m depth at the mid-shelf M2 mooring. During a large fraction of the record $Ri \approx 0.25$, indicating marginally stable conditions.

The uniform distribution of *Ri* at its critical value is characteristic of stratified boundary-layer flows (e.g. Businger *et al.*, 1971; Trowbridge, 1992). The flow is apparently driven by a barotropic pressure gradient, as noted previously in connection with the northwestward motion of the plume. Based on the distribution of *Ri*, the boundary layer extends nearly to the base of the plume (Fig. 24). This is considerably broader than the tidal boundary layer, which is approximately 10-m thick (based on moored measurements at the mid-shelf site; Beardsley *et al.*, 1995). The vertical extent of the tidal boundary layer is limited by the stratification, as well as the tidal frequency (Soulsby, 1990), whereas the boundary layer of the mean along-shelf flow is influenced by stratification, but not by time-dependence. The Earth's rotation does not constrain the vertical growth of the boundary layer at this latitude, due to the small value of the Coriolis parameter ($f = 1 \times 10^{-5}\,s^{-1}$). However, the Coriolis acceleration still results in Ekman veering within the boundary layer, which causes a landward component of flow at the bottom. The anchor-station observations (Fig. 24) indicate a net landward motion near the bottom, consistent with Ekman veering. The moored measurements at M2 also show a significant cross-shelf circulation in the mean, with landward flow of 3–6 cm s^{-1} between 30- and 60-m depth, and seaward flow of 7 cm s^{-1} at 3-m depth (Lentz, 1995a). This cross-shelf transport is due to the imbalance between the barotropic component of cross-shelf pressure gradient on the outer shelf and the vertically varying Coriolis acceleration of the strongly sheared along-shelf flow (e.g. Kalkwijk and Booij, 1986).

A consequence of the landward near-bottom flow on the outer shelf is the upwelling of relatively cold water from offshore. Gibbs (1970) attributed the upwelling to along-shelf wind stress; these observations and the above discussion suggest that the upwelling may be

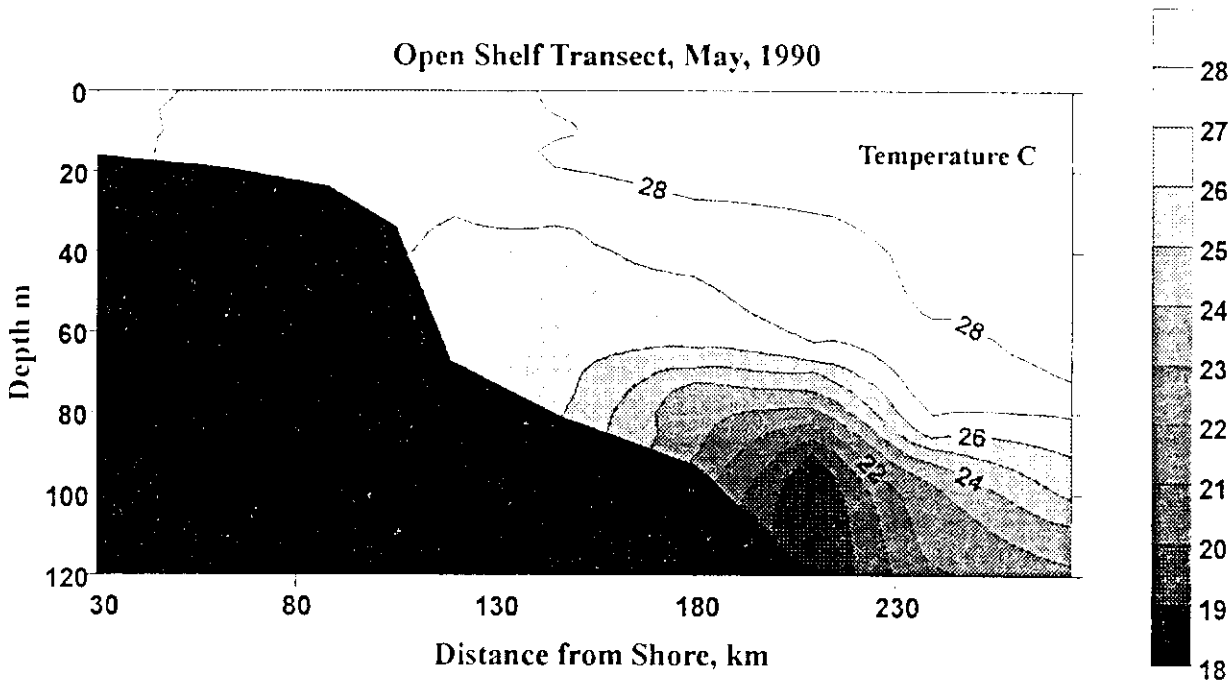

Fig. 26. Cross-section of temperature along the Open-Shelf Transect obtained during the May 1990 shelf-wide survey. Upwelling is evident in the upward-sloping isotherms and the inferred onshelf motion of cool water along the bottom, beneath the thermocline. A cold anomaly of this type was observed during all four cruises.

driven by Ekman transport of the along-shelf flow. Figure 26 shows a tongue of cold water extending onto the shelf from the shelf break along the Open-Shelf Transect, during May 1990. The near-bottom temperature data at the M2 mooring also show cooling events that are correlated with the on-shelf flow, consistent with an upwelling scenario. The mean landward transport of bottom water results in net cooling; this tendency must be balanced in the mean by along-shelf advection and/or vertical mixing. Rough estimates of vertical mixing, based on an assumed mixing efficiency of 0.15 (Osborn, 1980) and stress estimates from Cacchione *et al.* (1995) and Beardsley *et al.* (1995), suggest that the downward heat flux due to mixing could be comparable to the cross-shelf advective flux in the near-bottom water. The vertical mixing does not appear to extend into the plume, however, based on the lack of salinity variation in the sub-plume waters. The combination of upwelling and mixing results in cooling of the water beneath the plume as it flows along the shelf. There was a drop in temperature of 1–2°C for the sub-plume waters between the River-Mouth and Open-Shelf Transects, during the August 1989, May 1990 and November 1991 surveys. Based on an along-shelf advective velocity of 0.8 m s^{-1}, along-shelf advective cooling is commensurate with the net heat loss due to vertical mixing and upwelling of cold water. This vertical transport of oceanic water also supplies nutrients to the upper water column, contributing to high rates of phytoplankton production (DeMaster *et al.*, 1996).

CONCLUSIONS AND UNRESOLVED QUESTIONS

The physical oceanographic component of AmasSeds provides the most comprehensive examination to date of the physical processes on the Amazon shelf. A combination of

strong tidal currents, large riverine outflow, persistent winds and large-scale forcing of along-shelf flow, leads to an energetic and surprisingly variable physical regime. The strong semi-diurnal tidal currents are explained in terms of the near-resonant conditions of the broad, shallow shelf. The tidal propagation characteristics change from a standing wave at the Open-Shelf Transect, to a progressive wave at the River-Mouth Transect. The tides strongly influence the structure and position of the frontal zone, due to the influence of tide-induced mixing on stratification and cross-shelf salinity variation. During neap tides, the frontal zone is strongly stratified and extends up to 20 km landward of its mean position. In contrast, during spring tides the vertical stratification is reduced and the front moves seaward. Based on estimates of gradient Richardson numbers, these variations in frontal-zone structure appear to result from shear-induced mixing. Thick layers of fluid mud are associated with the frontal zone, due to the effective trapping of river-derived sediment in the frontal convergence zone. The fluid mud is of such high concentration that it significantly increases stratification in the near-bottom water, which leads to a reduction of turbulent mixing in the bottom boundary layer. The vertical structure of the tidal flow suggests that the effective drag coefficient is reduced by up to an order of magnitude relative to normal continental-shelf environments.

The Amazon plume, which extends over much of the shelf to the northwest of the river mouth with a typical thickness of 5–10 m, shows a large amount of variation in salinity and seaward extent, on time scales ranging from a few days to seasonal. Along-shelf wind stress causes a large fraction of the observed plume variability, both in terms of transport and spatial structure. When the along-shelf wind stress is northwestward, the transport of the plume increases and the plume veers seaward as it extends along the shelf. When the along-shelf wind stress opposes the northwestward drift of the plume, its along-shelf transport is retarded and fresh water accumulates seaward of the river mouth. Increased residence time gives plankton time to grow, consuming nutrients and increasing their biomass within the plume (DeMaster *et al.*, 1996). In addition to wind-induced plume motion, there appears to be a northwestward mean transport of the plume, driven by a large-scale pressure gradient on the shelf. This pressure gradient also drives a strongly sheared, along-shelf flow beneath and seaward of the plume, over the outer shelf. The flow is a landward extension of the North Brazil Current. The bottom Ekman transport associated with the along-shelf flow on the outer shelf, advects relatively cold water landward from the shelf break across the outer- and mid-shelf regions.

There are a number of important questions left unanswered after this study, due in part to limitations of the study and to the size and complexity of the Amazon shelf.

The dynamics of the river-mouth and inner-shelf regions

Few observations of water properties and currents were obtained in the nearshore regions of the Amazon shelf during AmasSeds, nor have previous studies provided adequate physical oceanographic measurements in these regions, in part because of hazardous navigation conditions. There remain significant questions about the strength and variability of the along-shelf flow on the inner shelf and thus about its contribution to the along-shelf flux of fresh water and sediment. Satellite imagery (Fig. 8) suggests that the riverine outflow may sometimes extend directly over the Cabo Norte shoal, but the evidence is very limited. One would expect that the well-mixed and energetic conditions on the inner shelf would lead to high drag and thus weak along-shelf flow, particularly on

the Cabo Norte shoal, but we cannot rule out the inner shelf as a potentially important conduit of fresh water and/or sediment. Allison *et al.* (1995) (see also Kuehl *et al.*, 1996) found that nearshore transport of Amazon sediments is contributing to the progradation of the shoreline near Cabo Cassiporé. The mechanisms by which that sediment is transported to shore are not well understood.

Physical controls on sediment transport

The observations of extensive fluid mud layers on the Amazon shelf by Kineke and Sternberg (1995) and the insights about trapping and transport mechanisms described in Kineke *et al.* (1996) significantly advance our understanding of the sediment transport. However, there remain a number of unresolved issues about the mechanisms of sediment transport, particularly the along-shelf transport and the feedback between sediment transport and the flow. Kineke *et al.* (1996) discuss the mechanisms of trapping in the frontal zone, showing a strong similarity to the trapping processes occurring in estuarine turbidity maxima. They also indicate that gravity-driven, cross-shelf flow may provide the required cross-shelf tranport to carry sediment from the frontal zone to the foreset beds farther seaward, where most of the accumulation occurs (Kuehl *et al.*, 1986, 1996). However, it is not clear how sediment is transported from the river mouth to the larger reservoir of fluid muds near the Open-Shelf Transect. The Cabo Norte shoal is likely to limit the northwestward advection of fluid mud, due to intense mixing and shallow water depth. The bulk of the sediment may pass over the shoal, although probably not as fluid mud. The along-shelf extent of the sediment deposition is probably coupled to the hydrodynamics, although it is not obvious what mechanisms control this distribution. The accumulation pattern within the foreset beds may be controlled by the distribution of fluid mud within the frontal zone, although other physical factors such as the along-shelf and across-shelf variation of bottom stress may also be important.

Another unresolved issue is the feedback between the suspended sediment and the frontal-zone dynamics. The density anomaly of the fluid mud is great enough to have a strong stabilizing effect on the bottom boundary layer (Trowbridge and Kineke, 1994). It can also influence the baroclinic pressure gradient (Kineke *et al.*, 1996). Thus, the sediment may alter the dynamical balance of the frontal zone, influencing the frontal position and structure and also the sediment trapping within the front. Whether this feedback loop significantly affects the trapping process is an interesting topic for future research. The role of tidal currents in the formation and maintenance of fluid muds is not clear and the possible feedback between the bottom sediments, the tidal regime and bottom stress is unresolved. Finally, the role of surface gravity waves on sediment transport is still uncertain, due in large part to the limited number of wave measurements during AmasSeds. Kuehl *et al.* (1996) provide evidence that there are seasonal variations in resuspension that mix the upper meter of the sediment; these variations may be due to changes in wave energy, although this cannot be confirmed by existing observations.

Mixing processes

Geyer (1995) found much tide-inducing mixing within the frontal zone, but his analysis indicates that a significant fraction of the mixing between fresh and salt water occurs seaward of the frontal zone in the plume. The entrainment estimates of Lentz and

Limeburner (1995) also suggest that mixing occurs at the base of the plume. However, the observed shears across the pycnocline are too small by at least a factor of two (except at the landward and seaward limits of the plume) to destabilize the stratification within the pycnocline, via shear instability. How, when and where this tremendous volume of mixing occurs is still a mystery. Perhaps the accelerating flow around the Cabo Norte shoal plays an important role or perhaps the wind stress provides an efficient mixing mechanism in the vicinity of surface fronts.

The need for three-dimensional modeling

The simple analyses that have been described here do not do justice to the complex, three-dimensional and time-dependent dynamics of the Amazon shelf. Further progress in interpreting the existing data and in planning future field efforts would benefit greatly from three-dimensional model studies. There is enough observational information from AmasSeds, STACS and other work to provide a useful set of constraints and tests of a model's performance, allowing a more quantitative examination of the dynamics than has been attempted thus far. A few model studies have been undertaken (Jewell *et al.*, 1993; Paluszkiewicz, 1993), but they have not fully exploited the AmasSeds data, nor have they investigated in detail the physical processes on the shelf. Questions related to the inner-shelf dynamics, frontal-zone mixing, wind-driven motions and shelf-wide barotropic currents are all amenable to three-dimensional model simulation. Particular attention should be placed on the choice of turbulence closure, due to the strong influence of salt, temperature and sediment stratification on the velocity structure. A modeling approach could also address the complex problem of sediment transport, which would, in addition to the water-column transport, have to deal with vertical exchange between the bed, the fluid-mud layer and the overlying water column, as well as confronting the rheology of fluid muds. Although the data are inadequate to provide a complete set of initial or boundary conditions for three-dimensional model simulations, there is much that could be learned about the fluid and sediment transport processes on the Amazon shelf with a modeling effort that takes full advantage of the available observations.

Acknowledgements—The authors acknowledge the leadership and dedication of Chuck Nittrouer and Dave DeMaster through all stages of AmasSeds. We also thank Gail Kineke and Richard Legeckis for their scientific contributions; Craig Marquette and Carol Allesi for their technical assistance. This work was funded by National Science Foundation Grants OCE-8812917 and OCE-9115712, WHOI contribution number 8800.

REFERENCES

Allison M. A., C. A. Nittrouer and L. E. C. Faria (1995) Rates and mechanisms of shoreline progradation and retreat downdrift of the Amazon River mouth. *Marine Geology*, **125**, 373–392.

AmasSeds Group (1990) A multidisciplinary Amazon shelf sediment study. *American Geophysical Union*, **71**, 1771, 1776–1777.

Baumgartner A. and E. Reichel (1975) *The world water balance*, Elsevier, Amsterdam, 179 pp.

Beardsley R. C., J. Candela, R. Limeburner, W. R. Geyer, S. J. Lentz, B. M. Castro, D. Cacchione and N. Carneiro (1995) The M_2 tide on the Amazon shelf. *Journal of Geophysical Research*, **100**, 2283–2319.

Businger J. A., J. C. Wyngaard, Y. Izumi and E. F. Bradley (1971) Flux-profile relationships in the atmospheric surface layer. *Journal of Atmospheric Science*, **28**, 181–189.

Cacchione D. A., D. E. Drake, R. W. Kayen, R. W. Sternberg, G. C. Kineke and G. B. Tate (1995) Measurements in the bottom boundary layer on the Amazon subaqueous delta. *Marine Geology*, **125**, 235–257.

Candela J., R. C. Beardsley and R. Limeburner (1992) Separation of tidal and subtidal currents in ship-mounted acoustic Doppler current profiles observations. *Journal of Geophysical Research*, **97**, 769–788.

Cartwright D. E., R. D. Ray and B. V. Sanchez (1991) Oceanic tide maps and spherical marmonic coefficients from Geosat altimetry. *NASA Technical Memorandum* 104544, Goddard Space Flight Center, Greenbelt, MD, 75 pp.

Curtin T. B. (1986a) Physical observations of the plume region of the Amazon River during peak discharge. II. Water masses. *Continental Shelf Research*, **6**, 53–71.

Curtin T. B. (1986b) Physical observations of the plume region of the Amazon River during peak discharge. III. Currents. *Continental Shelf Research*, **6**, 73–86.

Curtin T. B. and R. V. Legeckis (1986) Physical observations in the plume region of the Amazon River during peak discharge. I. Surface variability. *Continental Shelf Research*, **6**, 31–51.

Damuth J. E. and N. Kumar (1975) Amazon cone: morphology, sediments, age and growth pattern. *GSA Bulletin*, **86**, 863–878.

Defant A. (1961) *Physical oceanography*, Pergamon Press, Oxford, 598 pp.

DeMaster D. J., W. O. Smith, D. M. Nelson and J. Y. Aller (1996) Biogeochemical processes in Amazon shelf waters: chemical distributions and uptake rates of silicon, carbon and nitrogen. *Continental Shelf Research*, **16**, 617–643.

Ferraz L. and A'd Carvalho (1975) Tidal and current prediction for the Amazon's North Channel using a hydrodynamical-numerical model. M.S. thesis, Naval Post-graduate School, Monterey, CA, 85 pp.

Geyer W. R. (1995) Tide-induced mixing in the Amazon frontal zone. *Journal of Geophysical Research*, **100**, 2341–2353.

Geyer W. R., R. C. Beardsley, J. Candela, B. M. Castro, R. V. Legeckis, S. J. Lentz, R. Limeburner, L. B. Miranda and J. H. Trowbridge (1991) The physical oceanography of the Amazon outflow. *Oceanography*, **4**, 8–14.

Geyer W. R. and G. C. Kineke (1995) Observations of currents and water properties in the Amazon frontal zone. *Journal of Geophysical Research*, **100**, 2321–2339.

Gibbs R. J. (1970) Circulation in the Amazon River estuary and adjacent Atlantic Ocean. *Journal of Marine Research*, **28**, 113–123.

Gibbs R. J. (1976) Amazon River sediment transport in the Atlantic Ocean. *Geology* **4**, 45–48.

Gibbs R. J. (1982) Currents on the shelf of northeastern South America. *Estuarine Coastal and Shelf Sciences*, **14**, 283–299.

Jewell P. W., R. F. Stallard and G. L. Mellor (1993) Numerical studies of bottom shear stress and sediment distribution on the Amazon continental shelf. *Journal of Sediment Petrology*, **63**, 734–745.

Johns W. E., T. N. Lee, F. A. Schott, R. J. Zantopp and R. H. Evans (1990) The North Brazil Current retroflection: seasonal structure and eddy variability. *Journal of Geophysical Research*, **95**, 22,103–22,120.

Kalkwijk J. P. T. and R. Booij (1986) Adaptation of secondary flow in nearly-horizontal flow. *Journal of Hydraulic Engineering* **24**, 19–37.

Kineke G. C. and R. W. Sternberg (1995) Distribution of fluid muds on the Amazon continental shelf. *Marine Geology*, **125**, 193–233.

Kineke G. C., R. W. Sternberg, J. H. Trowbridge and R. W. Geyer (1996) Fluid-mud processes on the Amazon continental shelf. *Continental Shelf Research*, **16**, 667–696.

Kuehl S. A., D. J. DeMaster and C. A. Nittrouer (1986) Nature of sediment accumulation on the Amazon continental shelf. *Continental Shelf Research*, **6**, 209–225.

Kuehl S. A., C. A. Nittrouer, M. A. Allison, L. E. C. Faria, D. A. Dukat, J. M. Jaeger, T. D. Pacioni, A. G. Figueiredo and E. C. Underkoffler (1996) Sediment deposition, accumulation and seabed dynamics in an energetic fine-grained coastal environment. *Continental Shelf Research*, **16**, 787–815.

Lentz S. J. (1995a) The Amazon River plume during AmasSeds: subtidal current variability and the importance of wind forcing. *Journal of Geophysical Research*, **100**, 2377–2390.

Lentz S. J. (1995b) Seasonal variations in the Amazon plume structure inferred from historical hydrographic data. *Journal of Geophysical Research*, **100**, 2391–2400.

Lentz S. J. and R. Limeburner (1995) The Amazon River plume during AmasSeds: spatial characteristics and salinity variables. *Journal of Geophysical Research*, **100**, 2355–2375.

Limeburner R., R. C. Beardsley, I. D. Soares, S. J. Lentz and J. Candela (1995) Lagrangian flow observations of the Amazon River discharge into the North Atlantic. *Journal of Geophysical Research*, **100**, 2401–2415.

Limeburner R., I. D. Soares, J. Candela and R. C. Beardsley (1992) CTD observations on the North Brazil shelf during a multidisciplinary Amazon shelf sediment study (AmasSeds). *WHOI Technical Report*, WHOI-92-27, 255 pp.

Miles J. W. (1961) On the stability of heterogeneous shear flow. *Journal of Fluid Mechanics*, **10**, 496–508.

Muller-Karger F. E., C. R. McClain and P. L. Richardson (1988) The dispersal of the Amazon's water. *Nature*, **333**, 56–69.

Nittrouer C. A., T. B. Curtin and D. J. DeMaster (1986) Concentration and flux of suspended sediment on the Amazon continental shelf. *Continental Shelf Research*, **6**, 161–174.

Nittrouer C. A. and D. J. DeMaster (1986) Sedimentary processes on the Amazon continental shelf; past, present and future research. *Continental Shelf Research*, **6**, 5–30.

Nittrouer C. A. and D. J. DeMaster (1996) The Amazon shelf setting—tropical, energetic and influenced by a large river. *Continental Shelf Research*, **16**, 553–573.

Nittrouer C. A., D. J. DeMaster, A. G. Figueiredo and J. M. Rine (1991) AmasSeds: an interdisciplinary investigation of a complex coastal environment. *Oceanography*, **4**, 3–7.

Oltman R. E. (1968) Reconnaissance investigations of the discharge and water quality of the Amazon River. *U.S. Geological Survey Circular* 552, Washington, D.C., 16 pp.

Osborn T. R. (1980) Estimates of the local rate of vertical diffusion from dissipation measurements. *American Meteorological Society*, **10**, 83–89.

Paluszkiewicz T. (1993) A numerical modeling study of the near- and far-field dispersal of the Amazon outflow. Ph.D. Thesis, University of Maryland, Cambridge, MD, 141 pp.

Richey J. E., R. H. Meade, E. Salati, A. H. Devol, C. F. Nordin Jr and U. Dos Santos (1986) Water discharge and suspended sediment concentrations in the Amazon River: 1982–1984. *American Geophysical Union*, **22**(5), 756–764.

Soulsby R. L. (1990) Tidal–current boundary layers. In: *The Sea, Ocean Engineering Science*, B. Le Mehaute and D. M. Hanes, editors, Wiley and Sons Inc., **9**(Part A), 523–566.

Sternberg R. W., D. A. Cacchione, B. Paulson, G. C. Kineke and D. E. Drake (1996) Observations of sediment transport on the Amazon subaqueous delta. *Continental Shelf Research*, **16**, 697–715.

Stumpf R. P. and G. Gelfenbaum, J. R. Pennock and W. W. Schroeder (1993) Seasonal changes in suspended sediment distributions of Mobile Bay, Alabama. Presented at: 12th Biennial International Estuarine Research Federation Conference. *Science and Management of Estuarine Coastal Systems—Abstracts*, 120.

Thorpe S. A. (1971) Experiments on the instability of stratified shear flows: miscible fluids. *Journal of Fluid Mechanics*, **46**, 299–319.

Trowbridge J. H. (1992) A simple description of the deepening and structure of a stably stratified flow driven by a surface stress. *Journal of Geophysical Research* **97**, 15,529–15,543.

Trowbridge J. H. and G. C. Kineke (1994) Structure and dynamics of fluid muds over the Amazon continental shelf. *Journal of Geophysical Research*, **99**, 865–874.